



저작자표시-비영리-변경금지 2.0 대한민국

이용자는 아래의 조건을 따르는 경우에 한하여 자유롭게

- 이 저작물을 복제, 배포, 전송, 전시, 공연 및 방송할 수 있습니다.

다음과 같은 조건을 따라야 합니다:



저작자표시. 귀하는 원저작자를 표시하여야 합니다.



비영리. 귀하는 이 저작물을 영리 목적으로 이용할 수 없습니다.



변경금지. 귀하는 이 저작물을 개작, 변형 또는 가공할 수 없습니다.

- 귀하는, 이 저작물의 재이용이나 배포의 경우, 이 저작물에 적용된 이용허락조건을 명확하게 나타내어야 합니다.
- 저작권자로부터 별도의 허가를 받으면 이러한 조건들은 적용되지 않습니다.

저작권법에 따른 이용자의 권리는 위의 내용에 의하여 영향을 받지 않습니다.

이것은 [이용허락규약\(Legal Code\)](#)을 이해하기 쉽게 요약한 것입니다.

[Disclaimer](#)

공학박사학위논문

**Enhancing damping estimation in
cable-supported bridges under
operational conditions**

공용중 케이블교량의 계측데이터 기반
감쇠비 추정기법 개선

2017 년 8 월

서울대학교 대학원

건설환경공학부

김 선 중

ABSTRACT

An enhanced output-only algorithm of the Natural Excitation Technique—Eigensystem Realization Algorithm (NExT-ERA) was suggested to solve a large scattering in identified damping ratio still remains to be a challenging issue. The suggested damping estimation procedure was applied to a parallel cable-stayed bridge for identifying structural damping ratios before and after the installation of a Multiple Tuned Mass Damper (MTMD) designed to mitigate a vortex-induced vibration (VIV) that was observed on the bridge.

The automated proper parameter selection process for NExT-ERA was suggested to reduce the large error bound due to poor parameter selection and achieve similar level of correctness of heuristic parameter selection. To make suitable criteria for each algorithm parameter, a series of parametric studies using numerical simulation and operational monitoring data was performed, respectively. It was discovered that the number of FFT (NFFT) of 2^{15} with 60 min data provided the accurate estimation in terms of mean and coefficient of variance (COV). A size of Hankel matrix was determined corresponding to the shape of calculated impulse response function (IRF). To overcome the limitation of non-structural model based algorithm, the sensitivity analysis

was performed using each estimated value according to a system order. The median value of estimated damping ratios provided a converged value successfully. This automated parameter selection process accomplished the more accurate damping estimation compared to the result of heuristic parameter selection.

The research also discovered that the effect of traffic loadings on the uncertainty of operational modal analysis (OMA) based damping estimation. The experimental studies found a localized response in traffic-induced vibration (TIV). When the number of traffic lane over the bridge is only one or two for one direction and the traffic volume is not high, the ambient vibration signal at the sensor position show an envelope as a vehicle is approaching and fading away. Since OMA assumes that the signal to be analyzed is a stationary white-noise process, the envelop-like signal obtained from running vehicles can also contribute the scattering in Structural Identification (St-Id). Furthermore, this traffic loading distorted the PSD of measured acceleration. A comparison between the PSD of stationary response and TIV clearly demonstrated that the frequency components of 2-5 Hz were amplified during the vehicle crossed the bridge. The ERA is the energy-based method so that the dominant modes will be more easily identified. Therefore, the distortion in PSD can be a reason for the poor modal identification.

To remove this envelope-like trend in measured data, a signal stationarization process based on amplitude-modulating function was employed to the simulated response and measured data, respectively. If the nonstationary loading can be represented by the product of amplitude-modulating function and stationary white noise process, then the envelope function can be evaluated by temporal root-mean-square function of responses. Consequently, the approximated stationary process can be extracted by dividing the measurements with calculated envelope function. This signal stationarization process successfully extracted the stationary process from the TIV. This signal stationarization process was applied to the 3-day operational monitoring data. It is discovered that some highly scattered points were eliminated by the signal stationarization. The COV of estimated damping ratios is significantly reduced, indicating the signal stationarization process is worth in reducing scattering in identified damping ratios from OMA. As a result, the amplitude dependency of a damping ratio also more clearly appeared in terms of R-squared value of linear regression increasing.

Since a multiple tuned mass damper (MTMD) was installed at the center of the main span to mitigate VIV, the modal damping ratios before and after the installation of the MTMD were also compared. Several sets of operational monitoring data that had been collected under various windy conditions were

used to develop a relationship between the identified damping ratios and the corresponding VIV level of the bridge. The performance of the bridge was enhanced regarding vibrational serviceability, based on the above findings.

The effect of environmental factors on the variation of damping ratio was evaluated. Three environmental factors of vibration amplitude, the number of vehicle and temperature were selected, and the statistical relationship between the damping ratio and each environmental parameter was evaluated through correlation analysis. The result confirmed that the main source of damping ratio of cable-supported bridge was traffic-induced vibration which showed a high positive correlation with the number of vehicle and corresponding vibration amplitude of TIV. RMS amplitude also increased within lock-in range, but no corresponding increase in the damping ratio was observed. The effect of temperature changes was also relatively low. The analysis of the amplitude-dependency of the damping ratio clearly showed that a tendency was clearly appeared by applying the stationarization method to reducing uncertainties in damping estimates.

Keywords: Operational Modal Analysis, Damping ratio, NExT-ERA, Cable-supported bridge, Stationarization, Amplitude-dependency,

Student Number: 2012-30241

Table of Contents

1. Introduction	1
1.1. Research background	3
1.2. Problem definition.....	7
1.3. Objective and scope	9
2. Damping estimation based on operational modal analysis	13
2.1. NExT-ERA: Output-only operational modal analysis.....	15
2.1.1. Literature survey: OMA-based damping estimation	15
2.1.2. Natural Excitation Technique (NExT).....	17
2.1.3. Eigensystem Realization Algorithm (ERA)	23
2.2. Damping estimation of cable-stayed bridge.....	29
2.2.1. Bridge description: Jindo Bridge.....	29
2.2.2. Monitoring data	30
2.2.3. Excitation test using TMD	33
2.2.4. Operational damping estimation using 3-days data.....	38
2.3. Concluding remarks	42

3.	Automated proper parameter selection for NExT-ERA.....	43
3.1.	Analysis parameter of NExT-ERA.....	45
3.2.	Parametric studies of numerical simulation	46
3.2.1.	Description of the simulated models	46
3.2.2.	Algorithmic parameters of NExT: NFFT and data length.....	47
3.2.3.	Algorithmic parameters of ERA: Size of Hankel matrix and system order	53
3.3.	Parametric studies using field monitoring data	58
3.3.1.	NFFT and the record length	59
3.3.2.	Size of Hankel matrix.....	60
3.3.3.	System order.....	61
3.4.	Application: Jindo Bridge	63
3.4.1.	Parameter selection	63
3.4.2.	Estimated damping ratio after proper parameter selection.....	66
3.4.3.	Computational cost.....	68
4.	Signal stationarization for traffic-induced vibration.....	71
4.1.	Introduction.....	73

4.2.	Experimental investigation for TIV properties.....	75
4.2.1.	Bridge description: Sorok Bridge.....	75
4.2.2.	Monitored data	76
4.2.3.	Experimental condition	77
4.2.4.	Nonstationary effect of TIV on a measured signal.....	80
4.3.	Signal stationarization using amplitude-modulating function.....	85
4.3.1.	Amplitude-modulating function	85
4.3.2.	The optimal segment length for signal stationarization	87
4.3.3.	Signal stationarization of operational monitoring data	91
4.4.	Application to NExT-ERA: numerical simulation	93
4.4.1.	Description of simulated models.....	93
4.4.2.	Estimated damping ratio corresponding to signal stationarization	100
4.5.	Application to NExT-ERA: operational monitoring data of Jindo Bridge	102
4.5.1.	Combined framework of p.p.s and stationarization.....	102
4.5.2.	Monitoring data	104
4.5.3.	Effect of signal stationarization in Jindo Bridge	104

4.5.4. Estimated damping ratio according to signal stationarization...	107
4.6. Application to NExT-ERA: Jindo Bridge after installation of MTMD	112
4.6.1. Monitored data	112
4.6.2. Estimated damping ratio corresponding to signal stationarization	114
4.6.3. Effectiveness of MTMD according to windy condition.....	118
4.7. Concluding remarks	126
5. Environmental effect on the variation of estimated damping ratio.....	127
5.1. Main environmental factors for variation of damping ratio	130
5.1.1. Vibration amplitude.....	130
5.1.2. Number of vehicle.....	132
5.1.3. Temperature.....	133
5.1.4. Aerodynamic damping ratio.....	135
5.2. Correlation analysis between estimated damping ratio and environmental factors	138
5.3. Correlation analysis between estimated damping ratio and environmental factors without lock-in range data set	141
5.4. Amplitude-dependency	143

5.5.	Conclusion.....	146
6.	Conclusions and further study	147
6.1.	Conclusions and contributions	149
6.2.	Suggestion	151
	References.....	154

List of Figures

Figure 1-1 The Jindo Bridge	3
Figure 1-2 Observed VIV in Bridge 2: (a) wind velocity and (b) vertical acceleration of the deck at the center of the mid span	4
Figure 1-3 Mode shapes and natural frequencies of Bridge 2: (a) first symmetric lateral mode with 0.311Hz, (b) first symmetric vertical mode with 0.436Hz, and (c) first symmetric torsional mode with 1.815Hz.....	6
Figure 2-1 Deployment of the two bridges and built-in sensors	30
Figure 2-2 Wind properties for a three-day monitoring period: (a) 10-minute average wind velocity and (b) 10-minute average wind direction	32
Figure 2-3 The MTMD installed in the deck of Bridge 2	33
Figure 2-4 Time histories for the measured acceleration of the bridge deck during the free vibration test	34
Figure 2-5 Estimated damping ratio via fitting an exponential function for uncontrolled case using (a) positive peaks and (b) negative peaks	35
Figure 2-6 Estimated damping ratio via fitting as exponential function for semi-controlled case using (a) positive peaks and (b) negative peaks	36
Figure 2-7 Estimated damping ratio via fitting as exponential function for fully controlled case using (a) positive peaks and (b) negative peaks	37
Figure 2-8 Measured vertical acceleration at the center of the main span of	

Bridge 2 during 12/10/15 13:40-14:00: (a) time history for 20 minutes, (b) PSD and (c) auto correlation function or equivalently impulse response function.....	39
Figure 2-9 Estimated damping ratio for the first vertical mode of Bridge 2...	40
Figure 2-10 Estimated damping ratio for the first vertical mode of Bridge 2.	41
Figure 3-1 Definition of modal analysis parameters represented in (a) measured acceleration history of ambient vibration and (b) calculated correlation function.....	49
Figure 3-2 Estimated damping ratio according to NFFT: (a) mean of the first mode and (b) second mode, (c) COV of the first mode and (d) second mode.....	52
Figure 3-3 Calculated impulse response function and the utilized time length	54
Figure 3-4 (a) Mean value and (b) COV of estimated damping ratio according to utilized time of impulse response function	55
Figure 3-5 A newly proposed procedure to select a converged damping ratio	57
Figure 3-6 Estimated damping ratio according to a system order.....	58
Figure 3-7 Estimated damping ratio according to NFFT and record length: (a) mean of the damping ratio and (b) COV of the damping ratio	59
Figure 3-8 (a) mean and (b) COV of estimated damping ratio according to utilized length of IRF	61
Figure 3-9 Estimated damping ratio according to system order (Oct. 16 10:00AM).....	62
Figure 3-10 Determining a utilized time length of IRF based on envelope	

function	65
Figure 3-11 Estimated damping ratio of Jindo Bridge corresponding to proper parameter selection	67
Figure 3-12 (a) Estimated damping ratio according to system order and (b) elapsed time according to the maximum number of system order	69
Figure 4-1 View of the Sorok Bridge	75
Figure 4-2 Utilized sensors in the monitoring system at the center of the mid span of the Sorok Bridge.....	77
Figure 4-3 A truck loading test.....	78
Figure 4-4 (a) Measured displacement and acceleration at the center of mid span and (b) moving mean, standard deviation and kurtosis of (a)	79
Figure 4-5 The measured acceleration and its PSD of stationary excitation...	81
Figure 4-6 The measured acceleration and its PSD under heavy truck.....	82
Figure 4-7 The measured acceleration and its PSD under ordinary vehicle ...	82
Figure 4-8 Normalized PSD amplitude of first vertical mode and structural modes within 2-3 Hz.....	83
Figure 4-9 Time-frequency distribution of Jul. 15 to 17	84
Figure 4-10 A brief concept of nonstationary process modeling.....	85
Figure 4-11 The calculated AM function using moving RMS ($T_w = 0.1s$).....	87
Figure 4-12 Moving RMS according to the segment length	89
Figure 4-13 Maximum value of moving RMS by the segment ratio (T_w/T_n) ..	90
Figure 4-14 Calculated AM function according to segment ratio	91
Figure 4-15 Measured acceleration (a) without signal stationarization and (b)	

with stationarization.....	92
Figure 4-16 PSD of measured acceleration (a) w/o signal stationarization and (b) with stationarization	93
Figure 4-17 Schematic diagram of 9-DOF shear building	94
Figure 4-18 (a) free decaying acceleration at the top floor and (b) its PSD....	96
Figure 4-19 Time histories of (a) stationary loading, (b) amplitude-modulating function and (c) nonstationary loading	98
Figure 4-20 Calculated acceleration of 8 th story under (a) stationary excitation, (b) nonstationary excitation and (c) stationarized acceleration of (b)	99
Figure 4-21 Estimated 3 rd modal damping ratio for the 100 simulations	100
Figure 4-22 Proposed damping estimation framework	103
Figure 4-23 (a) Measured acceleration at Oct. 16, 22:00 and corresponding calculated amplitude-modulating function (b) stationarized acceleration of (a)	105
Figure 4-24 PSD of measured acceleration (Oct. 16, 22:00) according to signal stationarization process	106
Figure 4-25 Kurtosis according to stationarization	107
Figure 4-26 Estimated modal damping ratio of Jindo Bridge according to proper parameter selection and signal stationarization	108
Figure 4-27 Estimated damping ratio for 3-day data (x: Ad hoc parameter selection for each 20-min segmented acceleration data (Kim et al., 2013),▲: Proposed parameter selection for each 60-min	

segmented acceleration data, ●: Proposed parameter selection for each stationarized 60-min segmented acceleration data)	109
Figure 4-28 Estimated modal damping ratio of Jindo Bridge by applying combined method.....	111
Figure 4-29 The statistics of estimated damping ratio according to the segment ratio of moving RMS: (a) mean value and (b) COV	112
Figure 4-30 1-hour mean wind velocity for 4-day wind data.....	113
Figure 4-31 Estimated damping ratio during the operating MTMD with basic analysis condition.....	114
Figure 4-32 Comparison of estimated damping ratio during the operating MTMD between the cases of basic and signal stationarization condition	115
Figure 4-33 PSD amplitude of first vertical mode	117
Figure 4-34 V-A curve of the averaged vertical vibration of TMDs	118
Figure 4-35 (a) Measured acceleration, (b) cross correlation function between Bridge 2 and MTMD (time lag is 0.03 second corresponding to phase lag of 4.71°), (c) PSD of bridge and (d) PSD of MTMD for low wind velocity.....	121
Figure 4-36 (a) Measured acceleration, (b) cross correlation function between Bridge 2 and MTMD (time lag is 0.57 second corresponding to phase lag of 91.4°), (c) PSD of bridge and (d) PSD of MTMD for onset wind velocity	123
Figure 4-37 V-A curve of the deck of Bridge 2 with and without the MTMD	124

Figure 4-38 PSD of the measured acceleration (a) without MTMD ($U = 10.61\text{m/s}$) and (b) with MTMD ($U = 10.04\text{m/s}$)	125
Figure 5-1 Local maxima from the measured acceleration of Jindo Bridge .	132
Figure 5-2 The location of Jindo Bridge and automatic weather station (AWS)	135
Figure 5-3 (a) Flutter derivatives and (b) Calculated mode shape along the bridge deck for the first vertical mode	137
Figure 5-4 Estimated aerodynamic damping.....	138
Figure 5-5 Normalized distribution of damping ratio and representative environmental factors according to time evolution (3-days)	139
Figure 5-6 The distribution of RMS acceleration with (a) corresponding the number of vehicle and (b) identified damping ratios	140
Figure 5-7 Normalized distribution of damping ratio and representative environmental factors according to time evolution (3-days) after discarding the lock-in data set.....	142
Figure 5-8 Amplitude-dependency of estimated damping ratio (basic)	143
Figure 5-9 Amplitude-dependency of estimated damping ratio (proper parameter selection).....	144
Figure 5-10 Amplitude-dependency of estimated damping ratio (signal stationarization).....	145

List of Tables

Table 2-1 Output influence matrix and direct-transmission term.....	25
Table 2-2 The experimental condition of excitation test	35
Table 3-1 Structural properties of a 2-DOF model.....	47
Table 3-2 Modal properties of a 2-DOF model	47
Table 3-3 List of parameters according to the selected NFFT	50
Table 4-1 The modal frequencies of the Sorok Bridge.....	76
Table 4-2 Classification of data utilized.....	80
Table 4-3 Modal characteristics of 9-story numerical model	95
Table 4-4 Result of ERA using free decays.....	96
Table 4-5 Case name and corresponding simulation conditions	99
Table 4-6 The statistics of estimated 3 rd modal damping ratio.....	100
Table 4-7 The statistics of estimated modal damping ratio of Jindo Bridge .	109
Table 4-8 The statistics of estimated modal damping ratio of Jindo Bridge after proper parameter selection.....	111
Table 4-9 The statistics of estimated modal damping ratio of Jindo Bridge with operating MTMD	116
Table 5-1 Correlation coefficient between identified damping ratios and environmental factor	139
Table 5-2 Correlation coefficient between identified damping ratios and environmental factor without lock-in range data set.....	142

Chapter 1

Introduction

Some parts of this chapter were reported in following journal publications:

Kim S-J, Kim H-K, Calmer R, Park J, Kim GS, Lee DK. Operational field monitoring of interactive vortex-induced vibrations between two parallel cable-stayed bridges. *Journal of wind engineering and industrial aerodynamics*. 2013;123:143-54.

Kim S, Park J, Kim H-K. Damping Identification and Serviceability Assessment of a Cable-Stayed Bridge Based on Operational Monitoring Data. *Journal of Bridge Engineering*. 2016:04016123.

1.1. Research background

In 2011, an unexpected VIV was observed in the upstream deck of the parallel cable-stayed bridge shown in Figure 1-1. As shown in Figure 1-2, the maximum acceleration was far beyond the allowable limit of 0.5 m/s^2 (KSCE, 2006) resulting in a serviceability problem.



Figure 1-1 The Jindo Bridge

A series of wind tunnel tests were performed in an attempt to identify the main sources of VIV (Seo et al., 2013). The study pointed out that the amplitude of the VIV in Bridge 2 was sensitive to the mechanical damping of the bridge. The estimated damping ratio of Bridge 2 was lower than the design value and this was proposed to constitute one of the sources of the VIV. It was

also found that large vortices were developed between two decks with alternating “ Ω ” and “ \mathcal{O} ” shaped streamlines. Seo et al. (2013) traced the pattern of the streamlines and flow speeds between the two decks and successfully demonstrated an interference effect on the upstream deck. Since the amplitude of VIV was sensitive to the mechanical damping ratio of the bridges while modifying the deck shape with aerodynamic attachments such as fairing or guide vanes was not effective in mitigating the VIV (Kim et al., 2013; Seo et al., 2013), a multiple tuned mass damper (MTMD) was designed and installed at the center of the main span (HDEC, 2012a).

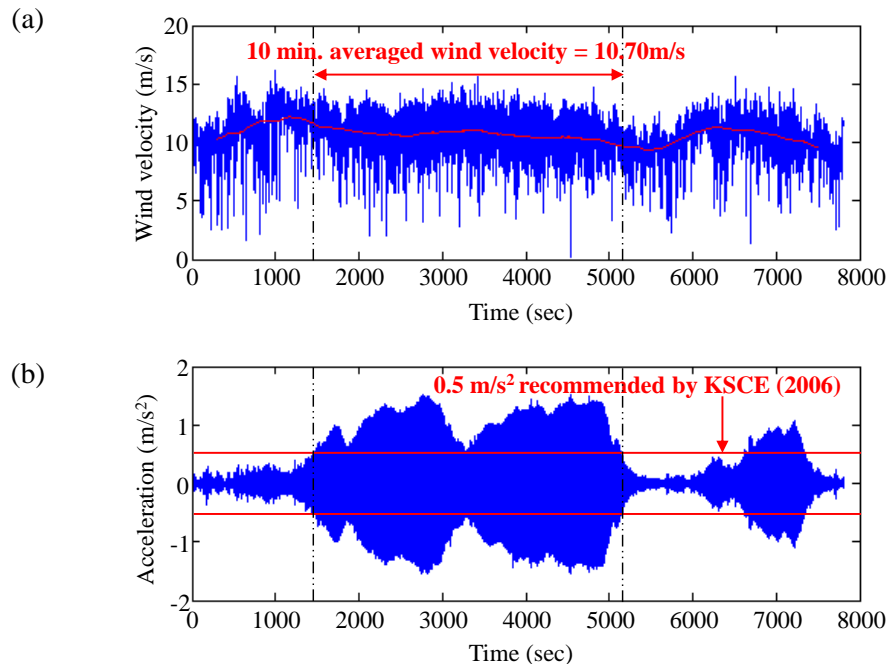
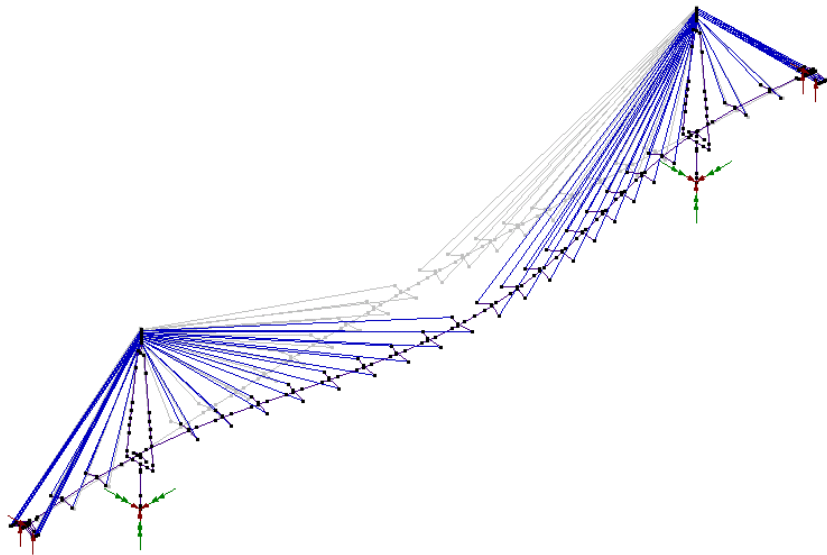
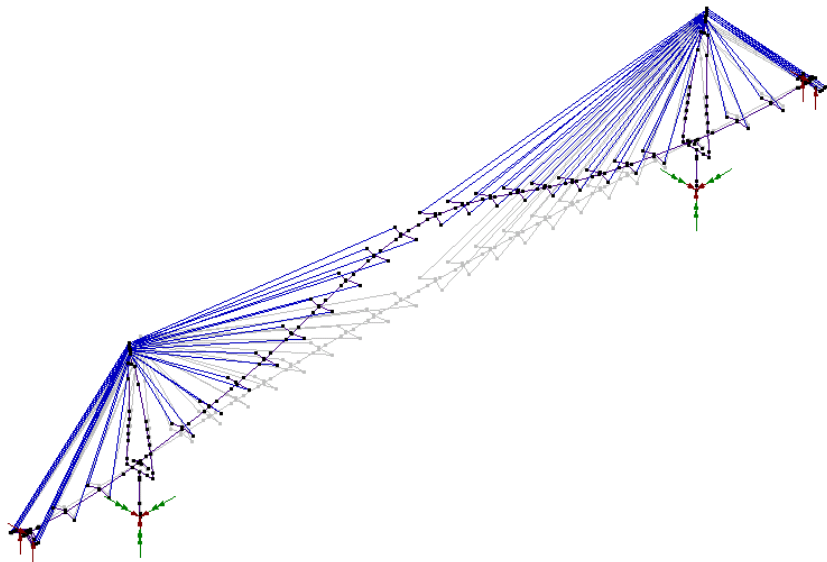


Figure 1-2 Observed VIV in Bridge 2: (a) wind velocity and (b) vertical acceleration of the deck at the center of the mid span

(a)



(b)



(c)

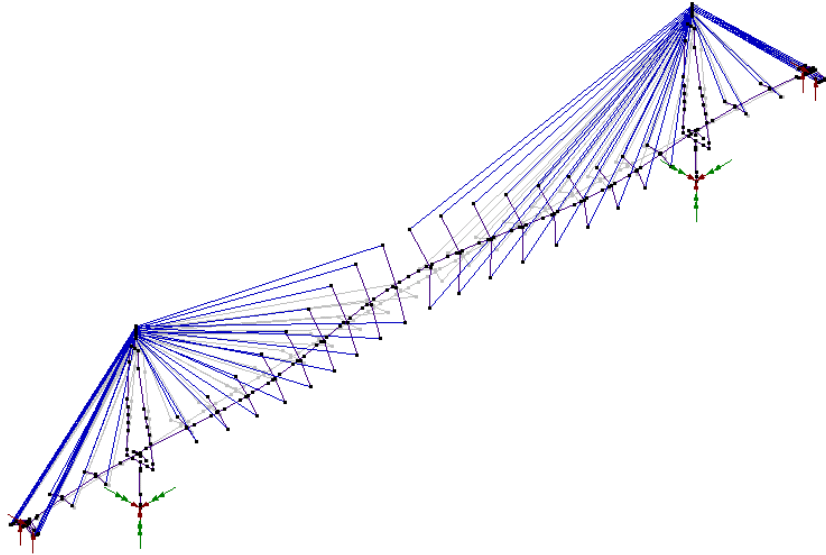


Figure 1-3 Mode shapes and natural frequencies of Bridge 2: (a) first symmetric lateral mode with 0.311Hz, (b) first symmetric vertical mode with 0.436Hz, and (c) first symmetric torsional mode with 1.815Hz

Figure 1-3 (a)-(c) shows the calculated mode shapes and natural frequencies of Bridge 2 for the first vertical, lateral and torsional modes. These frequencies are in good agreement with field-measured data from ambient vibration tests (Spencer Jr et al., 2011). The frequency of the observed VIV was identified as 0.438Hz (Seo et al., 2013) and matches the first vertical mode of 0.446Hz in the calculation.

1.2. Problem definition

As can be seen in Section 1.1, structural damping ratio is an important issue that is used in assessing the vibrational serviceability of long-span bridges due to their flexibility and relatively low structural damping capacity (Magalhães et al., 2012; Martínez-Rodrigo and Filiatrault, 2015; Xing et al., 2013). It is a critical factor in evaluating the amplitude of the vortex-induced vibration (VIV) of cable-supported bridges under operational conditions. As a result, an increasing interest in assessing the serviceability of cable-supported bridges has developed, concerning obtaining a reliable estimation of damping.

The modal damping ratios can be theoretically estimated by applying sweeping test with exciters for harmonic motion. Specially developed exciters were utilized for excitation of actual bridges (Brownjohn et al., 2003; Chen et al., 2016; Wen et al., 2017). A sudden release test of heavy weight was also utilized for the excitation of free-decaying motion of bridge structure (Magalhães et al., 2010). However, as the span length increases in recent long-span and super-long span bridges, the use of heavy exciters or sudden release tests are no more applicable from the point of view not only in structural safety but also in securing continuous traffic flows. If not, then a huge impulse loading which exceeds the level of ambient vibration loading has to be applied but it would rather be harmful to the structure.

Accordingly, AVT has been preferred to many researchers due to the economic and practical reasons. Moreover, as a classical output-only system identification (SI) scheme, a Frequency Domain Decomposition (Brincker et al., 2000), Eigensystem Realization Algorithm (Juang and Pappa, 1985) and Subspace Stochastic Identification (De Roeck, 2001; Van Overschee and De Moor, 2012) were developed and successfully applied to long-span bridge for modal identification.

More reliable and accurate operational modal analysis (OMA) techniques have also been developed with the consideration of reducing the uncertainties. Numerous researches have succeed to find natural frequencies or mode shapes of bridges accurately using operational monitoring data (Brownjohn et al., 2010; Siringoringo and Fujino, 2008). On contrary, a damping identification is still challenging unlike a natural frequency or mode shape (Rainieri and Fabbrocino, 2014). There are still large error bounds with a significant scattering in estimated damping ratio distribution. That is the reason why reference test such as FVTs are still required for reliable result.

There are many mechanisms to introduce a damping in a structure, and this complexity is a reason for the uncertainty in damping ratio. The material damping ratio comes from a complex molecular interaction while the mechanical damping from friction between connection of member and

bearing. A soil-structure interaction, aerodynamic/hydraulic damping also contributes to a damping ratio (Kareem and Gurley, 1996). Furthermore, many of environmental factors can contribute significantly to the overall reliability of identified damping ratio in a point of view of operating environment, controlled experimentations, data processing or model calibrations of system identification (Moon and Aktan, 2006). A nonlinear/nonstationary loading causes the uncertainty in damping estimation. Jeary (1992) performed a full-scale measurement and found that the nonlinearity between wind velocity and vibration amplitude of bridge increased error in damping estimation.

1.3. Objective and scope

This dissertation aims to improve the accuracy of operational damping estimation to overcome the limitation of classic OMA under traffic loading. The investigated bridge is Bridge 2 of Jindo Bridges. Chapter 2 focuses on the preliminary damping estimation of Jindo Bridge based on OMA. At first, with the literature surveys of OMA based damping estimations, the review of NExt-ERA is included. The theoretical backgrounds of both algorithms are described, respectively. The estimates of damping ratio of Bridge 2 are presented, and the lessons from the result are described.

Chapter 3 focuses on the automation of proper parameter selection for reliable OMA. The main algorithm parameters of NExT-ERA are defined. Parametric studies using simulated data and operational monitoring data are included, respectively. With the proposed parameter selection process, the damping ratio of Jindo bridge is estimated again. The comparative analysis with the preliminary estimation in Chapter 2 is included to assess the effect of proper parameter selection.

Chapter 4 presents the effect of signal stationarization for traffic-induced vibration. First the detailed traffic-induced vibration (TIV) properties in real bridge are presented by experimental investigations. To deal with the frequency distortion due to the nonstationary traffic loading, the amplitude-modulating function is introduced to eliminate global trends caused by nonstationary input. NExT-ERA is re-applied to estimate the damping ratio for a stationarized process. Comparative analysis was performed between an extracted stationary process and nonstationary data to demonstrate the effect of eliminating nonstationarity for improving the accuracy of operational damping estimation. Using this verified OMA based damping estimation algorithm, the effectiveness of TMD in Jindo Bridge is measured in terms of enhanced damping ratio.

Chapter 5 focused on assessing the effect of environmental factors on the

variation of damping ratio, and identifying the most dominant parameter. First, the factors affecting the damping ratio change were selected based on the damping ratio distribution, and the characteristics of each parameter were analyzed. Next, the statistical relationship between the damping ratio and each environmental parameter was evaluated through correlation analysis. Based on these result, the effect of environmental factors on the damping ratio was analyzed.

The final chapter summarizes the conclusions of this research. The importance and contribution of the results are presented. Moreover, the limitation and some further researches are suggested.

While this thesis has been prepared for a long duration, many parts were already published or submitted in journals (Kim et al., 2013; Kim et al., 2016; Kim and Kim, 2017; Kim et al., 2018).

Chapter 2

Damping estimation based on operational modal analysis

Some parts of this chapter were reported in following journal publications:

Kim S-J, Kim H-K, Calmer R, Park J, Kim GS, Lee DK. Operational field monitoring of interactive vortex-induced vibrations between two parallel cable-stayed bridges. *Journal of wind engineering and industrial aerodynamics*. 2013;123:143-54.

Kim S, Park J, Kim H-K. Damping Identification and Serviceability Assessment of a Cable-Stayed Bridge Based on Operational Monitoring Data. *Journal of Bridge Engineering*. 2016:04016123.

2.1. NExT-ERA: Output-only operational modal analysis

2.1.1. Literature survey: OMA-based damping estimation

Output-only operational modal analysis scheme is classified into two categories: 1) frequency domain and 2) time domain method. Frequency domain methods such as Peak Picking or FDD identify the modal information based on the PSD of measured responses (Brincker et al., 2001). He et al. (2009) subdivided a time domain method into two categories: 1) two-stage method and 2) one-stage method. The two stage methods require a calculating free vibration response from a measured response by Random Decrement (RD) or NExT algorithm. Then, the classic modal identification methods such as the ERA (Brownjohn et al., 2010; Caicedo et al., 2004; Sim et al., 2010; Yun, 2009), the Ibrahim Time Domain method (ITD), the Poly-Least Squares Complex Exponential (p-LSCE) (Magalhães and Cunha, 2011; Magalhães et al., 2010) are applied to the calculated free vibration response. In contrast, the one-stage approaches (e.g. Stochastic Subspace Identification, SSI) extract modal parameters directly (Brownjohn et al., 2010; He et al., 2009; Magalhães et al., 2007; Magalhães and Cunha, 2011; Magalhães et al., 2010; Rodrigues and Brincker, 2005).

To estimate the damping ratio of long-span bridges, many of researchers have been applied several output-only system identification algorithms for a

mutual validation. He et al. (2009) applied three output-only system identification methods consist of multiple-reference NExT-ERA, SSI-COV and Enhanced FDD (EFFD). The result showed that mNExT-ERA and SSI-COV was more robust than EFDD while the differences of identified damping ratios from three methods were relatively large compared to that of natural frequencies. Moaveni et al. (2014) also compared the accuracy of the NExT-ERA, the SSI-COV and the EFFD in modal identification from results obtained for a 7-story building on the shake table. Magalhães et al. (2010) compared the performance of the EFFD and the SSI-COV for damping estimation by numerical simulation. Although the SSI-COV resulted in being more robust, the result of SSI-COV with the ambient vibration from three large civil infrastructures (stadium suspended roof, footbridge and cable-stayed bridge) showed a high scatter with COV around 50%. Brownjohn et al. (2010) estimated modal properties using NExT-ERA, SSI-COV and least squares complex frequency domain (p-LSCF). Siringoringo and Fujino (2008) utilized the RD-ITD and NExT-ERA to the OMA of a suspension bridge using three-days of monitoring data. It clearly proved that the NExT-ERA was more practical and efficient to treat massive data set.

Based on a series of previous studies, it is known that the NExT-ERA and SSI-COV was most preferred and well-verified algorithm for output-only

system identification. Of that, NExT-ERA was selected as the investigating algorithm. SSI can be applied directly to ambient vibration records like “black-box”. Otherwise, NExT calculates the impulse response function so that it is more appropriate to consider a physical meaning. Furthermore, NExT-ERA has the potential to be enhanced by the reliable parameter selection and the treatment of nonstationarity in loading. Magalhães et al. (2010) also found that the SSI showed less dependency to the algorithm parameter compared to other methods. Actually, SSI has fewer parameters to consider compared to NExT-ERA. It is convenient in simplified application, but not suitable to stabilize the result with proper parameter selection. Since NExT-ERA is a two-stage method, more parameters should be defined carefully. It can be said that NExT-ERA can be enhanced to stabilize the estimated damping ratio with a physical sense and corresponding parameter selection procedure.

2.1.2. Natural Excitation Technique (NExT)

The basic concept of the NExT is that the auto and cross correlation function of responses under the Gaussian white noise loading has similar modal properties of impulse response. This chapter presents a simple description of NExT algorithm.

The equations of motion for MIMO (multiple input and multiple output) can be expressed as follows.

$$\mathbf{M}\ddot{\mathbf{x}} + \mathbf{C}\dot{\mathbf{x}} + \mathbf{K}\mathbf{x} = \mathbf{f} \quad (2-1)$$

where:

- \mathbf{M} = the mass matrix
- \mathbf{C} = the damping matrix
- \mathbf{K} = the stiffness matrix
- \mathbf{x} = the response vector of the system
- \mathbf{f} = the random loads vector.

Eq. 2-1 is generally transformed in a modal coordinate:

$$\mathbf{x} = \mathbf{\Phi}\mathbf{q} = \sum_{n=1}^N \mathbf{\phi}^n q^n \quad (2-2)$$

where:

- $\mathbf{\Phi}$ = the mode matrix
- \mathbf{q} = the modal coordinates vector
- $\mathbf{\phi}$ = the mode vector.
- The subscript n = index of particular mode from a total of N modes.

The mass, damping and stiffness matrix can be diagonalized by multiplication of mode matrix. Then, Eq. 2-1 can be considered as a set of scalar equations as follows.

$$\ddot{\mathbf{q}}^n + 2\xi^n \omega_n^n \dot{\mathbf{q}}^n + \omega_n^{n2} \mathbf{q}^n = \frac{1}{m^n} \boldsymbol{\Phi}^{nT} \mathbf{f} \quad (n = 1, 2, \dots, N) \quad (2-3)$$

where:

- ω_n^n = the n th modal frequency
- ξ^n = the n th modal damping ratio
- m^n = the n th modal mass

The solution of Eq. 2-3 can be described as the convolution integral:

$$\mathbf{q} = \int_{-\infty}^T \boldsymbol{\Phi}^{nT} \mathbf{f}(\tau) \mathbf{g}^n(t - \tau) d\tau \quad (2-4)$$

g is the impulse response function (IRF) of the system which is expressed as follows:

$$\mathbf{g}(t) = \frac{1}{m^n \omega_d^n} \exp(-\xi^n \omega_n^n t) \sin(\omega_d^n t) \quad (2-5)$$

where:

- ω_d^i = the damped frequency ($= \omega_n^n \sqrt{1 - \xi^{n2}}$)

We can notice that the impulse response function is the summation of decayed sinusoidal function containing modal properties. By putting Eq. 2-4 to Eq. 2-2, a single output x_{ik} (response at i^{th} node due to the load at k^{th} node) is derived as follows:

$$x_{ik}(t) = \sum_{n=1}^N \Phi^n \Phi^{nT} \int_{-\infty}^t f_k(\tau) g^n(t - \tau) d\tau \quad (2-6)$$

Based on Eq. 2-6, the impulse response can be obtained where the force vector is a Dirac delta function at initial condition.

$$x_{ik}(t) = \sum_{n=1}^N \Phi^n \Phi^{nT} \frac{1}{m^n \omega_d^n} \exp(-\xi^n \omega_n^n t) \sin(\omega_d^n t) \quad (2-7)$$

As previously mentioned, a correlation function is considered as impulse response function in NExT. The cross-correlation function of two responses under stationary white noise excitation is evaluated as following equation:

$$\begin{aligned} R_{ijk}(T) &= E[x_{ij}(t+T) x_{ik}(t)] = \sum_{r=1}^N \sum_{s=1}^N \Phi_r^T \Phi_k^r \Phi_j^s \Phi_k^s \\ &\cdot \int_{-\infty}^T \int_{-\infty}^{t+T} g^r(t+T-\sigma) g^s(t-\tau) E[f_k(\tau) f_k(\sigma)] d\tau d\sigma \end{aligned} \quad (2-8)$$

By the definition of the white noise, the correlation function between $f_k(\tau)$ and $f_k(\sigma)$ is considered as the Dirac delta function as below:

$$E[f_k(\tau) f_k(\sigma)] = C\delta(\tau - \sigma) \quad (2-9)$$

where C is a constant. Then, the first integration in Eq. 2-8 can be collapsed by the definition of a Dirac delta function:

$$\begin{aligned} R_{ijk}(T) &= \sum_{r=1}^N \sum_{s=1}^N \Phi_i^r \Phi_k^r \Phi_j^s \Phi_k^s C \int_{-\infty}^T \mathbf{g}^r(t + T - \tau) \mathbf{g}^s(t - \tau) d\tau \\ &= \sum_{r=1}^N \sum_{s=1}^N \Phi_i^r \Phi_k^r \Phi_j^s \Phi_k^s C \int_0^{\infty} \mathbf{g}^r(\lambda + T) \mathbf{g}^s(\lambda) d\lambda \end{aligned} \quad (2-10)$$

Eq. 2-5 shows that the impulse response function is the form of sine function. Therefore, a trigonometric identities and formulas allow dividing $\mathbf{g}^r(\lambda - \tau)$, which is the combination of exponential function and sine function, depending to λ and T as follows.

$$\begin{aligned} \mathbf{g}^r(\lambda + T) &= e^{-\xi^r \omega_n^r T} \cos(\omega_d^r T) \frac{e^{-\xi^r \omega_n^r \lambda} \sin(\omega_d^r \lambda)}{m^r \omega_d^r} \\ &\quad + e^{-\xi^r \omega_n^r T} \sin(\omega_d^r T) \frac{e^{-\xi^r \omega_n^r \lambda} \cos(\omega_d^r \lambda)}{m^r \omega_d^r} \end{aligned} \quad (2-11)$$

Note that all terms corresponding to T in Eq. 2-11 can be factored out from integral while terms in λ is under integral. Then Eq. 2-10 becomes

$$R_{ijk}(T) = \sum_{r=1}^N \left[e^{-\xi^r \omega_n^r T} \cos(\omega_d^r T) G_{ijk}^r + e^{-\xi^r \omega_n^r T} \sin(\omega_d^r T) H_{ijk}^r \right] \quad (2-12)$$

where G and H are the constants corresponding to the modal properties such as modal mass, modal damping ratio and mode vector at the i^{th} , j^{th} and k^{th} nodes. Then, the simplified expression of G, H with summation on s are given by

$$G_{ijk}^r = \frac{1}{m_r \omega_d^r} \sum_{s=1}^N \beta_{jk}^{rs} \sqrt{J_{rs}^2 + I_{rs}^2} \sin(\gamma^{rs}) \quad (2-13)$$

$$H_{ijk}^r = \frac{1}{m_r \omega_d^r} \sum_{s=1}^N \beta_{jk}^{rs} \sqrt{J_{rs}^2 + I_{rs}^2} \cos(\gamma^{rs}) \quad (2-14)$$

where

- $J_{rs} = \left(\omega_d^{s^2} - \omega_d^{r^2} \right) + (\xi_r \omega_n^r + \xi_s \omega_n^s)^2$
- $I_{rs} = 2\omega_d^r (\xi_r \omega_n^r + \xi_s \omega_n^s)$
- $\gamma_{rs} = \tan^{-1}(I_{rs}/J_{rs})$
- $\beta_{jk}^{rs} = C \phi_{kr} \phi_{js} \phi_{ks} / m_s$

Substituting Eqs. 2-13 and 2-14 into Eq. 2-12, and summing on k leading to calculate the cross-correlation function due to all inputs gives

$$R_{ijk}(T) = \sum_{r=1}^N \frac{\phi_{ir} \dot{C}_{jr}}{m_r \omega_d^r} e^{-\xi^r \omega_n^r T} \sin(\omega_d^r T + \theta_{jr}) \quad (2-15)$$

where

- C_{jr} = new constant multiplier
- θ_{jr} = new constant phase angle

New constant multiplier and phase angle are introduced by merging two sine functions into a single sine function. As can be seen, Eq. 2-15 is the summation of decayed sinusoidal function with modal properties, which is same characteristic of impulse response function in Eq. 2-5.

2.1.3. Eigensystem Realization Algorithm (ERA)

ERA is utilized to obtain a system matrix in steady-state form based on the impulse response function which is evaluated from NExT procedure.

The equation of motion for a finite-dimensional linear dynamic system can be expressed as follows.

$$\begin{aligned} \mathbf{M}_{st} \ddot{\mathbf{w}} + \mathbf{C}_{st} \dot{\mathbf{w}} + \mathbf{K}_{st} \mathbf{w} &= \mathbf{B}_f \mathbf{u} \\ \mathbf{y} &= \mathbf{H}_d \mathbf{w} + \mathbf{H}_v \dot{\mathbf{w}} + \mathbf{H}_a \ddot{\mathbf{w}} \end{aligned} \quad (2-16)$$

From Eq. 2-16, the acceleration can be expressed as below.

$$\ddot{\mathbf{w}} = -\mathbf{M}_{\text{st}}^{-1}\mathbf{C}_{\text{st}}\dot{\mathbf{w}} - \mathbf{M}_{\text{st}}^{-1}\mathbf{K}_{\text{st}}\mathbf{w} + \mathbf{M}_{\text{st}}^{-1}\mathbf{B}_{\text{f}}\mathbf{u} \quad (2-17)$$

Then, continuous-time state-space model is expressed as below.

$$\begin{aligned} \dot{\mathbf{x}}(t) &= \mathbf{A}_{\text{c}}\mathbf{x}(t) + \mathbf{B}_{\text{c}}\mathbf{u}(t) \\ \mathbf{y}(t) &= \mathbf{C}_{\text{c}}\mathbf{x}(t) + \mathbf{D}_{\text{c}}\mathbf{u}(t) \end{aligned} \quad (2-18)$$

where:

- $\mathbf{x}(t) = \begin{bmatrix} \mathbf{w}(t) \\ \dot{\mathbf{w}}(t) \end{bmatrix}$
- $\mathbf{A}_{\text{c}} = \begin{bmatrix} \mathbf{0} & \mathbf{I} \\ -\mathbf{M}_{\text{st}}^{-1}\mathbf{K}_{\text{st}} & -\mathbf{M}_{\text{st}}^{-1}\mathbf{C}_{\text{st}} \end{bmatrix}$
- $\mathbf{B}_{\text{c}} = \begin{bmatrix} \mathbf{0} \\ \mathbf{M}_{\text{st}}^{-1}\mathbf{B}_{\text{f}} \end{bmatrix}$
- $\mathbf{C}_{\text{c}} = [\mathbf{H}_{\text{d}} - \mathbf{H}_{\text{a}}\mathbf{M}_{\text{st}}^{-1}\mathbf{K}_{\text{st}} \quad \mathbf{H}_{\text{v}} - \mathbf{H}_{\text{a}}\mathbf{M}_{\text{st}}^{-1}\mathbf{C}_{\text{st}}]$
- $\mathbf{D}_{\text{c}} = \mathbf{H}_{\text{a}}\mathbf{M}_{\text{st}}^{-1}\mathbf{B}_{\text{f}}$

For example, in order to observe a displacement, $\mathbf{H}_{\text{d}} = \mathbf{I}$ and $\mathbf{H}_{\text{v}} = \mathbf{H}_{\text{a}} = \mathbf{0}$.

Therefore, \mathbf{C}_{c} and \mathbf{D}_{c} is $[\mathbf{I} \quad \mathbf{0}]$ and $\mathbf{0}$, respectively. The output influence matrix and direct-transmission term according to a considering response are listed in

Table 2-1

Table 2-1 Output influence matrix and direct-transmission term

Response	Influence matrix	Direct-transmission
Displacement	$\mathbf{C}_d = [\mathbf{I} \quad \mathbf{0}]$	$\mathbf{D}_d = \mathbf{0}$
Velocity	$\mathbf{C}_v = [\mathbf{I} \quad \mathbf{0}]$	$\mathbf{D}_v = \mathbf{0}$
Acceleration	$\mathbf{C}_a = [-\mathbf{M}^{-1}\mathbf{K} \quad -\mathbf{M}^{-1}\mathbf{C}]$	$\mathbf{D}_a = \mathbf{M}^{-1}\mathbf{B}_f$

The general solution of the continuous time dynamic system is as below:

$$\mathbf{x}(t) = e^{\mathbf{A}_c(t-t_0)}\mathbf{x}(t_0) + \int_{t_0}^t e^{\mathbf{A}_c(t-\tau)}\mathbf{B}_c\mathbf{u}(\tau)d\tau \quad (2-19)$$

In reality, all of input loading and output response change only at discrete sampling frequencies. Therefore, discretization is required with the transformation of continuous solution in Eq. 2-19 into discrete difference equations which is suitable for computation.

A zero-order hold (ZOH) is utilized to sample a discretized value from the continuous function $\mathbf{x}(t)$, assuming one sample per time interval T .

$$x_{ZOH}(t) = \sum_{n=-\infty}^{\infty} x(n) \cdot \text{rect}\left(\frac{t - T/2 - nT}{T}\right) \quad (2-20)$$

where $\mathbf{rect}(\cdot)$ indicates the rectangular function. In this concept, a function $\mathbf{x}(t)$ always gives time-invariant value for each time interval indicating that it would be considered as constant value $\mathbf{x}(k\Delta t) = \mathbf{x}(k)$.

Assuming zero-order hold for the input loading, the response at the time argument for $k\Delta t$ is obtained as follows.

$$\begin{aligned}
 \mathbf{x}(k+1) &= e^{\mathbf{A}_c \Delta t} \mathbf{x}(k) + \int_{k\Delta t}^{(k+1)\Delta t} e^{\mathbf{A}_c[(k+1)\Delta t - \tau]} \mathbf{B}_c \mathbf{u}(\tau) d\tau \\
 &\cong e^{\mathbf{A}_c \Delta t} \mathbf{x}(k) + \int_0^{k\Delta t} e^{\mathbf{A}_c \tau'} d\tau' \mathbf{B}_c \mathbf{u}(\tau) \\
 &= \mathbf{A}_d \mathbf{x}(k) + \mathbf{B}_d \mathbf{u}(k)
 \end{aligned} \tag{2-21}$$

$$\mathbf{y}(k) = \mathbf{C}_c \mathbf{x}(k) + \mathbf{D}_c \mathbf{x}(k) \tag{2-22}$$

where:

- $\mathbf{A}_d = e^{\mathbf{A}_c \Delta t}$
- $\mathbf{B}_d = \int_0^{\Delta t} e^{\mathbf{A}_c \tau'} d\tau' \mathbf{B}_c = \mathbf{A}_c^{-1} (\mathbf{A}_d - \mathbf{I}) \mathbf{B}_c$

In a discrete state-space model, the impulse response function can be obtained with a zero initial condition ($\mathbf{x}(0) = 0$) and unit pulse ($\mathbf{u}(0) = 1$, $\mathbf{u}(k) = 0$ for $k = 1, 2, \dots, n$) as follows:

$$\begin{aligned}
 \mathbf{x}(0) = 0 &\quad \Rightarrow \quad \mathbf{Y}_0 = \mathbf{D}_c \\
 \mathbf{x}(1) = \mathbf{B}_d &\quad \Rightarrow \quad \mathbf{Y}_1 = \mathbf{C}_c \mathbf{B}_d \\
 \mathbf{x}(2) = \mathbf{A}_d \mathbf{B}_d &\quad \Rightarrow \quad \mathbf{Y}_2 = \mathbf{C}_c \mathbf{A}_d \mathbf{B}_d \\
 \vdots &\quad \quad \quad \vdots \\
 \mathbf{x}(k) = \mathbf{A}_d^{k-1} \mathbf{B}_d &\quad \Rightarrow \quad \mathbf{Y}_k = \mathbf{C}_c \mathbf{A}_d^{k-1} \mathbf{B}_d
 \end{aligned} \tag{2-23}$$

where \mathbf{Y}_k = Markov parameter.

ERA procedure begins with constructing a Hankel matrix using Markov parameters $\mathbf{Y}(k)$ which contains modal properties as follows.

$$\mathbf{H}(0) = \begin{bmatrix} \mathbf{Y}_1 & \mathbf{Y}_2 & \mathbf{Y}_3 & \cdots & \mathbf{Y}_r \\ \mathbf{Y}_2 & \mathbf{Y}_3 & \mathbf{Y}_4 & \cdots & \mathbf{Y}_{r+1} \\ \mathbf{Y}_3 & \mathbf{Y}_4 & \mathbf{Y}_5 & \cdots & \mathbf{Y}_{r+2} \\ \vdots & \vdots & \vdots & \ddots & \vdots \\ \mathbf{Y}_p & \mathbf{Y}_{p+1} & \mathbf{Y}_{p+2} & \cdots & \mathbf{Y}_{p+r-1} \end{bmatrix} \quad (2-24)$$

The size of Hankel matrix is $pm \times qr$, where r is the number of inputs and m is the number of outputs. p and q are algorithm parameters which satisfy that condition $qr > pm$.

Substituting $\mathbf{Y}_k = \mathbf{C}_c \mathbf{A}_d^{k-1} \mathbf{B}_d$ into Eq. 2-24,

$$\begin{aligned} \mathbf{H}(0) &= \begin{bmatrix} \mathbf{C}_c \mathbf{B}_d & \mathbf{C}_c \mathbf{A}_d \mathbf{B}_d & \cdots & \mathbf{C}_c \mathbf{A}_d^{r-1} \mathbf{B}_d \\ \mathbf{C}_c \mathbf{A}_d \mathbf{B}_d & \mathbf{C}_c \mathbf{A}_d^2 \mathbf{B}_d & \cdots & \mathbf{C}_c \mathbf{A}_d^r \mathbf{B}_d \\ \vdots & \vdots & \ddots & \vdots \\ \mathbf{C}_c \mathbf{A}_d^{p-1} \mathbf{B}_d & \mathbf{C}_c \mathbf{A}_d^p \mathbf{B}_d & \cdots & \mathbf{C}_c \mathbf{A}_d^{p+r-1} \mathbf{B}_d \end{bmatrix} \\ &= \begin{bmatrix} \mathbf{C}_c \\ \mathbf{C}_c \mathbf{A}_d \\ \mathbf{C}_c \mathbf{A}_d^2 \\ \vdots \\ \mathbf{C}_c \mathbf{A}_d^{p-1} \end{bmatrix} \begin{bmatrix} \mathbf{B}_d & \mathbf{A}_d \mathbf{B}_d & \mathbf{A}_d^2 \mathbf{B}_d & \cdots & \mathbf{A}_d^{r-1} \mathbf{B}_d \end{bmatrix} \\ &= \mathbf{P}_p \mathbf{Q}_r \end{aligned} \quad (2-25)$$

Calculate the singular value decomposition of $\mathbf{H}(0)$:

$$\mathbf{H}(0) = \mathbf{R}_{2n} \boldsymbol{\Sigma}_{2n} \mathbf{U}_{2n}^T = \left[\mathbf{R}_{2n} \boldsymbol{\Sigma}_{2n}^{1/2} \right] \left[\boldsymbol{\Sigma}_{2n}^{1/2} \mathbf{U}_{2n}^T \right] \simeq \mathbf{P}_p \mathbf{Q}_r \quad (2-26)$$

To compute \mathbf{A}_d , Hankel matrix of $\mathbf{H}(1)$ is considered as below.

$$\begin{aligned} \mathbf{H}(1) &= \begin{bmatrix} \mathbf{Y}_2 & \mathbf{Y}_3 & \mathbf{Y}_4 & \cdots & \mathbf{Y}_{r+1} \\ \mathbf{Y}_3 & \mathbf{Y}_4 & \mathbf{Y}_5 & \cdots & \mathbf{Y}_{r+2} \\ \mathbf{Y}_4 & \mathbf{Y}_5 & \mathbf{Y}_6 & \cdots & \mathbf{Y}_{r+3} \\ \vdots & \vdots & \vdots & \ddots & \vdots \\ \mathbf{Y}_{p+1} & \mathbf{Y}_{p+2} & \mathbf{Y}_{p+3} & \cdots & \mathbf{Y}_{p+r} \end{bmatrix} \\ &= \begin{bmatrix} \mathbf{C}_c \mathbf{A}_d \mathbf{B}_d & \mathbf{C}_c \mathbf{A}_d^2 \mathbf{B}_d & \cdots & \mathbf{C}_c \mathbf{A}_d^r \mathbf{B}_d \\ \mathbf{C}_c \mathbf{A}_d^2 \mathbf{B}_d & \mathbf{C}_c \mathbf{A}_d^3 \mathbf{B}_d & \cdots & \mathbf{C}_c \mathbf{A}_d^{r+1} \mathbf{B}_d \\ \vdots & \vdots & \ddots & \vdots \\ \mathbf{C}_c \mathbf{A}_d^p \mathbf{B}_d & \mathbf{C}_c \mathbf{A}_d^{p+1} \mathbf{B}_d & \cdots & \mathbf{C}_c \mathbf{A}_d^{p+r} \mathbf{B}_d \end{bmatrix} \\ &= \mathbf{P}_p \mathbf{A}_d \mathbf{Q}_r \\ &= \left[\mathbf{R}_{2n} \boldsymbol{\Sigma}_{2n}^{1/2} \right] \mathbf{A}_d \left[\boldsymbol{\Sigma}_{2n}^{1/2} \mathbf{U}_{2n}^T \right] \end{aligned} \quad (2-27)$$

Finally, approximated \mathbf{A}_d to \mathbf{D}_d is obtained as follows.

$$\begin{aligned} \hat{\mathbf{A}}_d &= \mathbf{U}_{2n} \boldsymbol{\Sigma}_{2n}^{-1/2} \mathbf{H}(1) \boldsymbol{\Sigma}_{2n}^{-1/2} \mathbf{R}_{2n}^{-1} \\ \hat{\mathbf{B}}_d &= \text{the first } r\text{th column of } \mathbf{Q}_r (= \boldsymbol{\Sigma}_{2n}^{1/2} \mathbf{U}_{2n}^T) \\ \hat{\mathbf{C}}_d &= \text{the first } m\text{th row of } \mathbf{P}_p (= \mathbf{R}_{2n} \boldsymbol{\Sigma}_{2n}^{1/2}) \\ \hat{\mathbf{D}}_d &= \mathbf{Y}_0 \end{aligned} \quad (2-28)$$

Transform this system matrices into modal coordinates using eigenvector

Φ .

$$\begin{aligned}
\mathbf{A}' &= \mathbf{\Phi}^T \mathbf{A} \mathbf{\Phi} \\
\mathbf{B}' &= \mathbf{\Phi}^T \mathbf{B} \\
\mathbf{C}' &= \mathbf{C} \mathbf{\Phi} \\
\mathbf{D}' &= \mathbf{D}
\end{aligned}
\tag{2-29}$$

Finally, modal parameters can be obtained from the real and imaginary parts of the eigenvalues after transforming to the continuous model:

$$\begin{aligned}
s_i &= \sigma_i \pm \omega_{di} i \\
\xi_i &= -\frac{\sigma_i}{\sqrt{\sigma_i^2 + \omega_{di}^2}} \\
f_{di} &= \frac{\omega_{di}}{2\pi}
\end{aligned}
\tag{2-30}$$

2.2. Damping estimation of cable-stayed bridge

2.2.1. Bridge description: Jindo Bridge

The examined bridges (Figure 1-1) consist of two parallel cable-stayed bridges in a twin concept. There was a time interval between the construction of two bridges (Ju et al., 2015). The older bridge, hereafter referred to as Bridge 1, was built in 1984, and the newer bridge, hereafter referred to as Bridge 2, was opened to traffic in 2005 to accommodate the increased volume

of traffic on the bridge. Bridge 2, for which the VIV was observed, consists of main and side spans that are 74.25m-344 m-74.25m in length. The steel box girder provides two traffic lanes with a total width of 12.69 m and a height of 2.75 m. The external shapes, including guide vanes, of both decks are highly similar, as shown in Figure 2-1.

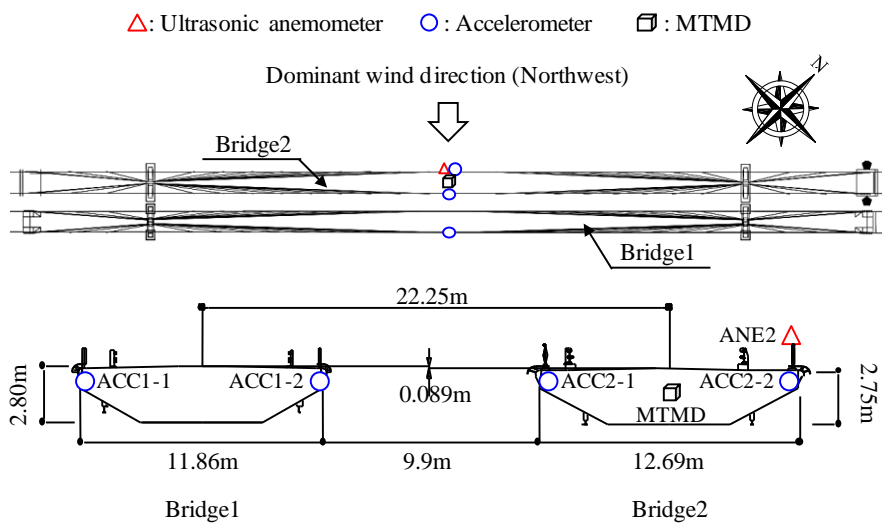


Figure 2-1 Deployment of the two bridges and built-in sensors

2.2.2. Monitoring data

The built-in sensors that are used to monitor the dynamic response of the bridge are shown in Figure 2-1. Acceleration was measured in gal (cm/s^2) with a sampling frequency of 100 Hz. The vertical accelerations of bridge deck were monitored at the center of the main spans in both bridges. Since the operational monitoring system was originally designed by the government

institute at the opening of the bridge to estimate the natural frequency in real time, the number of installed accelerometer was relatively low compared to the in-depth modal information. Wind direction and wind velocity were also recorded by ultrasonic anemometers that were installed on Bridge 2 and Bridge 1 at a height of 3m from the top of decks, respectively. Even though both anemometers were connected to the same data logger scanning 100Hz, the actual capacities of the sampling rate of the anemometers were 1Hz and 10Hz for Bridge 2 and Bridge 1, respectively. The wind data were measured by the anemometer located upstream of Bridge 2. In wind tunnel test measurements, the wind velocity at the anemometer position increased by about 10% compared to the free upstream velocity due to the local interference effect by the deck itself.

The acceleration data, recorded for 3 days starting on October 15 and 4 days on December 14, 2012, were utilized for an output-only modal analysis. In several studies, including those by James et al. (1992), Ill et al. (1993), Farrar and James (1997) and Farrar and Jauregui (1998), attempts were made to identify structural damping ratios under loading conditions of traffic and wind. Bridge 2 was also subjected to ambient loadings of normal traffic and wind during that period. For the operational modal analysis of Bridge 2, the measured acceleration and wind velocity was divided into 10-min segments.

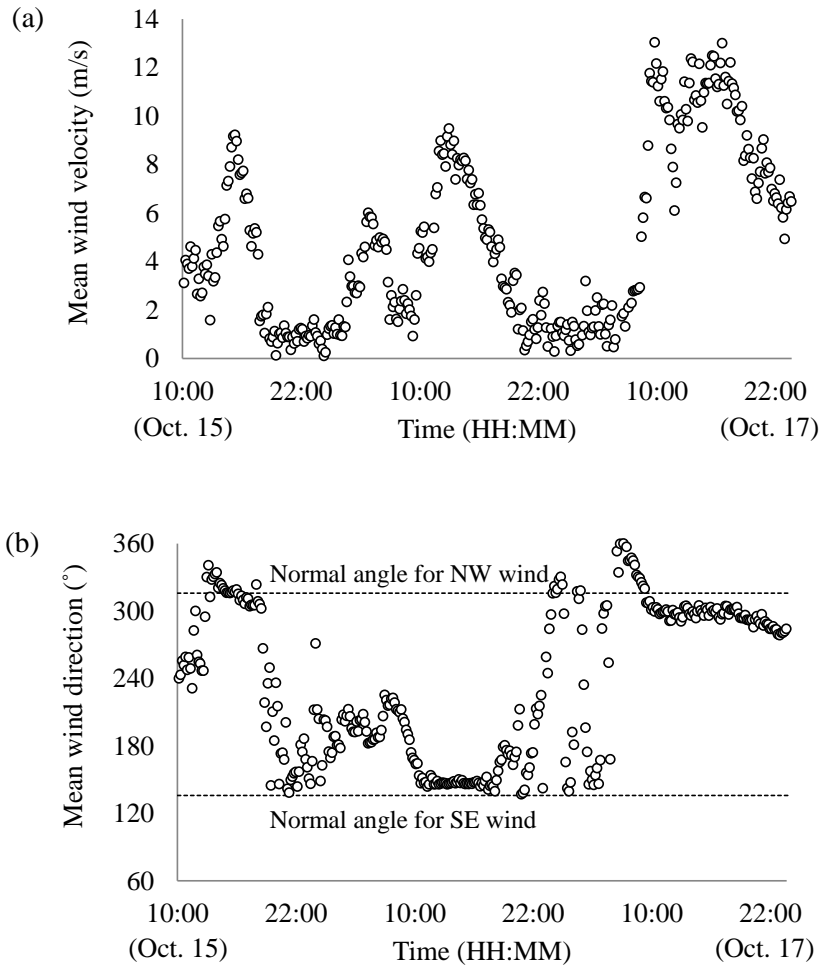


Figure 2-2 Wind properties for a three-day monitoring period: (a) 10-minute average wind velocity and (b) 10-minute average wind direction

Figure 2-2 showed the 10-minute average wind velocity and wind direction during the Oct. 15, 2012 to Oct. 17, 2012. The wind velocity was less than 13 m/s and the wind direction varied between Northwest (NW) and Southeast (SE). It is clear that most of the high winds were normal to the bridge decks.

2.2.3. Excitation test using TMD

As previously mentioned, the MTMD was installed inside the deck of Bridge 2 at the center of the main span in order to enhance a mechanical damping ratio. Figure 2-3 shows a part of the MTMD. The measured masses, natural frequencies, and damping ratios of four TMDs were 3787.3, 3261.3, 3185.3, 2981.8kg, 0.404, 0.423, 0.445, 0.461Hz, and 7.022, 8.178, 7.999 and 8.566%, respectively (HDEC, 2012) to satisfy the target damping ratio of 3.95% (HDEC, 2012).



Figure 2-3 The MTMD installed in the deck of Bridge 2

Seo (2015) performed a series of free vibration tests by utilizing one TMD as a mass vibrator. Four humans excited one TMD by pushing manually

manipulating it at its own natural frequency. The other TMDs, as well as the excited TMD, were fixed or released to obtain free-decaying signals after the bridge motion was developed to a certain sinusoidal level of motion with the first vertical natural frequency of the bridge, as shown in Figure 2-4. This excitation was realized without difficulty due to the tuned natural frequency of the exciting TMD to the target mode of bridge. Table 2-2 summarized the experimental condition of excitation test.

A narrow band-pass filter was applied to the free-decaying acceleration response and the logarithmic decrements were estimated from the exponentially fitted curves for both the positive and negative peaks.

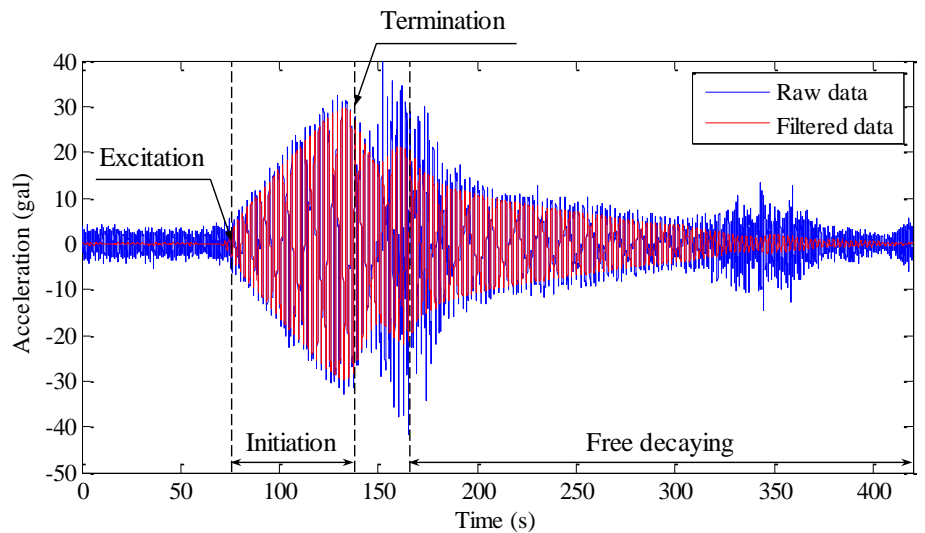


Figure 2-4 Time histories for the measured acceleration of the bridge deck during the free vibration test

Table 2-2 The experimental condition of excitation test

Case	TMD1	TMD2	TMD3	TMD4
Uncontrolled	Fixed	Fixed	Exciter and fixed	Fixed
Semi controlled	Fixed	Fixed	Exciter and released	Fixed
Fully controlled	Released	Released	Exciter and released	Released

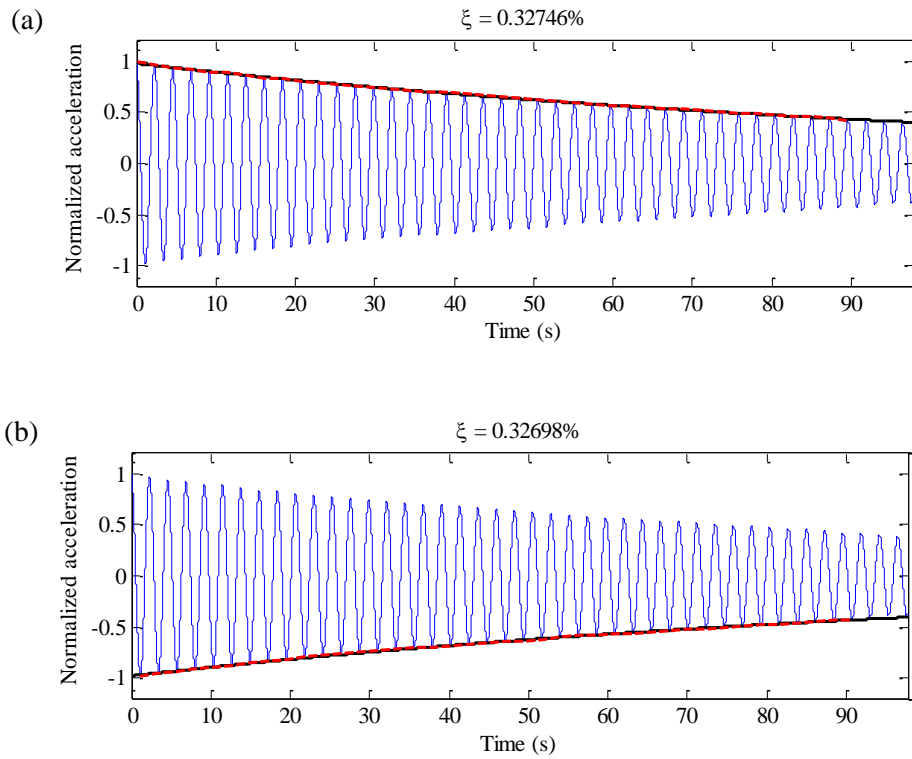


Figure 2-5 Estimated damping ratio via fitting an exponential function for uncontrolled case using (a) positive peaks and (b) negative peaks

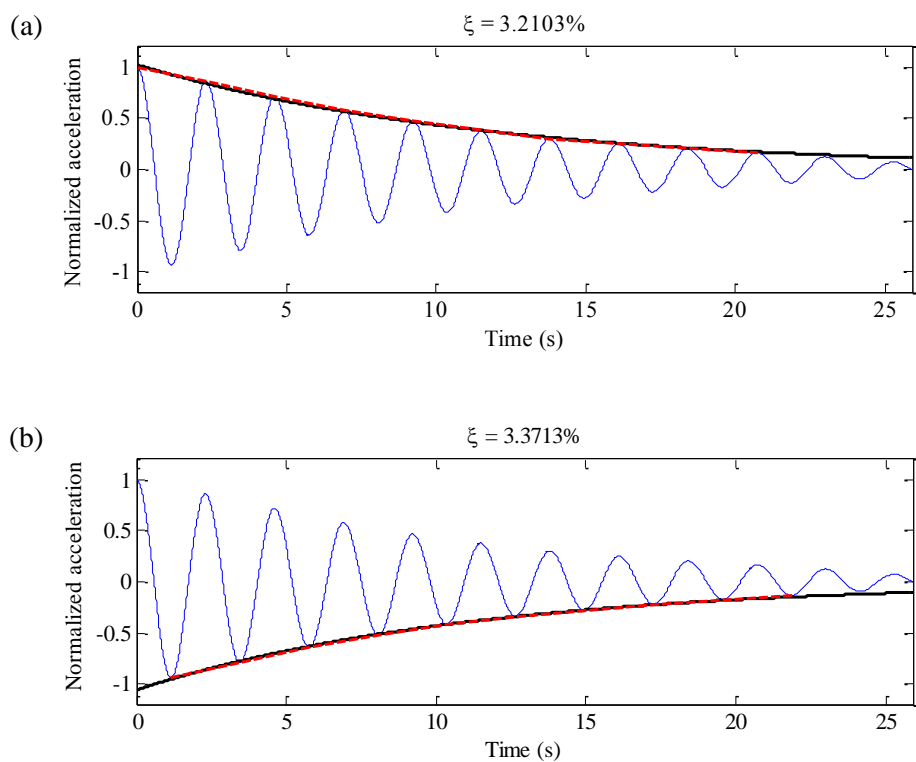


Figure 2-6 Estimated damping ratio via fitting as exponential function for semi-controlled case using (a) positive peaks and (b) negative peaks

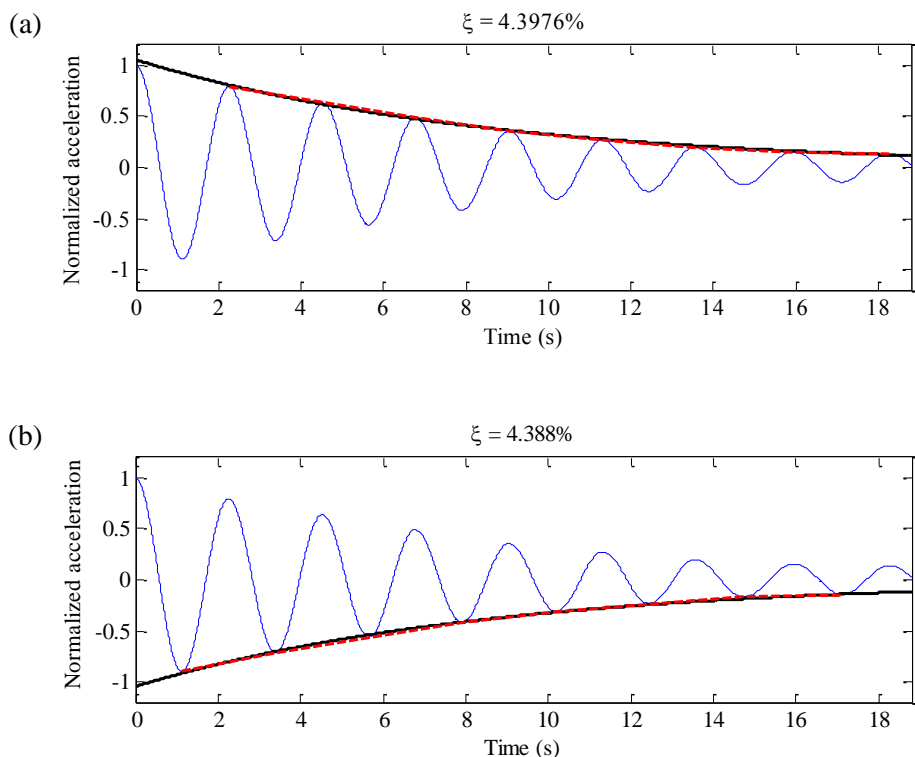


Figure 2-7 Estimated damping ratio via fitting as exponential function for fully controlled case using (a) positive peaks and (b) negative peaks

Figure 2-5~7 showed a successful fitting. The damping ratio was evaluated as 0.33% when all of the TMDs were fixed. This is much lower than the recommended damping ratio of 0.4 % for the wind-resistant design recommendations for a steel cable-stayed bridges (KSCE, 2006) and point out one of the sources of notable vibration in Bridge 2 in 2011 (Seo et al. (2013)). Here, the damping ratio is represented as a percent relative to the critical damping ratio. In a semi-controlled condition, the damping ratio increased as

a level of 3.2~3.4%. When all of TMDs were released for mitigating vibrations, the damping ratio was estimated to be 4.40% which slightly exceeded the target value of 3.95%.

2.2.4. Operational damping estimation using 3-days data

In order to estimate a damping ratio during operational condition, operational monitoring data accumulated for three days between 10-15 10:00 to 10-17 24:00 were utilized for the operational modal analysis. During the period, the bridges were subjected to ambient vibrations cause by the movement of traffic as well as ambient, daily winds. For evaluating the damping ratios of both bridges, the 10-min long data was utilized.

2.2.4.1. OMA based damping estimation

As previously mentioned in Section 2.1.1, the main algorithm of this study is a classical OMA, the Natural Excitation Technique (NExT) (Ill et al., 1993) combined with the Eigen Realization Algorithm (ERA) (Juang and Pappa, 1985; Caicedo, 2010; Caicedo et al., 2004) which was proven to be the suitable output-only system identification methods for the civil structures.

The auto correlation function or equivalently impulse response function in NExT was derived from an inverse Fast Fourier transform (FFT) of the

auto power spectral density (PSD) function of the vertical acceleration (Bendat and Piersol, 2000), as shown in Figure 2-8.

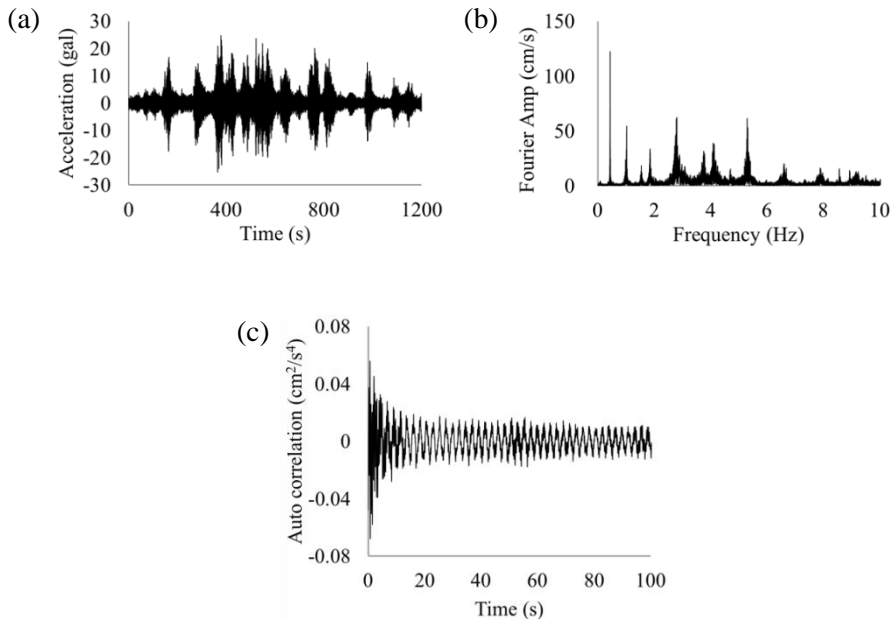


Figure 2-8 Measured vertical acceleration at the center of the main span of Bridge 2 during 12/10/15 13:40-14:00: (a) time history for 20 minutes, (b) PSD and (c) auto correlation function or equivalently impulse response function

The sample acceleration in Figure 2-8(a) is for a low wind velocity of 4m/s and mainly induced by vehicles that are crossing over the span. The amplitude of vibration exceeds 5 gal and the maximum value reaches 25 gal depending on the vehicle type. One excited signal lasts for 20 to 40 seconds which corresponds to the crossing time over the main span. The PSD of

acceleration in Figure 2-8(b) demonstrates the excitation of several modes by crossing vehicles. The auto correlation function in Figure 2-8(c) was obtained by the inverse FFT with the number of data for 2^{15} .

A model order equivalent to fifteen modes was employed in obtaining the dynamic properties of bridges, and only the first one corresponding to the first vertical mode was considered. The size of the Hankel matrix varies between 800×800 and $1,500 \times 1,500$ for the 100 Hz sampled auto correlation function.

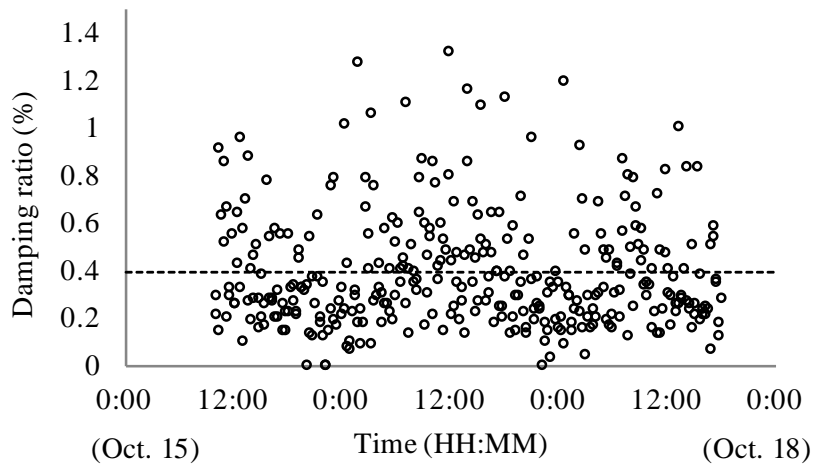


Figure 2-9 Estimated damping ratio for the first vertical mode of Bridge 2

The damping ratios of Bridge 2 were scattered between 0.02 % and 2.58 % with a mean value of 0.39 % and a coefficient of variation (COV) of 69.44%. Although the mean value of estimates was slightly high compared to the results of TMD excitation test of 0.33%, it was within acceptable range.

However, the main problem is scattering in the damping estimates. A large error bounds were observed in a distribution of estimate damping ratios as shown in Figure 2-9.

To stabilize several scattered estimates, a heuristic parameter selection was carried out with respect to a system order. A data length was increased into 20-minutes long data to secure more averages, and a Hamming window was used to calculate IRF with segment lengths of 2^{16} and a 50% overlap. Then, a system order of 15 was adjusted until the estimated damping ratio was stabilized.

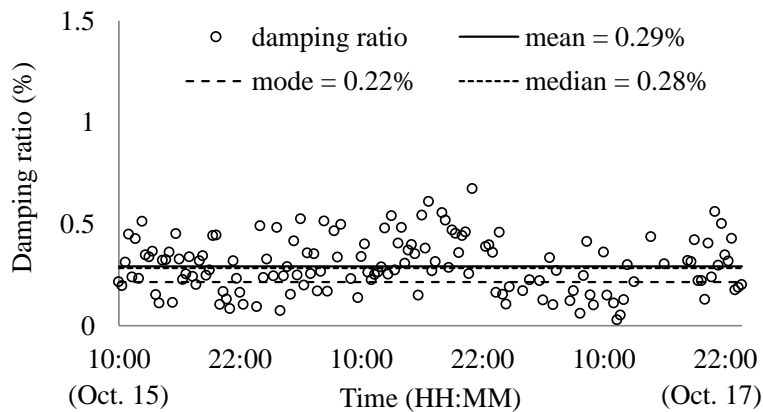


Figure 2-10 Estimated damping ratio for the first vertical mode of Bridge 2

Figure 2-10 illustrates the identified damping ratio of Bridge 2 after a heuristic parameter selection. The large scattering was significantly reduced compared to the result in Figure 2-9. The estimates were scattered between 0.1 % and 0.6 % with a mean value of 0.29 % and COV of 44.23%.

2.3. Concluding remarks

In order to estimate a damping ratio of Bridge 2 in Jindo Bridge, NExT-ERA was applied to ambient vibration data measured by operational monitoring system of Bridge 2. The preliminary damping estimation found that OMA was involved with a bias and variance error by a natural process. Between them, a bias error in estimated damping ratios can be removed by averaging of a large accumulated data set.

However, a challenging issue in a damping estimation is large scattering in a distribution of estimated damping ratios. A variance error in terms of large COV was significantly appeared in the result of OMA based damping estimation. Although this large error bounds in estimates can be reduced by heuristic decision of algorithm parameter, this approach is not suitable to treat a large accumulated data from operational monitoring system.

In order to apply a damping estimation algorithm to operational monitoring data in a real time without a heuristic process, the automation for proper parameter selection should be required.

Chapter 3

Automated proper parameter selection for NE_xT-ERA

Some parts of this chapter were reported in following journal publications:

Kim S-J, Kim H-K, Calmer R, Park J, Kim GS, Lee DK. Operational field monitoring of interactive vortex-induced vibrations between two parallel cable-stayed bridges. *Journal of wind engineering and industrial aerodynamics*. 2013;123:143-54.

Kim S, Park J, Kim H-K. Damping Identification and Serviceability Assessment of a Cable-Stayed Bridge Based on Operational Monitoring Data. *Journal of Bridge Engineering*. 2016:04016123.

3.1. Analysis parameter of NExT-ERA

OMAs are defined as ill-posed problem so that the results can be varied rapidly according to the minor changes in analysis parameters. Especially, NExT-ERA was non-structural model based scheme so that the analysis parameters should be selected more carefully for reliable identification.

As previously mentioned, NExT procedure estimates the impulse response function of structures from the similarity in formulation with the correlation functions of measured acceleration responses, based on the assumption of stationary white noise excitation (Caicedo, 2010; Ill et al., 1993). The correlation function is preferably obtained from an inverse Fast Fourier Transform (FFT) of the power spectral density function (PSD) considering computational efficiency (Davenport, 1991). Since the FFT algorithm was applied to a set of segmented sub-data obtained from all available data, the window size and the number of averagings can affect the results (Brincker et al., 1992). Accordingly, the length of the segmented data as well as the whole record length needs to be carefully selected.

The ERA procedure is used to identify modal parameters as the form of state-space matrices through the singular vector decomposition of the Hankel matrix obtained from impulse response functions. The size of Hankel matrix decided the number of points of (= the time length of) impulse response

function used to estimate modal properties. The system order, i.e., the number of expected modes also should be carefully selected for this procedure to ensure that stable and reliable modal parameters are obtained from a singular vector decomposition.

3.2. Parametric studies of numerical simulation

3.2.1. Description of the simulated models

This chapter presents a preliminary parametric study to examine the effect of analysis parameters on the accuracy of a modal analysis for selecting an appropriate range of parameters prior to the application to Bridge 2. A numerical simulation of ambient vibration test was performed based on 2-DOF model. The mass and stiffness matrices of Magalhães et al. (2010) was applied to the simulation with the damping matrix was viscous as shown in Table 3-1. The corresponding modal properties were listed in Table 3-2.

A total of 100 random white-noises loading for with a normally distributed random process were applied to both DOFs to replicate ambient vibrations. The discrete-time state-space model was implemented for the dynamic analysis to evaluate the structural acceleration responses with a sampling frequency of 100 Hz. A level of 10% random white noise to the maximum response was added to each simulated response.

Table 3-1 Structural properties of a 2-DOF model

Stiffness (kN/m)	Damping (kN-s/m)	Mass (ton)
$\begin{bmatrix} 100 & 0 \\ 0 & 100 \end{bmatrix}$	$\begin{bmatrix} 0.3275 & -0.0725 \\ -0.0725 & 0.3275 \end{bmatrix}$	$\begin{bmatrix} 1.25 & 0.25 \\ 0.25 & 1.25 \end{bmatrix}$

Table 3-2 Modal properties of a 2-DOF model

Parameters	1 st mode	2 nd mode
Natural frequency	1.2995Hz	1.5915Hz
Damping ratio	1.0410%	2.0000%
Mode shape	[1 1]	[1 -1]

3.2.2. Algorithmic parameters of NExT: NFFT and data length

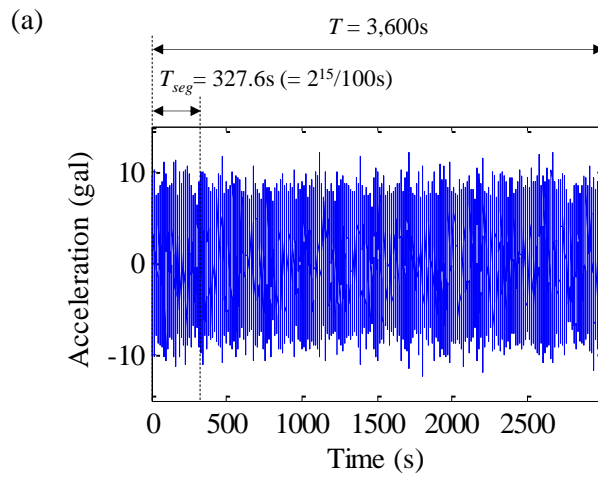
One of the key parameters for applying the NExT algorithm to the measured data is the window length (or time segment (T_{seg})), which is equivalent to dividing the number of FFT (NFFT) by the sampling frequency. The record length (T) is also a parameter that can affect NExT results in terms of the number of averagings. When 50% overlapping is assumed in segmenting data for consecutive FFTs, the length of the calculated impulse response function (T_{IRF}), the frequency resolution (df) and the number of averagings used in the spectral calculations (n_{avg}) can be represented with the algorithm parameters as below.

$$T_{IRF} = \frac{T_{seg}}{2} \quad (3-1)$$

$$df = \frac{1}{T_{seg}} \quad (3-2)$$

$$n_{aver} = \frac{2T}{T_{seg}} - 1 \quad (3-3)$$

Figure 3-1 illustrates a history of sample acceleration of a bridge deck upon excitation by an ambient loading and the corresponding correlation function obtained using the NExT algorithm. The parameters in Eqs. (3-1)~(3-3) are also illustrated in Figure 3-1. As shown in Figure 3-1(b), the correlation function for the measured acceleration clearly demonstrates a free-decaying signal as an impulse response function of the structural system.



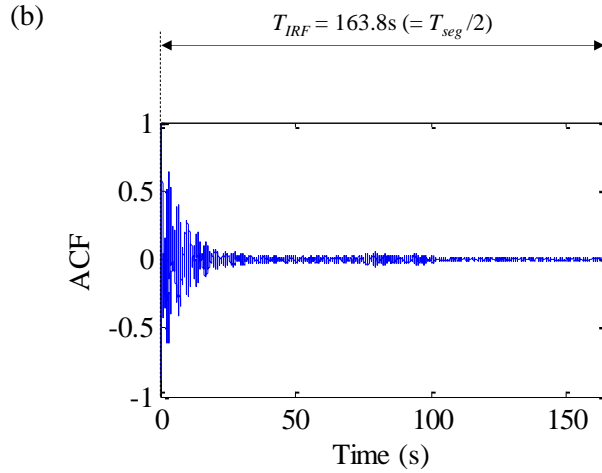


Figure 3-1 Definition of modal analysis parameters represented in (a) measured acceleration history of ambient vibration and (b) calculated correlation function

The damping ratio was identified from a calculated acceleration using NExT-ERA algorithm by considering a wide range of NFFT from 2^9 to 2^{18} for each acceleration response. Table 3-3 shows the modal analysis parameters that were determined according to a given NFFT and the total length of time. Each analysis parameter in Table 3-3 can affect the reliability of the identified damping ratio and the recommend ranges were selected as follows.

By considering the period of the lowest mode (1.0 s) for the model structure, the preferred length of the IRF was found to be 10 s or higher for securing at least motion 10 cycles with respect to the first mode (Rainieri and Fabbrocino, 2014). The difference in the natural frequencies between the two

modes was about 0.3Hz. In order to secure at least 20 divisions between two closely spaced frequencies, a frequency resolution of 0.015Hz or smaller would be preferable. Based on previous reports dealing with the NExT algorithm (Sim et al., 2011; Sim, 2011), the minimum averaging number can be preferably set to 10. Consequently, the case of NFFT=2¹³ (corresponding time segment = 81s) only satisfies all criteria for the three parameters for T=1,200s while the cases of 2¹³ to 2¹⁵ does so for T = 3,600s.

Table 3-3 List of parameters according to the selected NFFT

Power NFFT (2 ⁿ)	of T_{seg} (s)	df (Hz)	n_{aver}	
			T=1,200s	T=3,600s
7	0.64	0.7813	937	2,812
8	1.28	0.3906	468	1,406
9	2.56	0.1953	234	703
10	5.12	0.0977	117	351
11	10.24	0.0488	58	175
12	20.48	0.0244	29	87
13	40.96	0.0122	14	43
14	81.92	0.0061	7	21
15	163.84	0.0031	3	10
16	327.68	0.0015	1	5
17	655.36	0.0008	0	2
18	1310.72	0.0004	0	1

Appropriate NFFT also can be defined based on a random process theory. For the calculating PSD, a normalized bias error is evaluated as follows (Bendat and Piersol, 2000).

$$e_b[S_{xx}(f_n)] \approx -\frac{1}{3} \left(\frac{\Delta f}{B_r} \right)^2 = -\frac{1}{3} \left(\frac{\Delta f}{2f_n \xi_n} \right)^2 \quad (3-4)$$

where:

- Δf = frequency resolution
- B_r = bandwidth of target mode
- f_n = the modal frequency of target mode
- ξ_n = the modal damping ratio of target mode

To make the normalized bias error lower than 5%, frequency resolution should be smaller than $0.78f_n \xi_n$. The corresponding NFFT is as follow:

$$NFFT > \frac{1}{\Delta f \Delta t} = \frac{2.6}{B_r \Delta t} = \frac{1.3}{\xi_n f_n \cdot \Delta t} \quad (3-5)$$

For the case of the Bridge 2, a target frequency of first vertical mode is about 0.43Hz while damping ratio can be assumed as a level of 0.5~1.5% with sampling frequency of 100 Hz. Then, the required NFFT can be calculated as:

$$NFFT \geq \frac{1.3}{\xi_n f_n \cdot \Delta t} = 20,000 \sim 60,000 \quad (3-6)$$

This result, NFFT of 2^{15} to 2^{16} , is well matched with the result in Table 3-3. Keeping the preferred ranges of parameters in mind, the mean and COV of the identified damping ratios were calculated for 100 simulated cases for

each combination of NFFT and the total time length in Table 3-3. The results are shown in Figure 3-2.

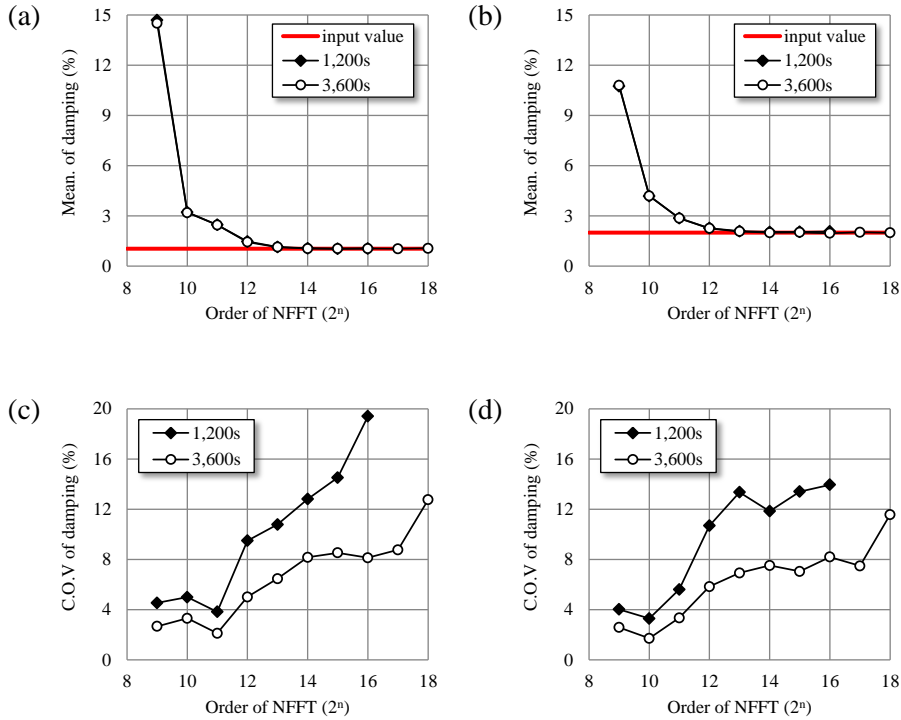


Figure 3-2 Estimated damping ratio according to NFFT: (a) mean of the first mode and (b) second mode, (c) COV of the first mode and (d) second mode

Initially, it was found that the mean value of the identified damping ratio is not affected by the data length or averaging number but is strongly influenced by the length of the IRF and frequency resolution. For the case of a NFFT from 2^9 to 2^{11} , the calculated PSD fails to estimate the Bell function properly, due to a low frequency resolution in all cases, irrespective of the time length. The estimated damping ratios of both modes converge to the

input value from $NFFT = 2^{13}$ (corresponding to the frequency resolution = 0.0122Hz) as expected from Table 4. On the contrary, the bias and variance depend on the averaging number. A longer period of data collection always leads to a stable estimation in all cases due to a high number of averagings. Small numbers of averaging such as 1 to 3 produce a 10% or higher COV, regardless of the total time length.

3.2.3. Algorithmic parameters of ERA: Size of Hankel matrix and system order

As previously mentioned, the size of Hankel matrix was associated with the utilized number points of impulse response function in a modal analysis. Since the end of the calculated IRF can include the erroneous term due to leakages in calculating PSD, the utilization only to the first few cycles of obtained IRF can enhance the accuracy of damping estimation (Rainieri and Fabbrocino, 2014). In addition, it should be noted that a low-rank Hankel matrix could be a reason of missing the target mode. Caicedo (2010) recommended that as much number of IRF from the spectral density function as possible without including noisy signals is required for a successful damping identification. Therefore, the size of Hankel matrix should be determined based on the number of points available in the calculated IRF.

This chapter presents a study of appropriate length of IRF based on 2-DOF numerical simulation. The damping ratio was identified with a variation of the utilized length of IRF from 2 seconds to 30 seconds as shown in Figure 3-3. A total simulation time was 3,000 seconds with NFFT of 2^{15} . For each length of IRF, a total of 100 simulations were performed by 100 reproduction of a normally distributed random loading.

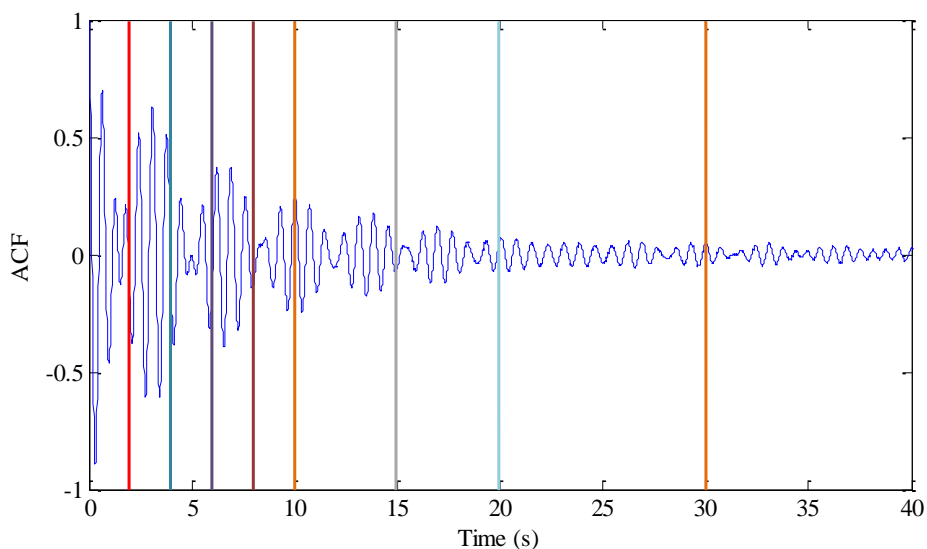


Figure 3-3 Calculated impulse response function and the utilized time length

Figure 3-4 illustrated the mean and COV of estimated damping ratios corresponding to the utilized time length of IRF. As can be seen, too short or too long utilized time of IRF caused a bias and variance error in a damping estimation. The mean of estimated damping ratios was closed to the theoretical value with the smallest COV under the utilized time of 6 to 10

seconds (the corresponding cycles of the length of 6 to 10 seconds was 4 to 7 for each mode).

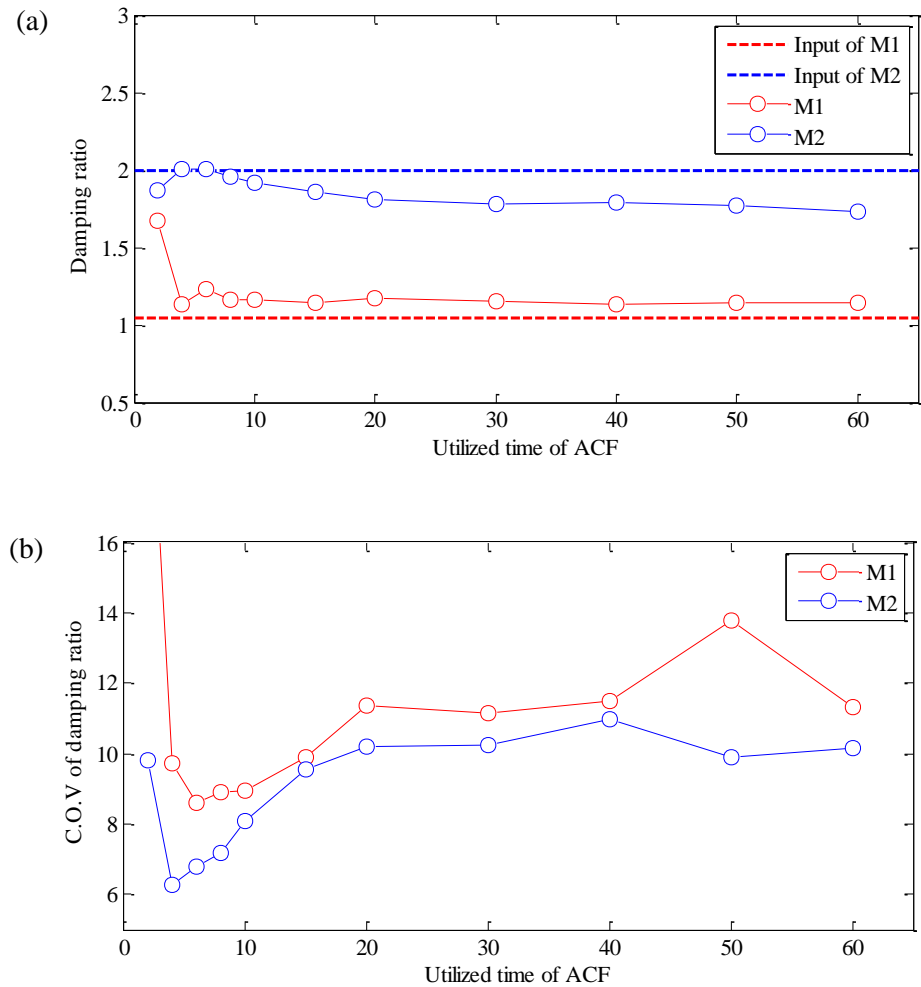


Figure 3-4 (a) Mean value and (b) COV of estimated damping ratio according to utilized time of impulse response function

A system order can be chosen from the number of poles in the calculated PSD (Caicedo, 2010; Zhang, 2012). The rank of the Hankel matrix also

indicates a system order. The rank corresponds to the number of non-zero singular values, which can be determined from the pattern of a rapid drops in the distribution of singular values (Fu and He, 2001; Chiang and Lin, 2010). A stabilization diagram can also be utilized to evaluate the appropriateness of the chosen system order by examining the presence of and variations in the number of poles for the focusing modes in ERA (Caicedo, 2010).

In order to produce reliable modal properties, an iterative procedure for determining system order is proposed based on the utilization of a stabilization diagram followed by a sensitivity analysis. First, the process of modal identification is repeated with a step-by-step increase in the system order from 1 to 50. A total of three criteria are proposed to determine whether the trial system order is acceptable or not. The first criterion is to check whether the identified natural frequency for the targeting first vertical mode is in an acceptable range, for example, between 0.43Hz and 0.46Hz. The second criterion is to check whether the identified damping ratio is at least greater than zero. The third criterion is to confirm that the calculated Extended Modal Amplitude Coherence (EMAC), a measure of how accurately a particular mode projects forward onto the impulse response data (Pappa et al., 1992), is greater than 99%, which indicates that the identified mode matches the target mode. If any of these three criteria are not satisfied, then the identified modes

are discarded. The iterative process continues by increasing the system order by 1 until the maximum number of system order is encountered. As a result, only the identified target modes which satisfy all criteria remain.

In a basic approach, the iteration was terminated when the identified first vertical mode satisfies all criteria of target mode. As a result, we can find a minimum system order required to identify the first vertical mode without including fictitious modes. However, as previously mentioned, the iteration process can be terminated without convergence in some cases. To overcome this limitation, in the newly proposed method, a sensitivity analysis with respect to a system order is performed at the end of the entire iterative process to select a converged value. To secure a converged damping ratio automatically, the median value of the recorded damping ratios as a successful identification is selected as a representative damping ratio.

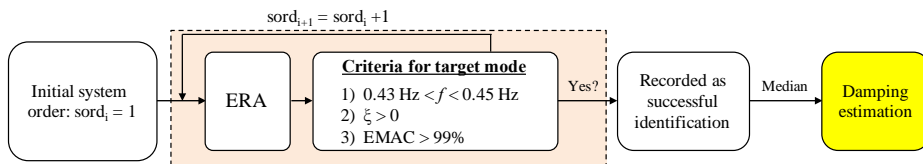


Figure 3-5 A newly proposed procedure to select a converged damping ratio

The sensitivity of damping estimation corresponding to a system order was examined using numerical simulation with a NFFT of 2^{15} , the time length of the simulated acceleration of 3,600s and the length of utilized IRF of 10

second.

As shown in Figure 3-6, the estimated damping ratios were not sensitive to a variation of system order compared to other analysis parameters in a numerical simulation since a numerical model was simple compared to real structures. Therefore, it should be studied more extensively in the following section.

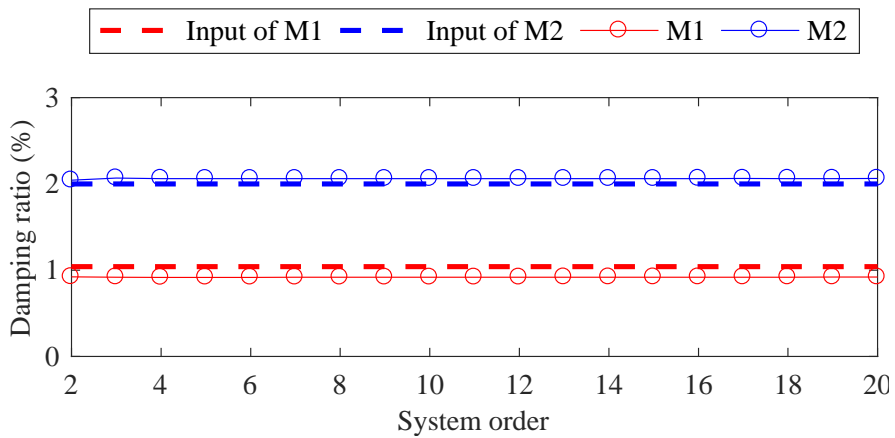


Figure 3-6 Estimated damping ratio according to a system order

3.3. Parametric studies using field monitoring data

To validate the result of numerical simulation in a real structure, the sensitivities of the algorithm parameters on the identified damping ratios were investigated by varying the analysis parameters for 1-day monitoring data, obtained on Dec, 16. The variations in the identified damping ratios were estimated in terms of mean and COV.

3.3.1. NFFT and the record length

To deal with a trade-off between the frequency resolution and the number of averagings, the data sets were prepared for record lengths of 20, 40, and 60 min. The NFFT and the corresponding number of averagings are summarized in Table 3-3

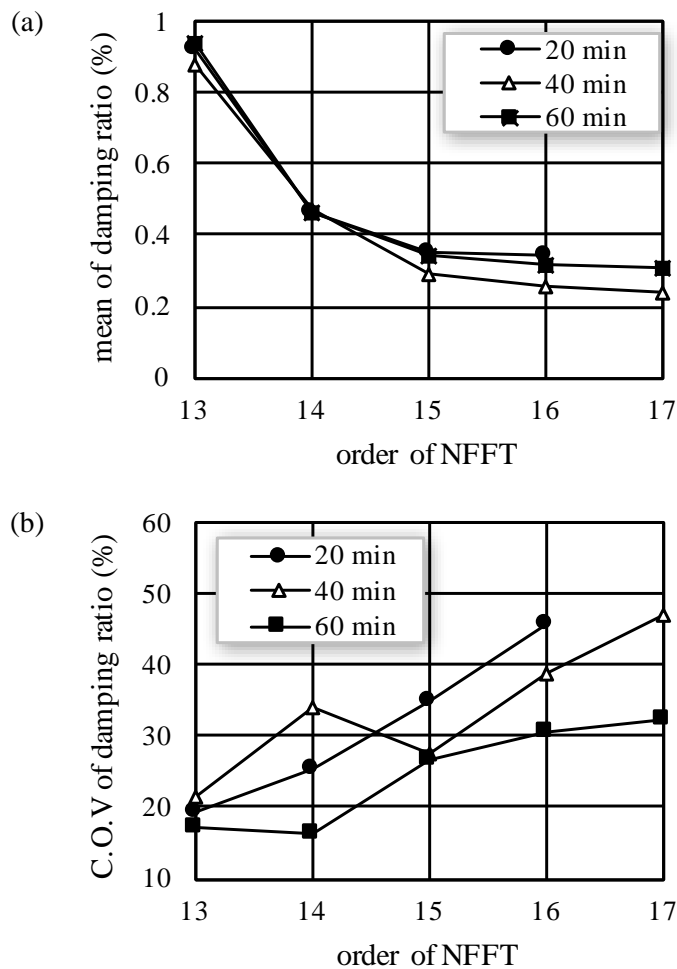


Figure 3-7 Estimated damping ratio according to NFFT and record length: (a)

mean of the damping ratio and (b) COV of the damping ratio

As shown in Figure 3-7, for a given record length, the estimated damping ratio demonstrates the dependencies to the chosen NFFT. As NFFT increases by over 2^{15} , the estimated damping ratios converge to a specific value in all of record length. On the contrary, the COV of the identified damping ratios generally increases due to reduced averaging number with larger NFFT. Among them, a longer record length reduced a scattering in damping estimation due to increasing the number of performed averages. The COVs of record length of 60 min were smaller than other record length cases in all of NFFT case, indicating more reliable estimations.

Therefore, it is required a sufficient NFFT of 2^{15} to reduce a bias error in estimated damping ratios with a longer data of 60 min to decrease a variance error with a sufficient averaging number.

3.3.2. Size of Hankel matrix

The bias and variance error of estimated damping ratios according to the size of Hankel matrix are plotted in Figure 3-8. As can be seen, a small or large Hankel matrix representing a short or long IRF utilizing caused a bias and variance error in damping estimation. After a utilized length of IRF of 5 seconds, the bias and variance error was minimized that was well agreed with the result of numerical simulation.

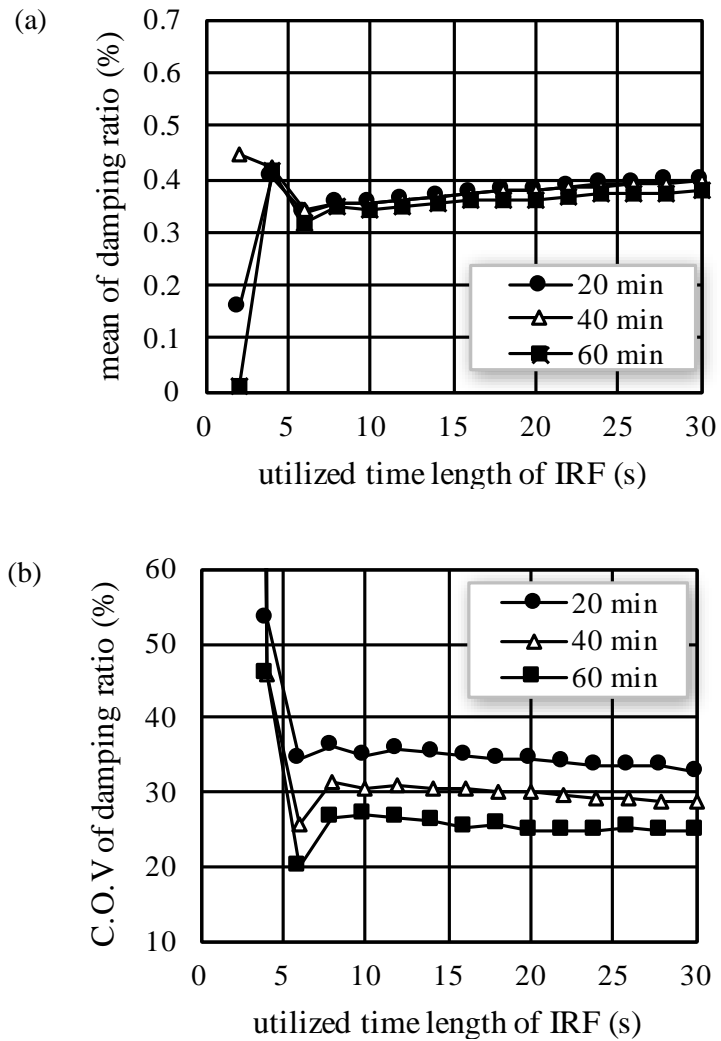


Figure 3-8 (a) mean and (b) COV of estimated damping ratio according to utilized length of IRF

3.3.3. System order

Figure 3-9 shows a distribution of estimated damping ratios at Oct. 16 10:00AM according to a system order.

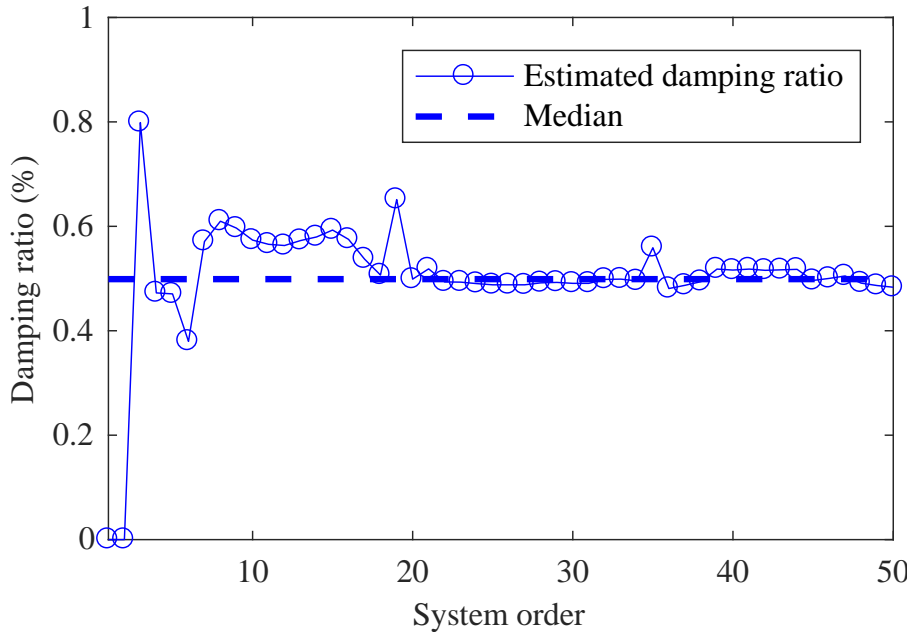


Figure 3-9 Estimated damping ratio according to system order (Oct. 16 10:00AM)

As can be seen, a first trial (system order = 1) failed to identify a target mode. From the second trial, of which system order increased to 2, the modal properties of identified mode satisfied the criteria of target mode. However, this value was overestimated compared to the converged value. This case is an example that an iteration could be terminated but convergence has not been achieved. After a system order reached to 19, the identified damping ratio converged to the certain value. Nevertheless, in some cases after convergence has been achieved, a number of erroneous estimations were still observed such as the system order of 20 or 35.

It is clear that a damping estimation was sensitive to the corresponding system order, and converged to the certain value. Furthermore, even if the convergence was achieved, an over/underestimation could be observed in a certain system order. Therefore, to avoid the uncertainty due to the poor selection of system order, it was recommended to select the median value of the damping estimates satisfying the criteria of target mode as a representative damping ratio.

3.4. Application: Jindo Bridge

3.4.1. Parameter selection

Based on the extensive studies in Section 3.3, a total of four analysis parameters were determined as below procedure.

Data length

The extensive parametric studies found that the longer record length of data provides more stable estimations of the identified damping ratio with lower values for both the bias factor and COV due to increasing of averaging number in the NExT procedure, a record length of 60 min was used for identifying the damping ratios.

NFFT

NFFT should be selected to obtain a sufficient the length of IRF, a frequency resolution and the number of averagings. The numerical simulations and field monitoring data found that NFFT of 2^{14} to 2^{15} with 50% overlapping was appropriated for the case of 60 min data with sampling frequency of 100 Hz. On the basis of the aforementioned investigations, $\text{NFFT} = 2^{15}$ was adopted for the acceleration response of $T = 60$ min. A Hanning window with a length of 2^{15} was applied with an overlapping of 50% in calculating the correlation function by the inverse FFT of a corresponding PSD function calculated by Welch's method. With these NFFT and record lengths, the corresponding parameters for the NExT procedure were determined to be $T_{seg} = 327.68\text{s}$, $T_{IRF} = 163.84\text{s}$, $df = 0.0031\text{Hz}$ and $n_{avg} = 21$. These parameters would be expected to provide a fine frequency resolution to permit the target mode to be accurately identified and a sufficient averaging number to permit bias error or the scattering of the estimated damping ratio to be reduced.

Size of Hankel matrix

In practice, the Hankel matrix should be determined according to a shape of calculated IRF. For example, a case of lower frequency and higher damping ratio required a longer IRF to secure sufficient cycles since a correlation

function would decay slowly. Therefore, a size of Hankel matrix should be determined based on a decaying shape of IRF which was determined by the modal properties of system. To obtain a much data number without noisy data at the end of IRF, the consistent part of the decaying free vibration signals was utilized as shown in Figure 3-10.

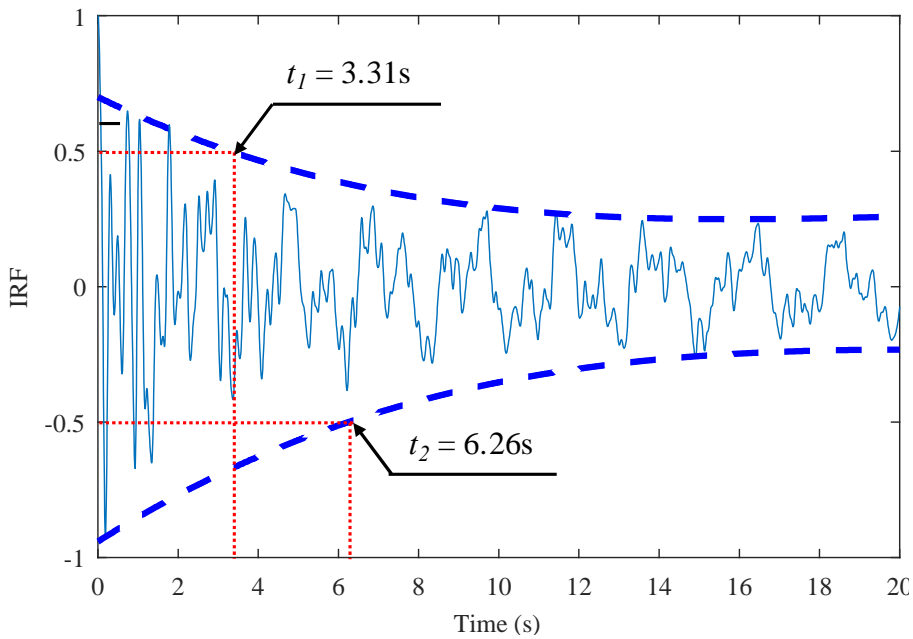


Figure 3-10 Determining a utilized time length of IRF based on envelope function

At first, find the time when a calculated IRF decreases as a level of 50% utilizing the positive/negative envelope function of IRF ($t_1 = 3.31s$, $t_2 = 6.26s$). Next, select a longer one (6.26 s) between two times. In addition, a previous researches showed that a utilized length of IRF of 5 to 15 seconds was

suitable to obtain a reliable damping estimation which contains about 3 to 10 cycles of target modes. Therefore, if the selected time was out of range (5 to 15 seconds), it should be modified to accordingly. In this case, 6.26 second was within in 5 to 15 seconds so that the size of Hankel matrix was determined as 300 by 300.

System order

A damping estimation was very sensitive to a system order. In order to obtain a converged damping ratio, a system order was selected based on a concept of stabilization diagram and its median value. A series of modal analysis was performed for all range of the system order from 1 to 50, and recorded the identified first vertical mode which satisfies the criteria (frequency range, EMAC and physically reliable damping ratio). Then, the median value of the identified damping ratios was selected as a representative value.

3.4.2. Estimated damping ratio after proper parameter selection

The operational monitoring data, which were already utilized in Section 2.2.4, were used to estimate a damping ratio during operational condition. Figure 3-11 illustrates the estimate damping ratio according to parameter

selection. White circles (denoted as ‘Basic’) indicated the estimated damping ratios of Section 2.2.4, and black circles (denoted as ‘Proper parameter selection’) meant the result after a proposed parameter selection procedure in Section 3.3.

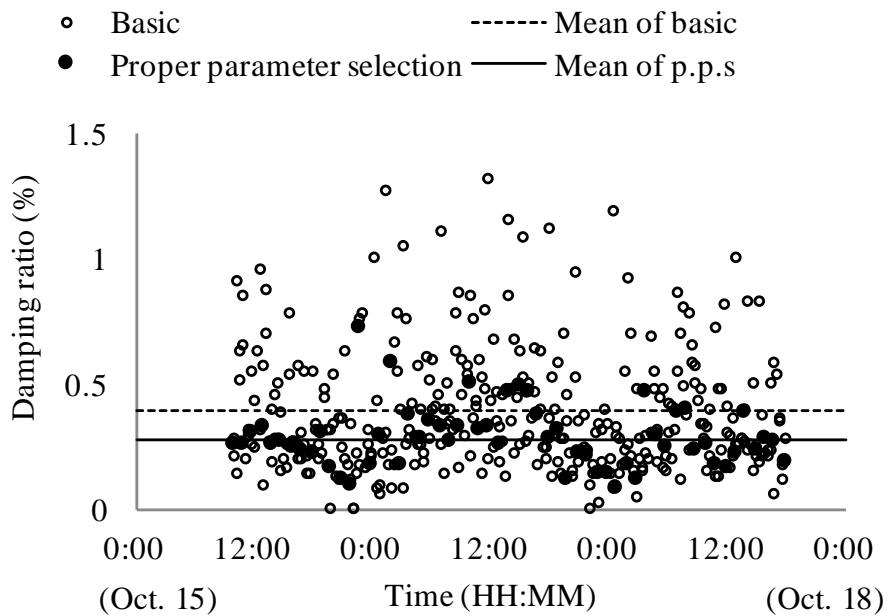


Figure 3-11 Estimated damping ratio of Jindo Bridge corresponding to proper parameter selection

As can be seen, a large scattering in damping estimates due to the over/underestimated damping ratio was significantly reduced. By applying a proper parameter selection, a mean value of estimated damping ratios slightly decreases from 0.37% to 0.28%, while COV dramatically reduced from 69.44% to 43.29%, which was acceptable value compared to the COV of heuristic

parameter selection. It is clear that the proposed proper parameter selection of NFFT, data length, size of Hankel matrix and system order was automated as well as effective to enhance the accuracy of damping estimation based on operational modal analysis.

3.4.3. Computational cost

In order to obtain the median value of estimated damping ratios corresponding to system order, OMA should be repeated as a times of considering system order. Before that, iteration was terminated when one of the identified modes satisfies the criteria of target mode. It indicates that the computational cost of OMA would increase with more iteration.

Figure 3-12 illustrates a distribution of estimated damping ratio and elapsed time corresponding to parameter selection method. As can be seen in Figure 3-12(a), the identified mode with the system order of 8 satisfied all criteria at first. In Figure 3-12(b), ‘Basic’ indicates a procedure without selecting a median value so that iteration was terminated at the system order of 8, and the corresponding elapsed time was 0.361 seconds. ‘Proper parameter selection’ continued iterative process by increasing the system order by 1 until the maximum number of system order was encountered. When the maximum number of system order specified was 50, a total elapsed

time was 5.04 seconds. Although it was 13.97 times of basic case, this consuming time can be acceptable compared to the total time length of the measured acceleration, 60 minutes.

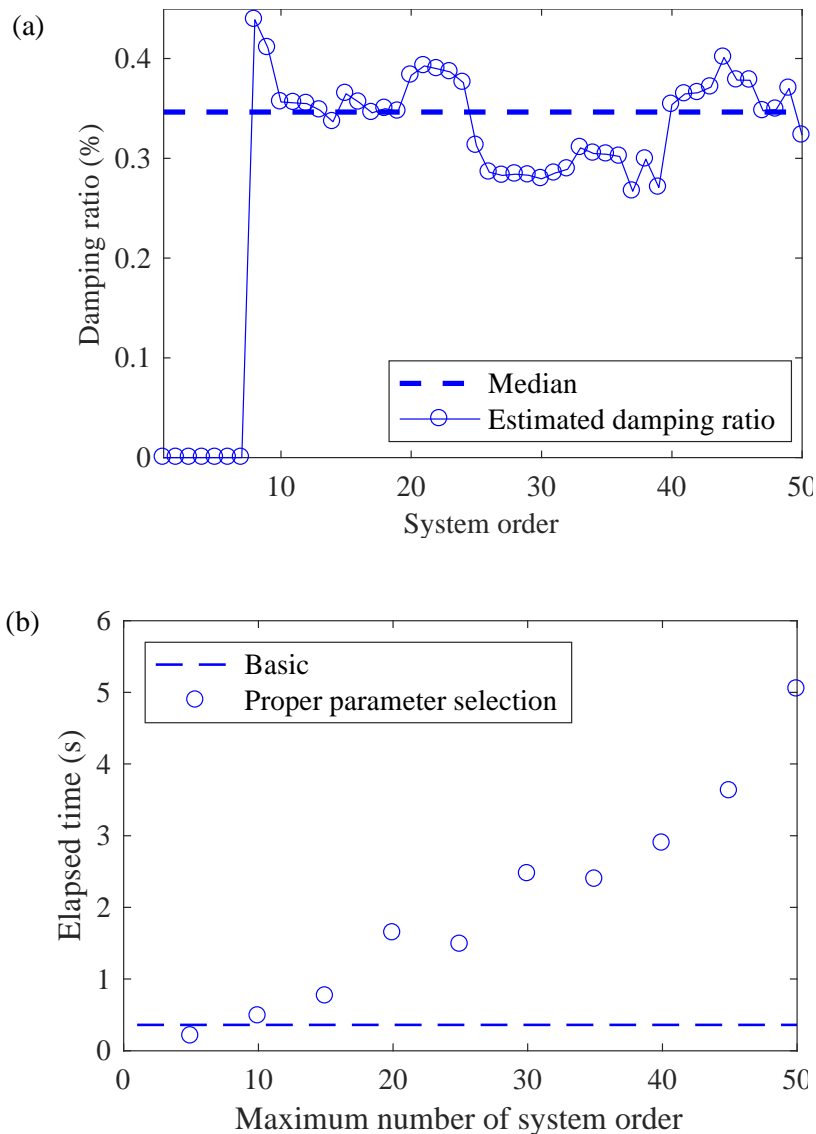


Figure 3-12 (a) Estimated damping ratio according to system order and (b) elapsed time according to the maximum number of system order

Chapter 4

Signal stationarization for traffic-induced vibration

Some parts of this chapter were reported in following journal publications:

- Kim S, Park J, Kim H-K. Damping Identification and Serviceability Assessment of a Cable-Stayed Bridge Based on Operational Monitoring Data. *Journal of Bridge Engineering*. 2016:04016123.
- Kim S, Kim H-K. Damping Identification of Bridges under Nonstationary Ambient Vibration. *Engineering*. 2017 (under review)
- Kim S, Kim H-K, Hwang YC. Enhanced Damping Estimation for Cable-Stayed Bridges from Operational Monitoring Data. *Structural Engineering International*. 2018. (submitted)

4.1. Introduction

One of the reasons for uncertainty in OMA based damping estimation is nonstationary in loading. OMA, which was performed without loading information, generally assumes that the input loading is stationary Gaussian white noise. In reality, however, the nonstationary loadings such as earthquake, extreme wind or traffic loading were mainly applied to civil structures, and it causes nonstationary responses (Feng et al., 2006; Guo et al., 2012; Lin and Chiang, 2013). Thus, this strong violation of excitation condition for the basic assumption of classical OMA can be a reason for a poorly damping estimation.

Traffic loads, are the main loading source for bridges (Kim and Kawatani, 2008; Kim et al., 2005), and these can be expressed as a stationary random process since the roughness of a road is modeled as a zero-mean stationary Gaussian random process (Guo and Xu, 2001). However, when traffic volume is low, an ambient vibration signal at the sensor position is seen as an envelope as a vehicle approaches and fades away. The traffic-induced vibration observed at a specific position can be read as a nonstationary process that is expressed as a product of stationary white noise and an envelope-like function (Sun et al., 2015). As a result, the accelerations of loads across a bridge subjected to traffic loads were localized (Guo and Xu, 2001) for specific positions.

Traffic loading usually excites the structural modes that correspond to vehicle frequencies. The Ontario Code (1991) recommends increasing the amplification factor when the dominant natural frequencies of a structure range from 2~5 Hz, and AASHTO specifies that the frequency of general trucks should be 2.5 Hz (Bartos, 1979). Bartos (1979) also suggests that the dynamic amplification effect could exceed limitations when the structural frequencies are between 1.5-5 Hz. The vehicle-bridge interaction also is distorted by driving frequencies, which are dependent on the duration of a vehicle crossing a single stringer (Lin and Yang, 2005; Majka and Hartnett, 2008). Brewick and Smyth (2014) discovered that these distortions of modal information increase the uncertainty of damping estimation based on OMA schemes.

The chapter focuses on the nonstationarity due to traffic loading and its effect on OMA-based damping estimation. The effect of traffic loading was examined via the field-measured data from a suspension bridge as shown in Figure 4-1. A signal stationarization algorithm was proposed by introducing an amplitude-modulating (AM) function, and this was applied to the operational monitoring data obtained from a suspension bridge for damping estimation.

4.2. Experimental investigation for TIV properties

4.2.1. Bridge description: Sorok Bridge

The Sorok Bridge in Figure 4-1 is a self-anchored mono-cable suspension bridge. The bridge has a total length of 470 m, which consists of a 250-m center span and two symmetric side spans of 110 m. The total width of its steel box girders is 15.7 m, which provides two traffic lanes. The bridge was opened to traffic in March, 2009. Since then, a series of dynamic tests have been carried out for detailed inspections and model updates for maintenance.



Figure 4-1 View of the Sorok Bridge

Table 4-1 summarizes the modal frequencies of the bridge, as identified by OMA using FDD of the data obtained from ambient vibration testing (AVT). Table 1 also includes the calculated natural frequencies obtained from the updated finite element model based on manual tuning and a parameterized sensitivity-based model updating approach (Park et al., 2012; Park et al., 2015). The coincidences between measured and calculated frequencies are shown in Table 4-1.

Table 4-1 The modal frequencies of the Sorok Bridge

Mode	AVT (2016)	Updated model (MAC)
VS1	0.406 Hz	0.403 Hz (0.991)
VS2	0.478 Hz	0.463 Hz (0.968)
VS3	0.839 Hz	0.829 Hz (0.984)
L1	0.521 Hz	0.521 Hz (0.993)
T1	1.550 Hz	1.530Hz (0.990)

4.2.2. Monitored data

The utilized sensors are displayed in Figure 4-2. Two accelerometers (EQK_SRRZ, EQK_SRQZ) were calibrated at the center of the deck to measure the vertical acceleration of the deck with a sampling frequency of 100 Hz. The corresponding displacement of the deck was simultaneously measured using a laser displacement transducer (DIS001_Z, DIS002_Z) equipped as a built-in sensor for the monitoring of the operational behavior of

the bridge. Wind direction and wind velocity were recorded via an ultrasonic anemometer (WGT001) installed on the bridge deck. The available data were divided into 10-min intervals for an in-depth investigation.

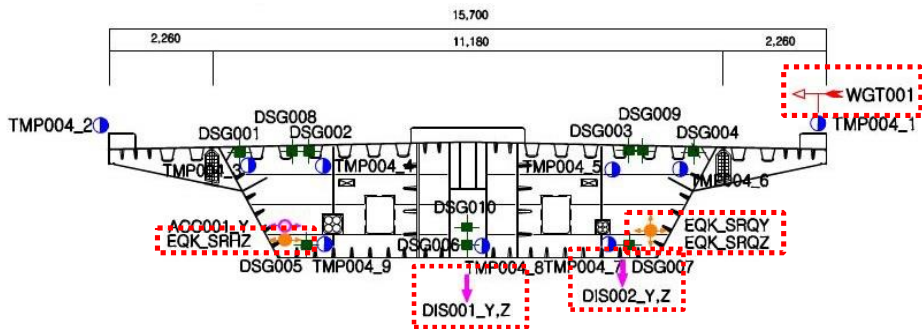


Figure 4-2 Utilized sensors in the monitoring system at the center of the mid span of the Sorok Bridge

4.2.3. Experimental condition

Even though the field tests were basically planned to secure data from AVT, a heavy truck was also prepared create the high-level excitation of an operating condition. A series of measured accelerations from the suspension bridge were analyzed to confirm the properties of the traffic-induced vibration (TIV). In particular, two types of testing — a truck loading test and an ambient vibration test using normal vehicles — was considered to investigate the characteristics of TIV according to different types of vehicles. The truck-loading test was performed using a three-axle truck with a total mass of 25

tons as shown in Figure 4-3 at speeds of 25 and 40 km/h. The bridge was not closed to normal traffic, but this would have been relatively minor in weight compared with the truck and would have been of little value in investigating truck-induced vibration.

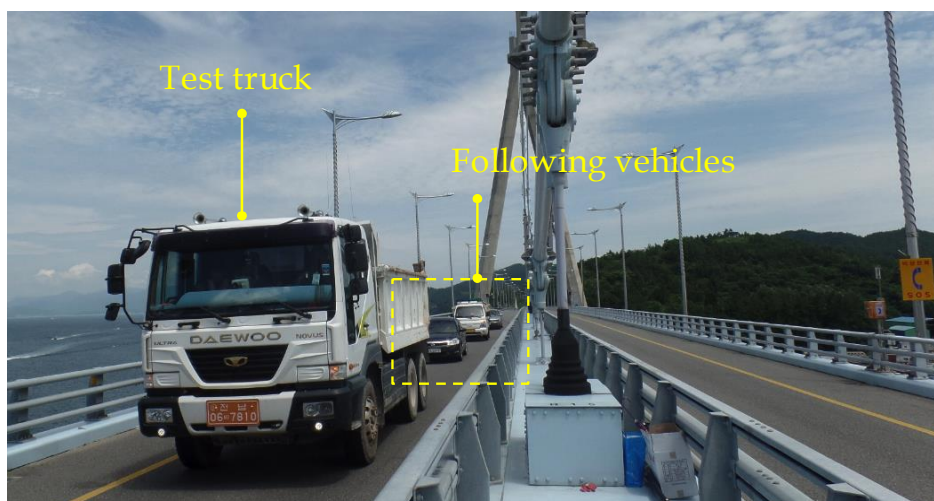


Figure 4-3 A truck loading test

A measured displacement and corresponding acceleration at the main span of investigated bridge are displayed in Figure 4-4(a). As expected, the vertical acceleration responses were localized during the vehicles passed the concerned measuring point, and it caused a nonstationary trend in response due to vehicles. Figure 4-4(b) shows the mean, standard deviation and kurtosis of the acceleration calculated in windows of 20 seconds with 10 seconds overlapping. The kurtosis, which was used to evaluate the

nonstationarity in signal, increased rapidly when the traffic passed the concerning point.

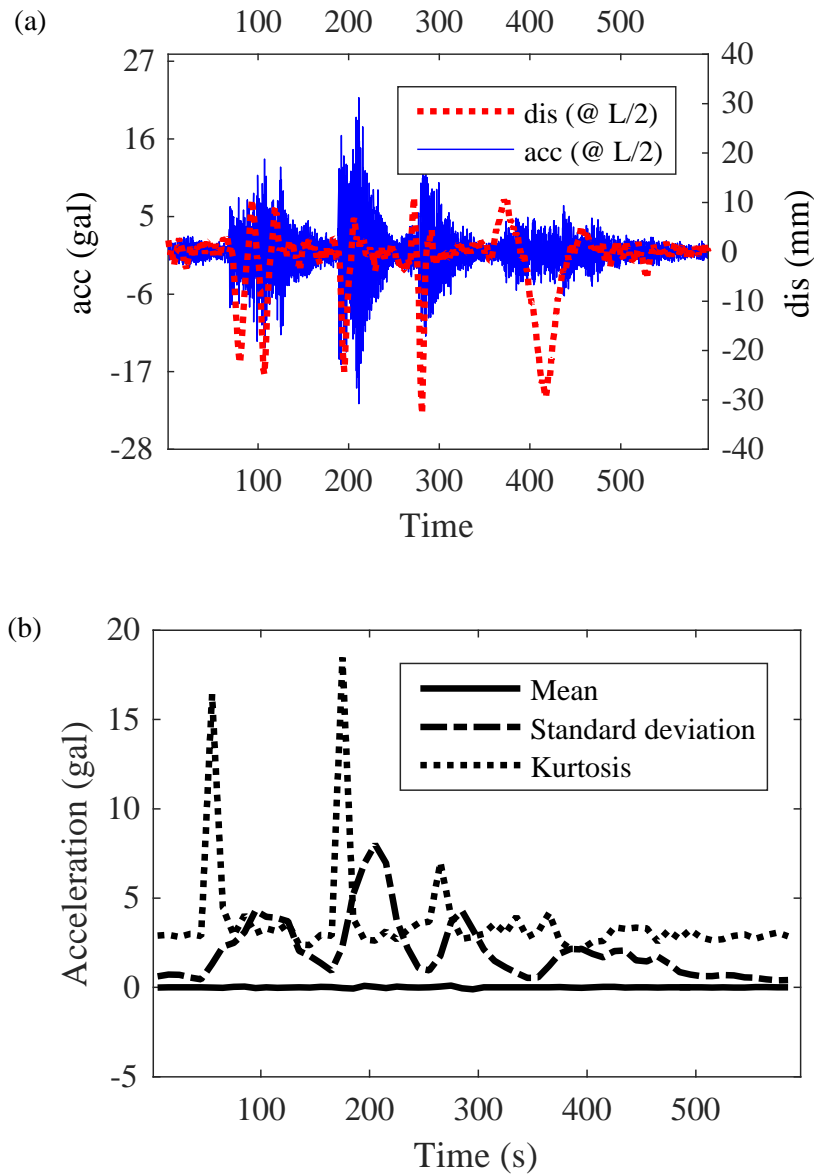


Figure 4-4 (a) Measured displacement and acceleration at the center of mid span and (b) moving mean, standard deviation and kurtosis of (a)

4.2.4. Nonstationary effect of TIV on a measured signal

To examine the nonstationary effect caused by traffic loading, a stationary response was utilized as a reference, which satisfied the assumptions of classic OMA. To select a stationary response from among the set of operational monitoring data, the kurtosis value was evaluated for a series of acceleration data. The kurtosis value data were lower than 10 and contained no peak responses that could be classified as stationary (Guo, 2015). In particular, the highest RMS acceleration was selected to represent the stationary data in order to secure a high signal-to-noise ratio.

The TIV data statistics are summarized in Table 4-2. As shown in Table 4-2, the TIV data induced by the truck loading were referred to as ‘heavy truck’ while the accelerations measured during normal operations were classified as ‘ordinary vehicle’.

Table 4-2 Classification of data utilized

	Stationary excitation	Heavy truck	Ordinary vehicle
RMS acceleration	0.49	2.61	1.74
MAX acceleration	2.98	21.82	26.08
Kurtosis	4.17	12.47	49.69
Mean wind velocity	8.81	6.91	2.43

The stationary excitation data shown in Figure 4-5 has no extreme peaks

due to passing vehicles while the kurtosis value was identified as 4.17, which indicates stationary status. The PSD shows that the main structural modes, the 1st (0.415Hz) and 3rd vertical modes (0.844Hz) were dominant.

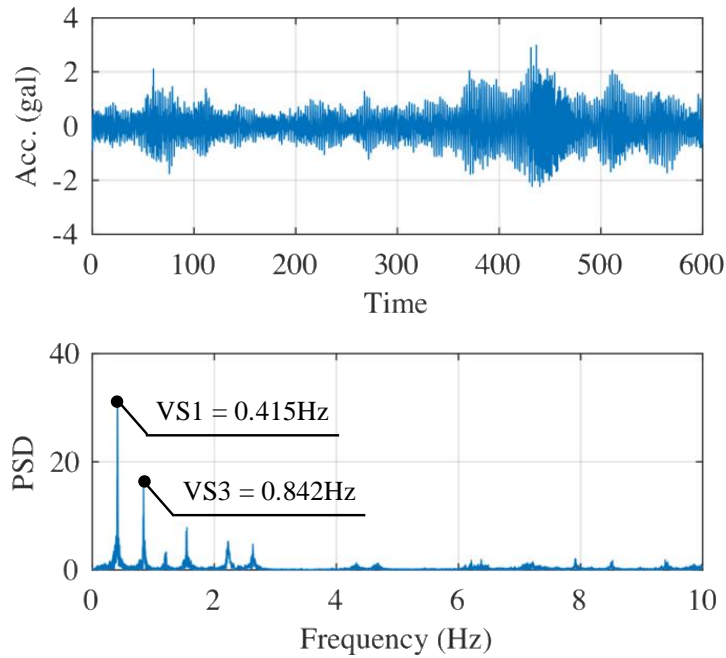


Figure 4-5 The measured acceleration and its PSD of stationary excitation

On the contrary, as shown in Figure 4-6, the structural modes around 2Hz were amplified when a heavy truck passed over the bridge. As a truck entered the main span, the amplitude increased gradually, and this invoked a nonstationary response. The kurtosis value was 10.70, which exceeded the criterion for a stationary mode.

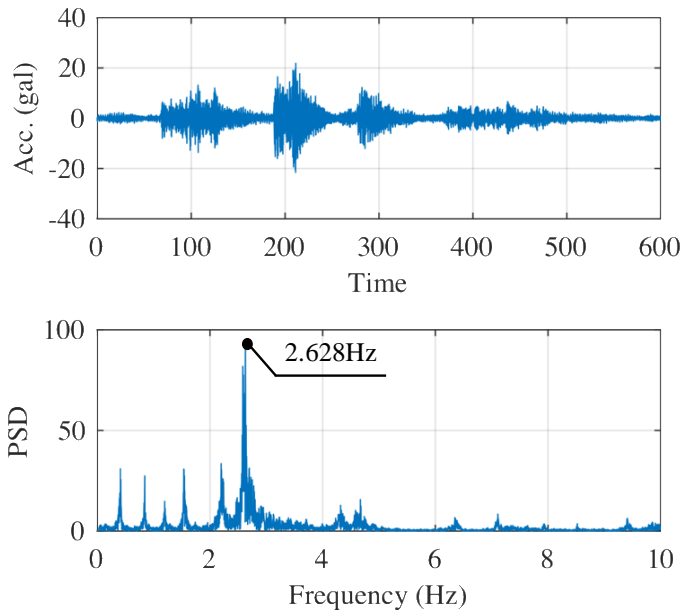


Figure 4-6 The measured acceleration and its PSD under heavy truck

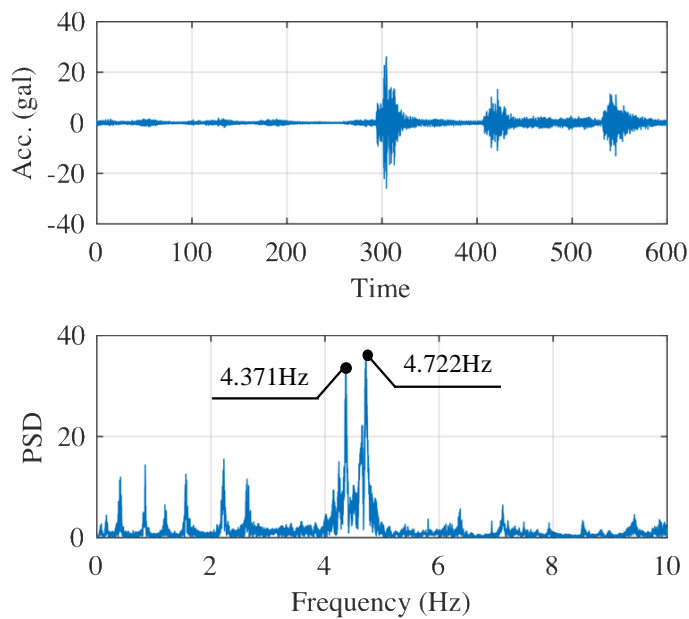


Figure 4-7 The measured acceleration and its PSD under ordinary vehicle

Ordinary vehicles also amplified a higher mode of structures compared with a stationary mode, as shown in Figure 4-7. The structural modes around 4-5 Hz were excited by lighter vehicles that excited relatively higher frequencies. The kurtosis value was 49.68, which also exceeded the stationary criterion of 10, and indicated a nonstationary mode.

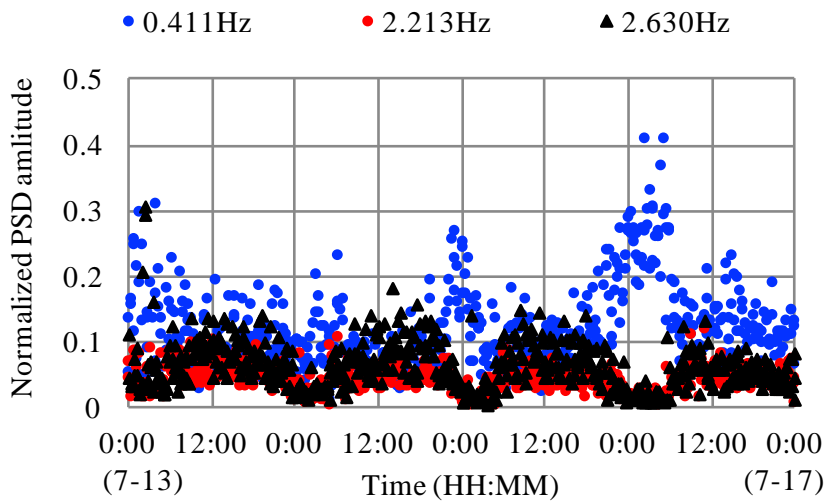


Figure 4-8 Normalized PSD amplitude of first vertical mode and structural modes within 2-3 Hz

In order to show the variance of dominant mode with respect to time, the normalized PSD amplitude of a total of three modes are presented in Figure 4-8. For this purpose, a series of each PSD was normalized to a length of 1 (2-norm). After this normalization, the corresponding PSD amplitude of 0.411 Hz (first vertical mode), 2.213 Hz and 2.630 Hz (the structural modes within

vehicle frequency of 2~3 Hz) were recorded. Figure 4-8 supposed that the modes of 2~3 Hz were dominant during from morning till night, in the case of large traffic volume. At dawn, the bridge was empty of vehicles, and accordingly, the first vertical mode became the most dominant mode for ambient vibration.

Figure 4-9 presents the time-frequency distribution. The measured acceleration of 10 minutes was considered as shorter segments of equal length and then the Fourier transform was performed separately on each shorter segment. With a normalization of 2-norm, some peaks cannot be found in a time-frequency distribution since the vibration amplitude of measured acceleration was relatively too low during the midnight to dawn. To overcome this, the calculated PSD was normalized to a maximum value of 1 in this case.

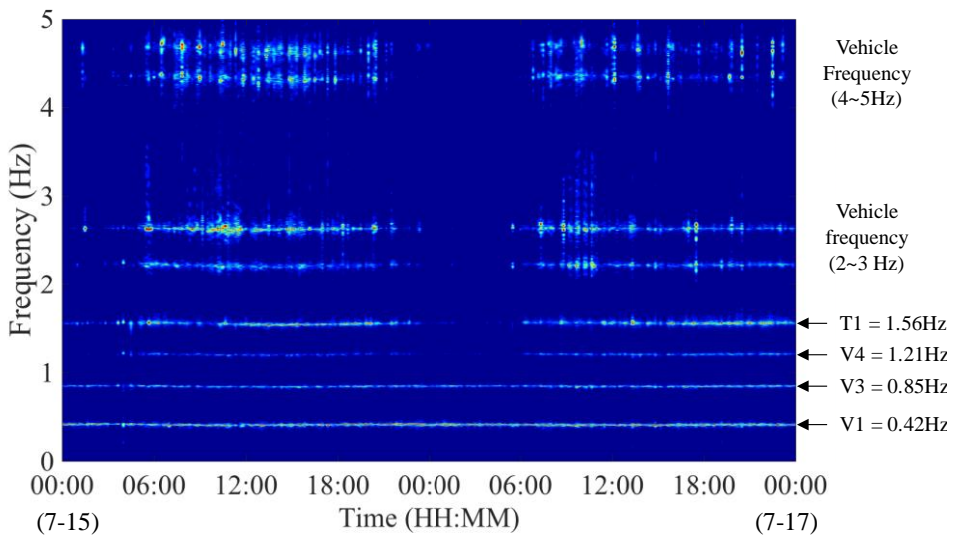


Figure 4-9 Time-frequency distribution of Jul. 15 to 17

These figures also clearly show that the higher structural modes presumably arose from the traffic-induced vibration. Especially, compared to the lower structural mode, the frequencies of higher modes arose by traffic-induced vibration was scattered. It is noted that the vehicle frequency had a wide frequency range corresponding to vehicle type, so the excitation of vehicles also had a broad-banded excitation for vehicle frequencies (2~5 Hz).

4.3. Signal stationarization using amplitude-modulating function

4.3.1. Amplitude-modulating function

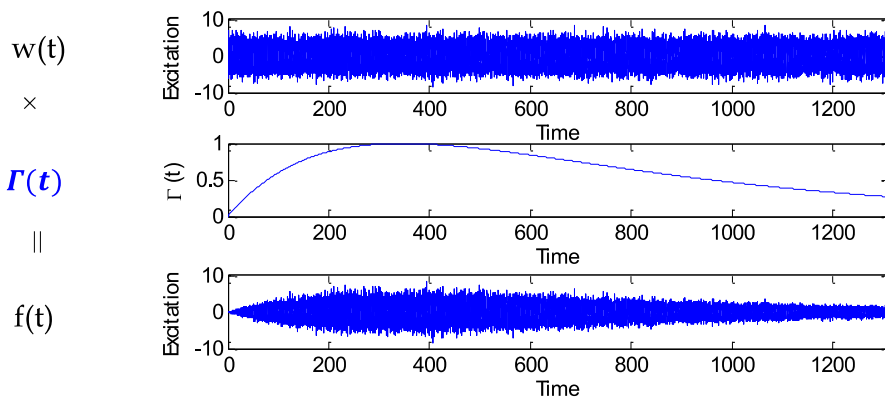


Figure 4-10 A brief concept of nonstationary process modeling

Chiang and Lin (2008) proposed a method for identification of modal parameters from response data gathered from a structure under nonstationary ambient vibration. As shown in Figure 4-10, nonstationary ambient excitation

can be modeled as a product of white noise and the amplitude-modulating function (AM function), $\Gamma(t)$, as follows.

$$f(t) = \Gamma(t)w(t) \quad (4-1)$$

If the AM function is slowly time-varying function, the nonstationary responses $a(t)$ also can be expressed as a product form of AM function and stationary response $\ddot{v}(t)$ as follows.

$$a(t) \simeq \Gamma(t)\ddot{v}(t) \quad (4-2)$$

As for the stationary process, this can be approximated from the nonstationary response via modulation with the AM function $\Gamma(t)$. The AM function can be evaluated from the temporal root-mean-square of nonstationary data (Newland, 2012). This temporal root-mean-square function can be evaluated by moving averaging method for the squared sample record as expressed below

$$\Gamma(t) = C \sqrt{\frac{1}{T_w} \int_{t-T_w/2}^{t+T_w/2} a^2(\tau) d\tau} \quad (4-3)$$

where C is the expectation of square root for the ergodic process part and T_w is the segment length for temporal RMS. Finally, we can obtain the

approximate stationary process by dividing the measured response by envelop AM function.

4.3.2. The optimal segment length for signal stationarization

The main parameter of temporal RMS is the segment length (T_w). If the segment length is too short, the calculated amplitude-modulating function fluctuates as the frequency of target mode. It leads to distort the target mode in stationarized acceleration. Figure 4-11 shows the calculated amplitude-modulating function using moving RMS of $T_w = 0.1s$. As can be seen, the red line which indicates the AM function vibrates with respect to the frequency of the measured acceleration.

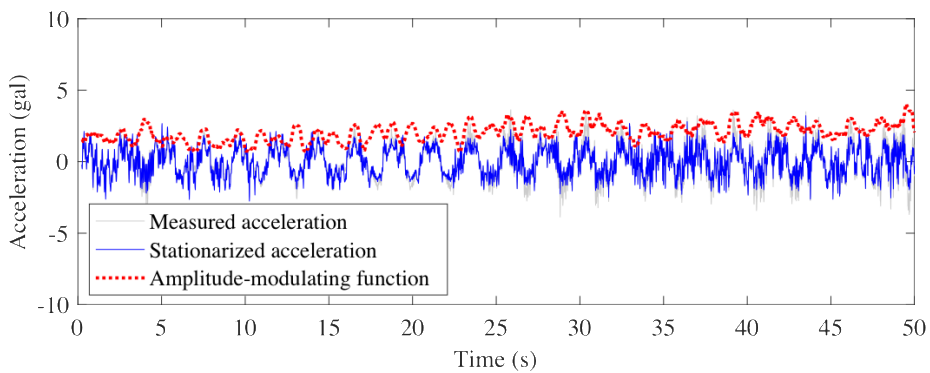


Figure 4-11 The calculated AM function using moving RMS ($T_w = 0.1s$)

To minimize this fluctuating term in moving RMS, theoretical moving RMS value in single sinusoidal function was introduced as follows.

$$y(k\Delta t) = \sqrt{2} \cos(2\pi f_n k\Delta t) \quad (4-4)$$

With the segment length, the temporal moving RMS of Eq. 4-4 can be derived as

$$Y_{\text{RMS}}^2 = \frac{1}{T_w} \sum_{k=0}^{T_w-1} (\sqrt{2} \cos(2\pi f_n k\Delta t))^2 \quad (4-5)$$

$$Y_{\text{RMS}}^2 = 1 + \frac{1}{T_w} \sum_{k=0}^{T_w-1} \cos 2(2\pi f_n k\Delta t) \quad (4-6)$$

Since the theoretical RMS value of single sinusoid is 1, the summation term in Eq. 4-5 can be considered the “error of moving RMS” resulting in the fluctuating part which can be zero when the ratio between segment length and natural period (T_w/T_n) is $0.5n$ ($n \in \mathbb{N}$). Figure 4-12 shows the moving RMS of the 0.5Hz single sinusoid according to the segment length. As can be seen, when the ratio between segment length and natural period (T_w/T_n) is $0.5n$ ($n \in \mathbb{N}$), the error is zero regardless of time evolution.

In real cases, the measured data is not a single sinusoid but a combination of the sinusoids of several frequencies. Furthermore, the natural frequency of each mode usually changes according to the environmental factors. Therefore, a minimum segment length that reduces overall errors below a certain level must be determined.

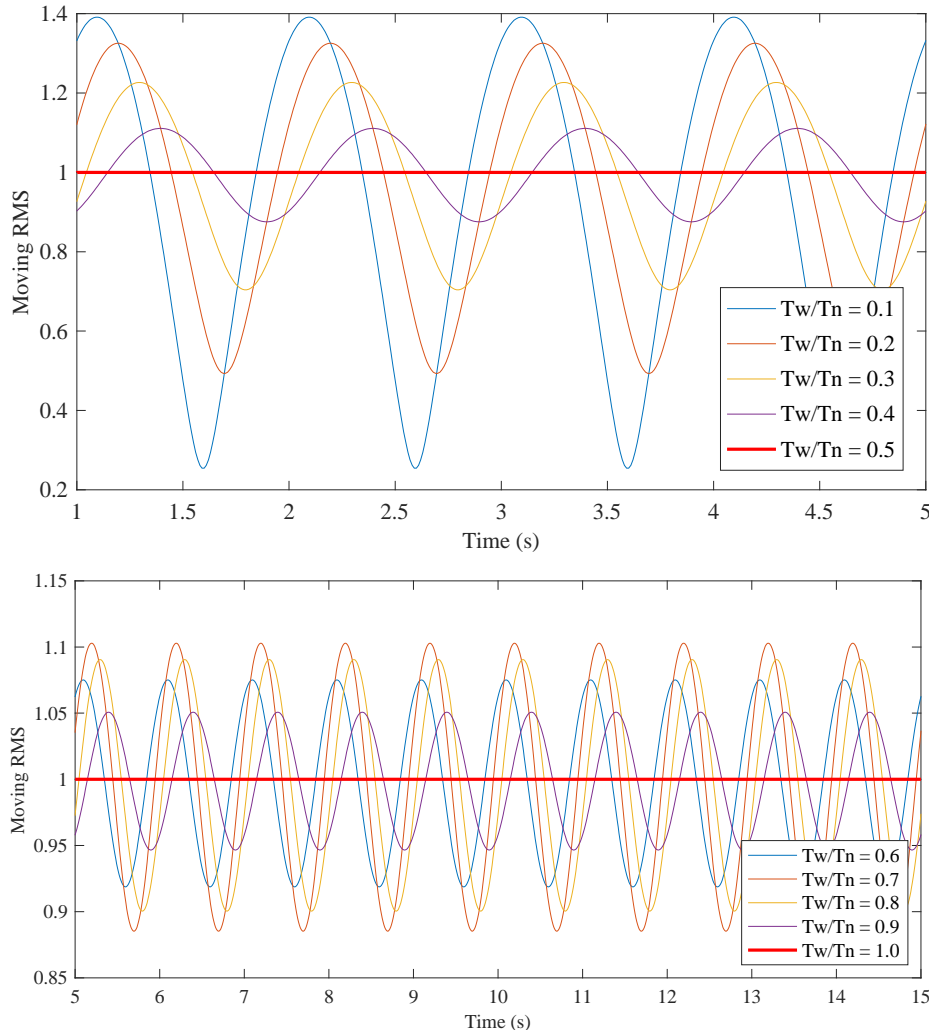


Figure 4-12 Moving RMS according to the segment length

Figure 4-13 demonstrates a variation in the maximum value of a moving RMS for a single sinusoidal function, according to the segment ratio (T_w/T_n). The fluctuating errors in a moving RMS become zero for $T_w/T_n = 0.5n$ ($n \in \mathbb{N}$), regardless of natural frequency of the single sinusoidal function. When the segment ratio exceeds 2, the error in a moving RMA becomes less than 5%.

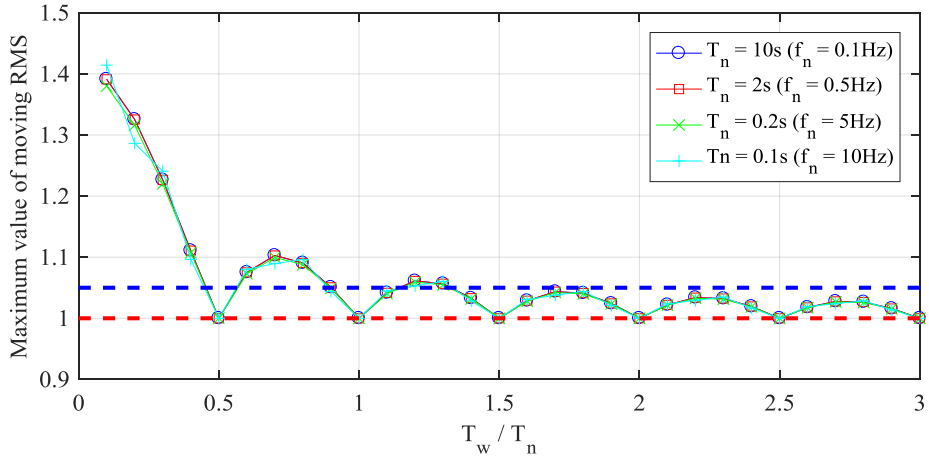


Figure 4-13 Maximum value of moving RMS by the segment ratio (T_w/T_n)

Accordingly, the segment length should be larger than twice the longest period of targeting structural modes in order to secure the fluctuating errors in a moving RMS of less than 5%, as follows.

$$T_w/T_n > 2 \quad (4-7)$$

$$T_w > 2T_n \quad (4-8)$$

where T_w is the required segment length or the filter size, and T_n is the natural period of the lowest mode. In the case of the Jindo Bridge, since the natural frequency of the first vertical mode was 0.436Hz, the required segment length should be larger than 4.59 seconds ($=2/0.436\text{Hz}$) to maintain the fluctuating errors in a moving RMS of less than 5%.

Figure 4-14 shows the calculated AM function from measured acceleration of Jindo Bridge. As can be seen, the fluctuation was reduced by

increasing segment ratio, and the segment length of 2 times of natural period was appropriate to reduce a fluctuating term in AM function.

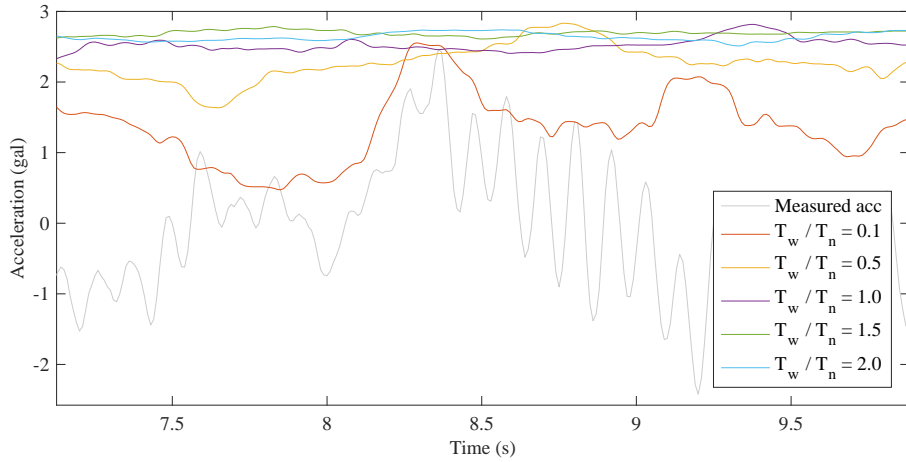


Figure 4-14 Calculated AM function according to segment ratio

4.3.3. Signal stationarization of operational monitoring data

The proposed stationarization process was applied to the operational monitoring data obtained from the Sorok Bridge. The AM function was evaluated by calculating the temporal-root-mean-square function of measured acceleration. Then, the approximated stationary acceleration can be extracted by dividing the measured acceleration by the AM function.

Figure 4-15 show the traffic-induced accelerations before and after signal stationarization, respectively. Before the signal stationarization process, the measured acceleration in time history was localized. The kurtosis value exceeded the criteria of 10. However, after the stationarization process, the

peaks due to traffic loading were removed from the time history. The kurtosis value also decreased from 12.83 to 2.36.

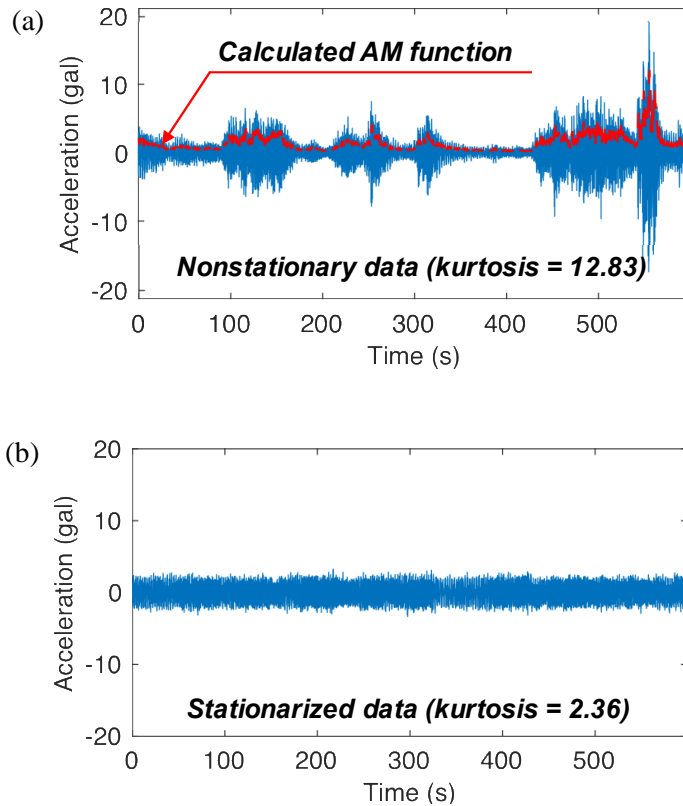


Figure 4-15 Measured acceleration (a) without signal stationarization and (b) with stationarization

Figure 4-16 compares normalized PSDs before and after signal stationarization. The frequency components around vehicle frequencies of 2-5Hz were clearly reduced with an application of the AM function during the signal stationarization. As a result, the PSD of stationarized data showed a frequency component that was similar to the stationary case in Figure 4-5.

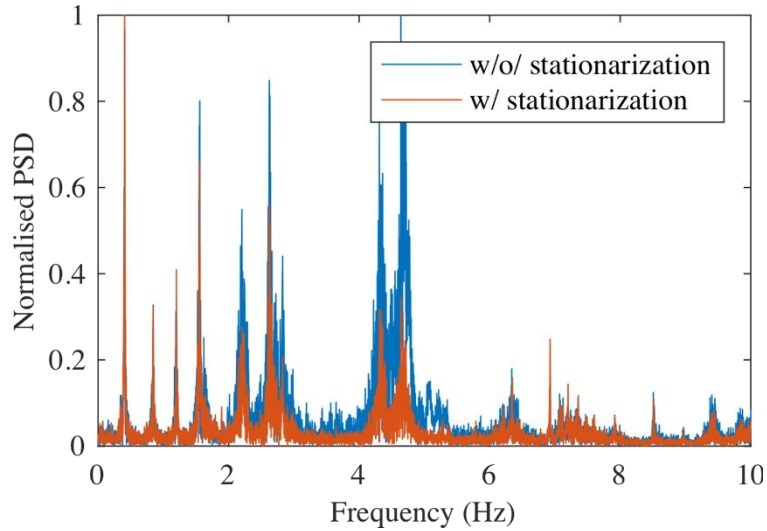


Figure 4-16 PSD of measured acceleration (a) w/o signal stationarization and
(b) with stationarization

4.4. Application to NExT-ERA: numerical simulation

4.4.1. Description of simulated models

To examine the effectiveness of the proposed damping estimation framework for nonstationary response, a numerical simulation of 9-story shear building model was performed. A simplified diagram of considered model is shown in Figure 4-17.

The mass and stiffness were as below. The damping matrix was considered based on proportional (Cauchy) damping model with damping ratio of 1.0%. The corresponding modal properties are defined in Table 4-3.

$$M = \begin{bmatrix} 611.6 & 0 & 0 & 0 & 0 & 0 & 0 & 0 & 0 \\ 0 & 530.1 & 0 & 0 & 0 & 0 & 0 & 0 & 0 \\ 0 & 0 & 530.1 & 0 & 0 & 0 & 0 & 0 & 0 \\ 0 & 0 & 0 & 530.1 & 0 & 0 & 0 & 0 & 0 \\ 0 & 0 & 0 & 0 & 530.1 & 0 & 0 & 0 & 0 \\ 0 & 0 & 0 & 0 & 0 & 530.1 & 0 & 0 & 0 \\ 0 & 0 & 0 & 0 & 0 & 0 & 509.7 & 0 & 0 \\ 0 & 0 & 0 & 0 & 0 & 0 & 0 & 509.7 & 0 \\ 0 & 0 & 0 & 0 & 0 & 0 & 0 & 0 & 509.7 \end{bmatrix} \text{ ton}$$

$$K = \begin{bmatrix} 4.2 & -2.1 & 0 & 0 & 0 & 0 & 0 & 0 & 0 \\ -2.1 & 4.2 & -2.1 & 0 & 0 & 0 & 0 & 0 & 0 \\ 0 & -2.1 & 4.2 & -2.1 & 0 & 0 & 0 & 0 & 0 \\ 0 & 0 & -2.1 & 4.2 & -2.1 & 0 & 0 & 0 & 0 \\ 0 & 0 & 0 & -2.1 & 4.2 & -1.9 & 0 & 0 & 0 \\ 0 & 0 & 0 & 0 & -1.9 & 3.8 & -1.7 & 0 & 0 \\ 0 & 0 & 0 & 0 & 0 & -1.7 & 3.4 & -1.7 & 0 \\ 0 & 0 & 0 & 0 & 0 & 0 & -1.7 & 3.4 & -1.7 \\ 0 & 0 & 0 & 0 & 0 & 0 & 0 & -1.7 & 1.7 \end{bmatrix} 10^5 \frac{kN}{m}$$

$$C = \Phi^{-1T} \text{diag}[m_n \xi \omega_n] \Phi^{-1} \text{ kN} \cdot \text{s/m} \quad (n = 1, 2, \dots, 9)$$

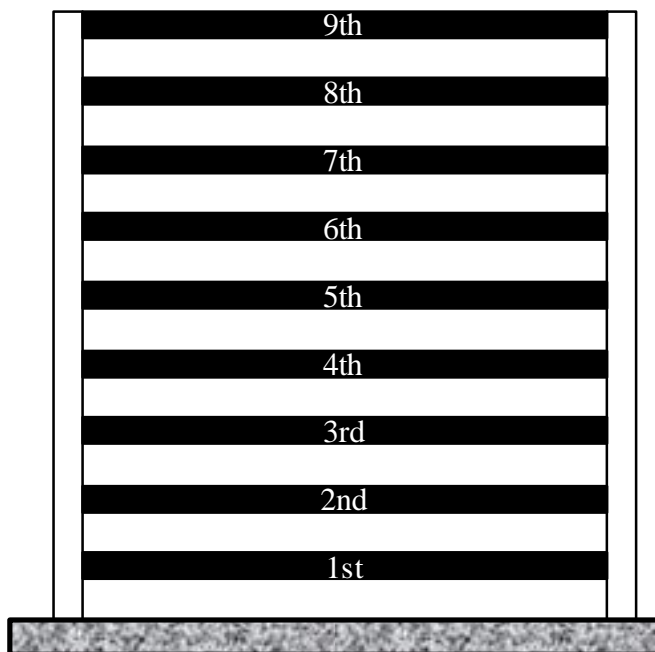
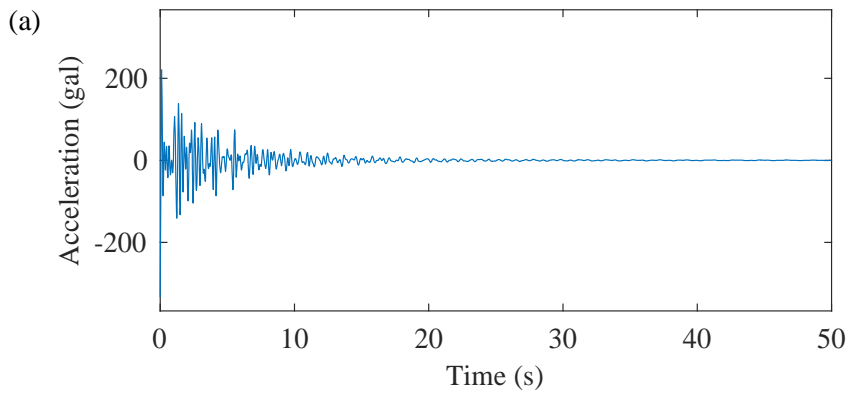


Figure 4-17 Schematic diagram of 9-DOF shear building

Table 4-3 Modal characteristics of 9-story numerical model

Mode order	Frequency (Hz)	Damping ratio (%)
1 st	0.524	1.00
2 nd	1.490	1.00
3 rd	2.433	1.00
4 th	3.325	1.00
5 th	4.062	1.00
6 th	4.781	1.00
7 th	5.310	1.00
8 th	5.741	1.00
9 th	6.171	1.00

To validate the damping ratio of numerical model, an initial displacement in a top floor was imposed for the simulation of free vibration test. The free decayed acceleration at a top floor shown in Figure 4-18, which can be considered as IRF, was applied to ERA to estimated modal properties with system order of 9.



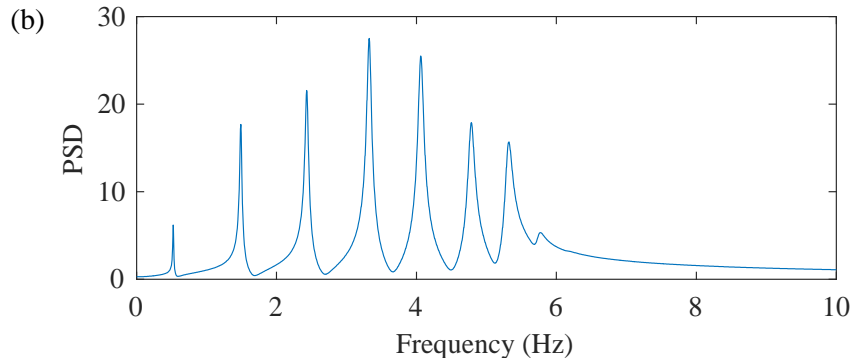


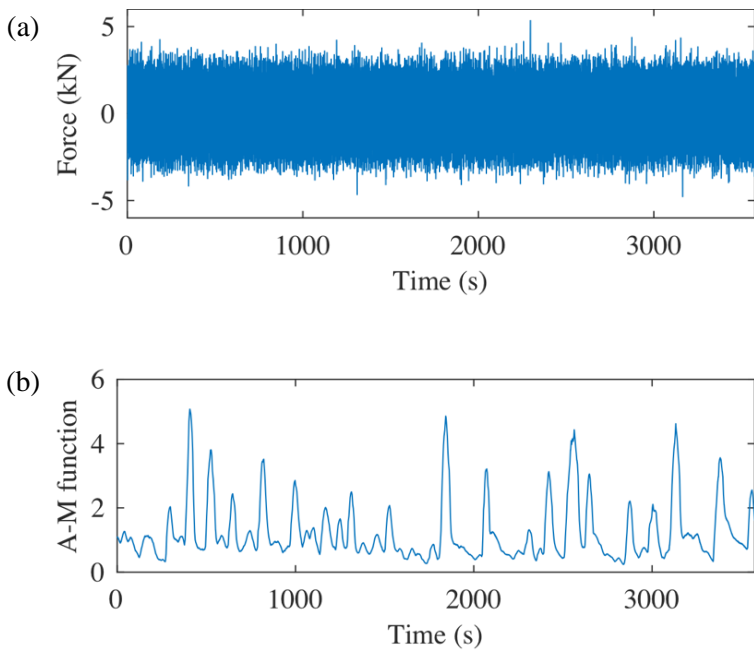
Figure 4-18 (a) free decaying acceleration at the top floor and (b) its PSD

Table 4-4 showed the result of ERA using free decays. As can be seen, the modal frequencies and damping ratios were well agreed with the pre-defined modal properties in Table 4-3. EMAC was 100% for all modes, indicating the perfect mode realization. The higher modal participation factor was found at 5, 4, 6, 2 modes, showing coincidence with the shape of PSD in Figure 4-18(b).

Table 4-4 Result of ERA using free decays

No.	f (Hz)	ξ (%)	EMAC (%)	Participation factor (%)
1 st	0.524	1.000	100.000	3.121
2 nd	1.490	1.000	100.000	9.039
3 rd	2.433	1.000	100.000	12.797
4 th	3.325	1.000	100.000	16.981
5 th	4.062	1.000	100.000	18.134
6 th	4.781	1.000	100.000	16.464
7 th	5.310	1.000	100.000	15.984
8 th	5.741	1.000	100.000	6.074
9 th	6.171	1.000	100.000	1.406

Next, a series nonstationary loading simulations was performed with a total simulation time of 60 min and the sampling frequency of 100Hz. In this simulation, the nonstationary loading was modeled based on Eq. 4-1. At first, a white noise stationary loading was generated using normally distributed random process. Then, the amplitude-modulating function, which was calculated from the field monitoring data as shown in Figure 4-15, was multiplied to stationary loading to obtain a nonstationary loading. The stationary loading, utilized amplitude-modulating function and nonstationary loading are displayed in Figure 4-19, respectively.



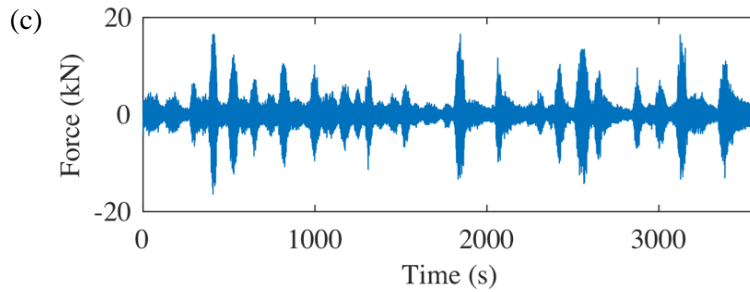


Figure 4-19 Time histories of (a) stationary loading, (b) amplitude-modulating function and (c) nonstationary loading

Using these stationary/nonstationary loading, a total of three accelerations (shown in Figure 4-20) corresponding to loading condition and signal stationarization was considered.

- 1) First case, which is denoted as ‘stationary excitation’, utilized a stationary loading. The acceleration measurements under this stationary loading were considered as the reference response satisfies the basic assumption of classical OMAs.
- 2) Next, in the case of ‘nonstationary excitation’, the nonstationary acceleration was conducted under the nonstationary excitation as shown in Figure 4-19(c).
- 3) Finally, by applying a signal stationarization to nonstationary acceleration, we obtained a stationarized acceleration denoted as ‘stationarized’.

The simulation conditions for each case are summarized in Table 4-5.

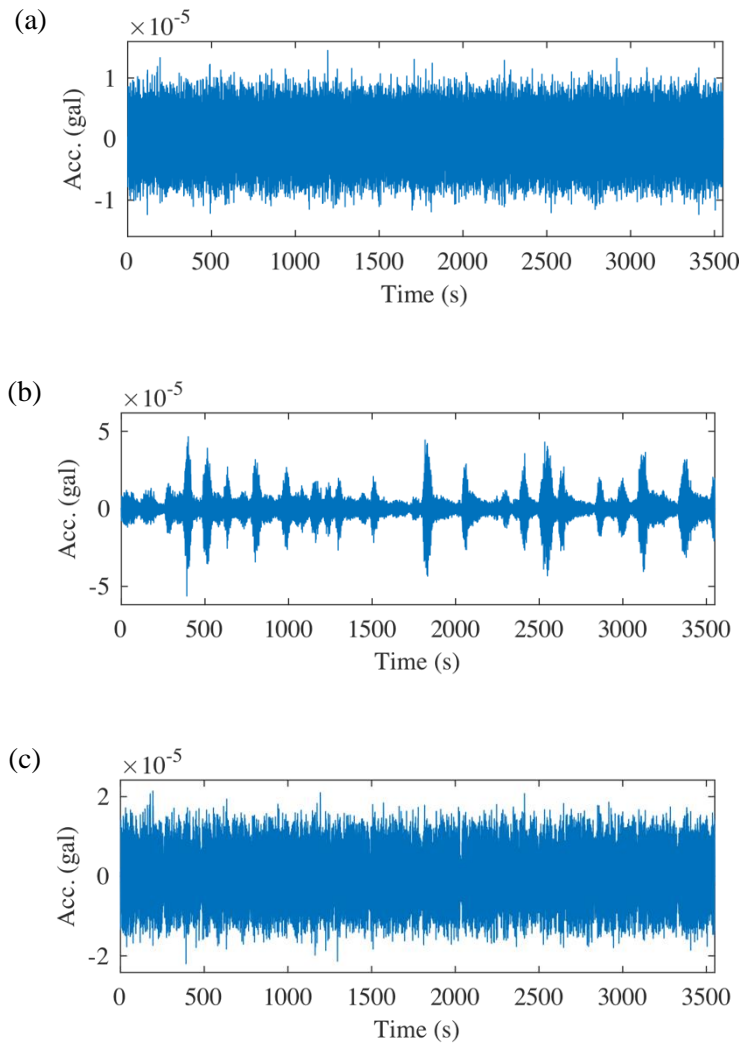


Figure 4-20 Calculated acceleration of 8th story under (a) stationary excitation, (b) nonstationary excitation and (c) stationarized acceleration of (b)

Table 4-5 Case name and corresponding simulation conditions

Case name	Load condition	Signal stationarization
Stationary excitation	Stationary loading	X
Nonstationary excitation	Nonstationary loading	X
Stationarized	Nonstationary loading	O

A total of 100 simulations was performed for each case by 100 reproduction of stationary loading. In all cases, the excitation input was applied to the 8th story mass, and the acceleration of the system was calculated based on state-space model.

4.4.2. Estimated damping ratio corresponding to signal stationarization

Figure 4-21 presents the estimated 3rd modal damping ratio for the 100 simulations from a simulated acceleration shown in Figure 4-20. Dashed lines indicate the mean values of each case.

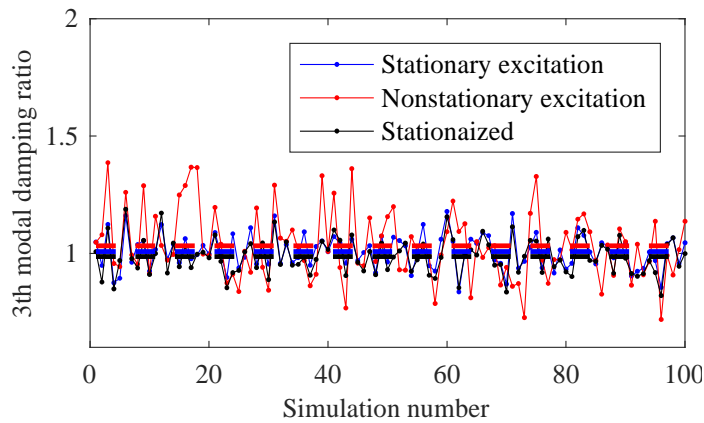


Figure 4-21 Estimated 3rd modal damping ratio for the 100 simulations

Table 4-6 The statistics of estimated 3rd modal damping ratio

	Stationary excitation	Nonstationary excitation	Stationarized
Mean	1.01%	1.03%	0.99%
COV	7.09%	14.32%	7.64%

The mean values of damping ratios for each case were almost the same value of 1.01%, 1.03% and 0.99%, respectively while the estimated damping ratios under nonstationary excitation showed over/underestimated compared to a stationary excitation. Actually, COV of estimated damping ratio under nonstationary excitation was 14.3% while under stationary excitation was 7.1%. After a signal stationarization, over/underestimated damping ratios under nonstationary excitation were recovered to the values under stationary excitation, and it leads to reduce a scattering in terms of COV from 14.3% to 7.6%. Table 4-6 summarizes the statistics of estimated 3rd modal damping ratio provided under each experimental condition.

A peak response contributed to over/underestimation of damping ratio in OMA. A signal stationarization, which is effective to decrease a peak response in measured data, was suitable to decrease this scattering successfully.

4.5. Application to NExT-ERA: operational monitoring data of Jindo Bridge

4.5.1. Combined framework of p.p.s and stationarization

The combined framework with the aforementioned two procedures—parameter selection and stationarization—is proposed shown in Figure 4-22. While each analysis parameter was selected based on the measurement condition and structural information, a signal stationarization should be selectively applied depending on the kurtosis value of the measured acceleration.

As Guo (2015) suggested, a kurtosis value of 10 was utilized as a criterion to differentiate stationary from nonstationary measured data. If the kurtosis value of the measured acceleration was larger than 10, a signal stationarization procedure was applied. After this classification and signal stationarization, NExT-ERA was performed with a proper parameter selection.

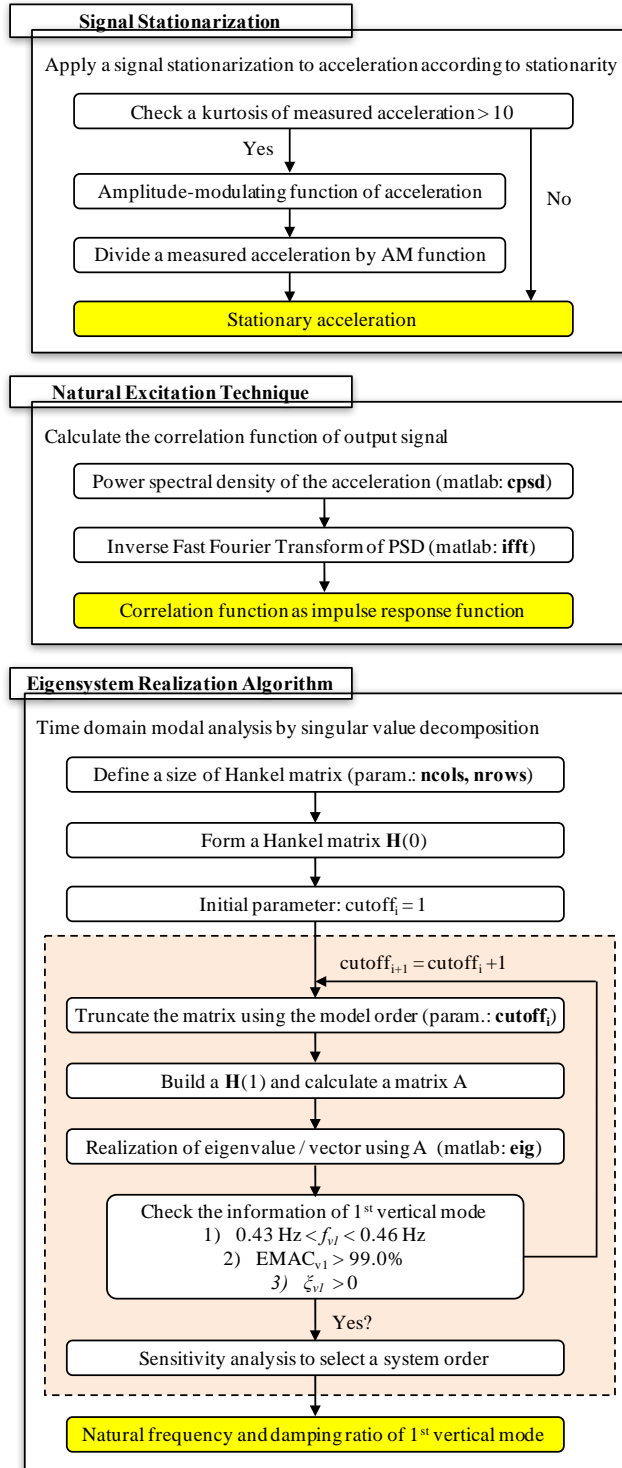


Figure 4-22 Proposed damping estimation framework

4.5.2. Monitoring data

Aforementioned data sets recorded for 3 days starting on October 15 and 4 days on December 14, 2012 were utilized for damping estimation. Based on the parametric study, the measured acceleration of Bridge 2 was divided into 1-hour segments. All of algorithmic parameters were equal to Section 3.4.

4.5.3. Effect of signal stationarization in Jindo Bridge

Figure 4-23 shows the example of signal stationarization in Jindo Bridge. The measured acceleration at the center of the mid span and corresponding amplitude-modulating function are shown in Figure 4-23(a). The kurtosis of measured acceleration without stationarization was 32.59 indicating a nonstationary process. After stationarization, the peaks due to vehicle loading in time histories was significantly removed shown in Figure 4-23(b). A kurtosis also decreased to 2.67 which was lower than criterion of nonstationary classification of 10.

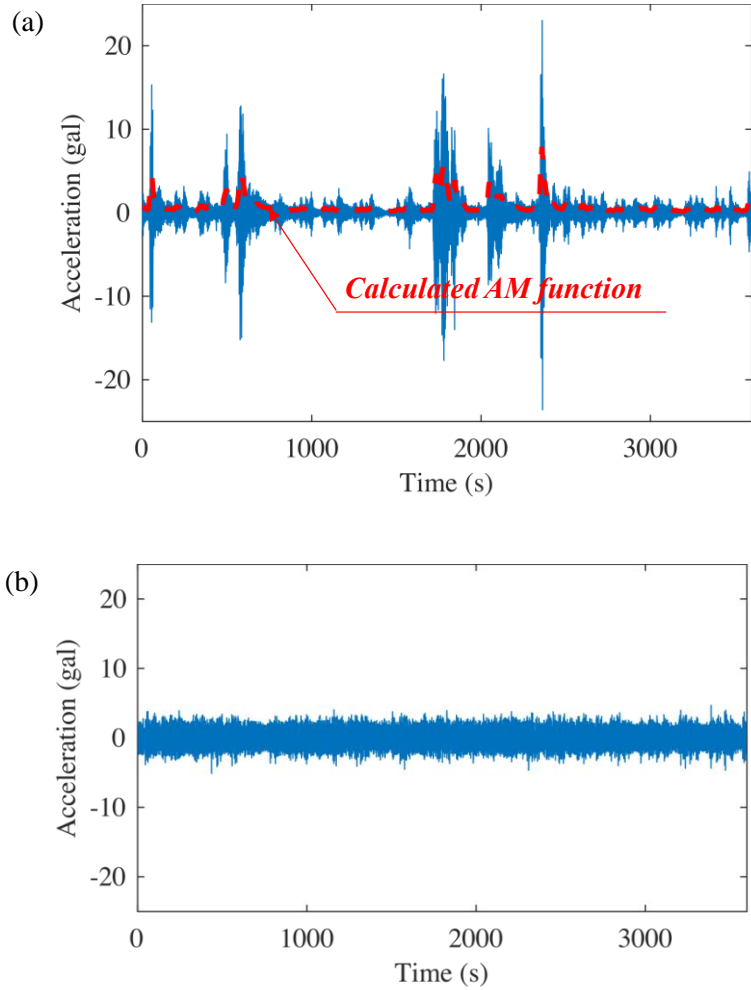


Figure 4-23 (a) Measured acceleration at Oct. 16, 22:00 and corresponding calculated amplitude-modulating function (b) stationarized acceleration of (a)

Figure 4-24 illustrates the normalized PSD of measured acceleration at Oct. 16, 22:00 (Figure 4-23). Regardless of stationarization, a first vertical mode was dominant in the both PSD. The structural modes within vehicle frequency range were amplified due to the passing vehicle, and it reduced according to applying stationarization process.

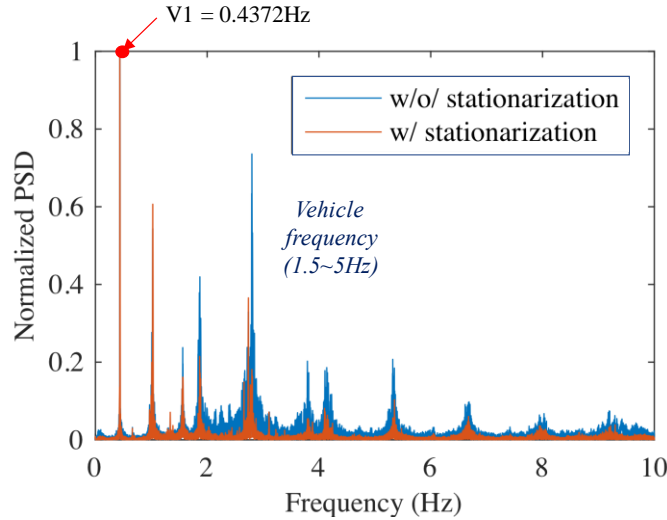


Figure 4-24 PSD of measured acceleration (Oct. 16, 22:00) according to
signal stationarization process

The effect of signal stationarization for overall operational monitoring data is shown in Figure 4-25. It shows that a distribution of kurtoses during 3 days according to a signal stationarization process. The kurtoses without stationarization were ranged from 3.45 to 126.17 with a mean value of 22.70. Based on the criterion of nonstationary classification, a total of 30 cases of measured accelerations were identified as a nonstationary response in 57 data sets. After stationarization, these kurtoses reduced as a level of 1.99 to 2.89 with mean value of 2.63.

A signal stationarization was effective to reduce the nonstationarity due to the vehicle loads in the Jindo Bridge. The distortion in the PSD also reduced according to the signal stationarization.

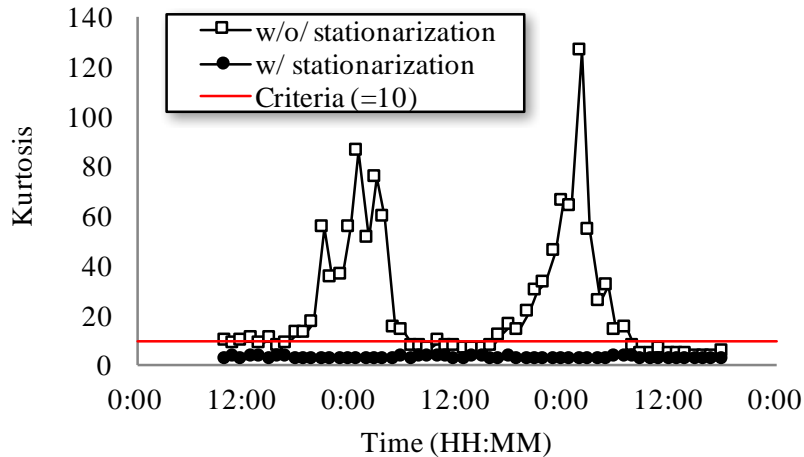


Figure 4-25 Kurtosis according to stationarization

4.5.4. Estimated damping ratio according to signal stationarization

Three comparative approaches were implemented in estimating the damping ratio of the first mode of Bridge 2. The first case did not consider the parameter selection and the stationarization and simply applied NExT-ERA to the measured data which was the result of Section 0, and hereafter this is referred to as ‘basic’. The secondary procedure is ‘Proper Parameter Selection (P.P.S)’, the result of Section 3.4. An identified damping ratio with signal stationarization is referred to as ‘P.P.S + Stationarization’ or ‘w/ stationarization’.

Figure 4-26 shows the estimated damping ratio of Bridge 2 during operation. The statistical values for the identified damping ratio are listed in Table 4-7 corresponding to each procedure. The mean value of damping ratio

of the first vertical mode was almost same among three procedures. On the other hands, a proper parameter selection and signal stationarization was effective to reduce a scattering. The COV of the estimated damping ratios of two methods was from 29.7% to 43.3%, which represents an acceptable result compared to previous AVT practices (Benedettini and Gentile, 2011; Brownjohn et al., 2010; Magalhães et al., 2012; Magalhães et al., 2010; Reynders et al., 2012).

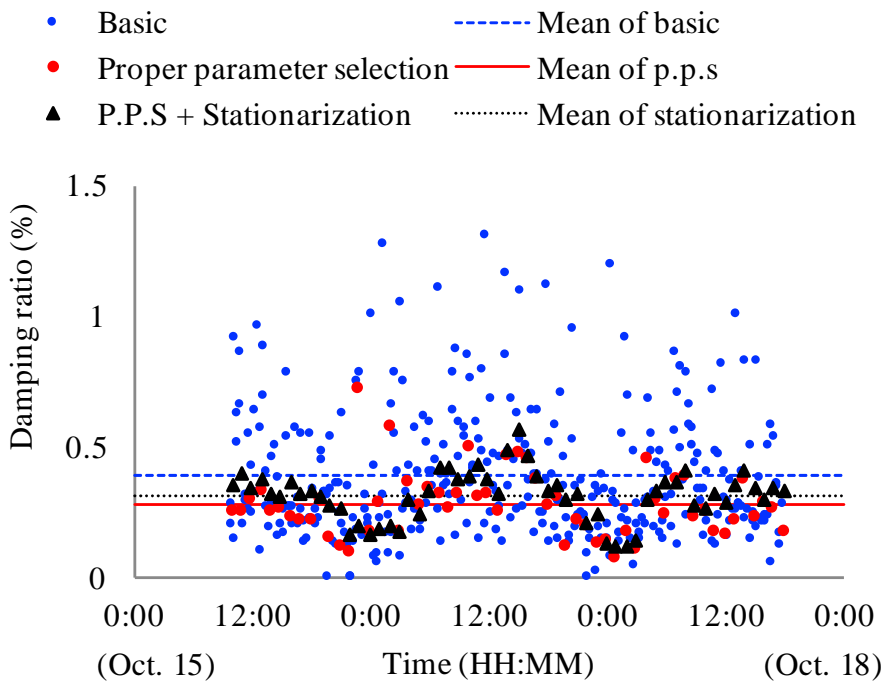


Figure 4-26 Estimated modal damping ratio of Jindo Bridge according to proper parameter selection and signal stationarization

Table 4-7 The statistics of estimated modal damping ratio of Jindo Bridge

	Basic	P.P.S	P.P.S + Stationarization
Mean	0.37%	0.28%	0.32%
COV	95.07%	43.29%	29.73%

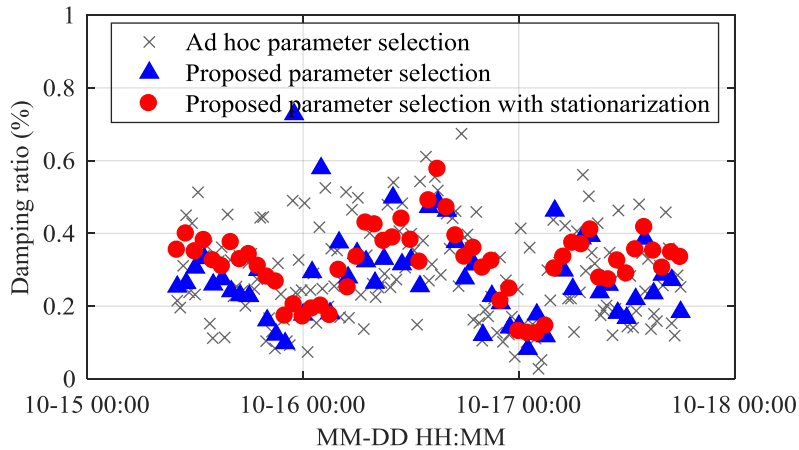


Figure 4-27 Estimated damping ratio for 3-day data (x: Ad hoc parameter selection for each 20-min segmented acceleration data (Kim et al., 2013), \blacktriangle : Proposed parameter selection for each 60-min segmented acceleration data, \bullet : Proposed parameter selection for each stationarized 60-min segmented acceleration data)

In the results shown in Figure 4-27, the cross marks indicate the identified damping ratios via the ad hoc approach, which was variation3 wherein the analysis parameters were determined via trial-and-error parametric study shown in Figure 2-10, while the triangle mark denotes the identified damping ratios according to the proposed parameter selection. The enhancement in terms of decreased variation in identified damping ratios is

due to the help of a longer period of data collection (60 min) as well as to a more reasonable selection of algorithm parameters for NEXT and ERA procedures. The circular mark denotes the identified damping ratios by applying the AM-based stationarization process to the measured acceleration data followed by NEXT-ERA procedures using the same proposed parameter selection process. The identified damping ratios slightly increased for most of the segmented data by comparison with those without stationarization. The stationarization process also decreased the variation in the identified damping ratios, which demonstrates the effectiveness of the proposed approach in OMA-based damping estimation.

Figure 4-28 shows one more procedure denoted as ‘combined’, implies that a signal stationarization was selectively applied depending on the kurtosis value of the measured acceleration which introduced in Section 4.5.1. Table 4-8 summarizes the statistics of estimated damping ratios corresponding to each procedure. Applying the combined method, COV also reduced as a level of 31.84% from P.P.S of 43.29% while mean value was almost same with the case of P.P.S. This COV of combined case was slightly larger than the COV of stationarization case. In the consideration of the result of free vibration test of 0.33%, the case of stationarization gave most accurate identification in terms of bias and variance error.

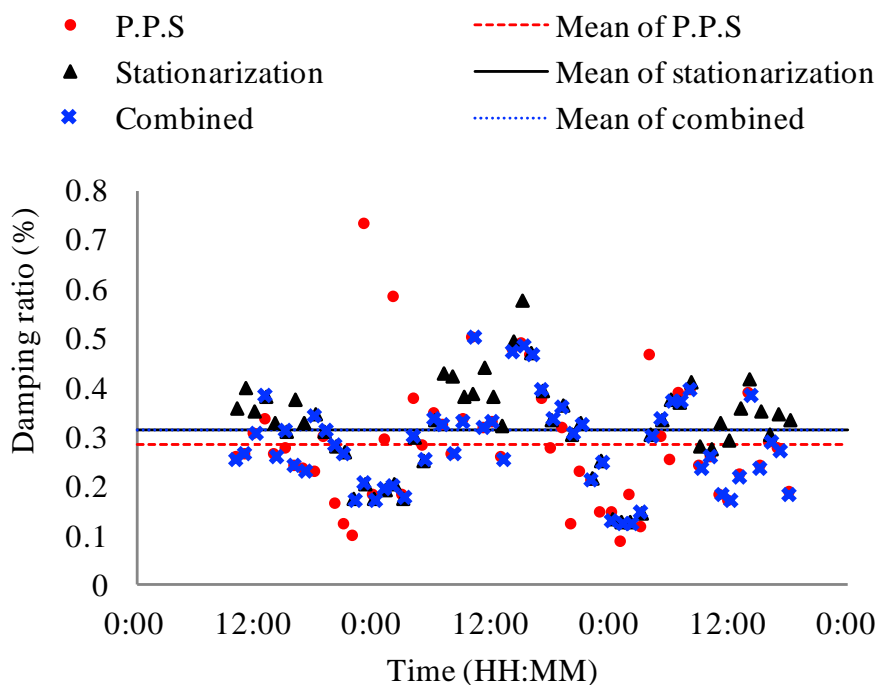


Figure 4-28 Estimated modal damping ratio of Jindo Bridge by applying
combined method

Table 4-8 The statistics of estimated modal damping ratio of Jindo Bridge
after proper parameter selection

	P.P.S	Stationarization	Combined
Mean	0.28%	0.32%	0.28%
COV	43.29%	29.73%	31.84%

Figure 4-29 illustrates the effect of segment ratio of moving RMS on the accuracy of damping estimation. As can be seen in Figure 4-29(a), the accuracy of damping estimation in terms of bias and random error was

significantly enhanced according to increasing segment ratio as shown in Figure 4-29(b). Actually, as expected in the discussion of optimal segment length, the mean and standard deviation were stabilized after the segment ratio of 1.0~2.0.

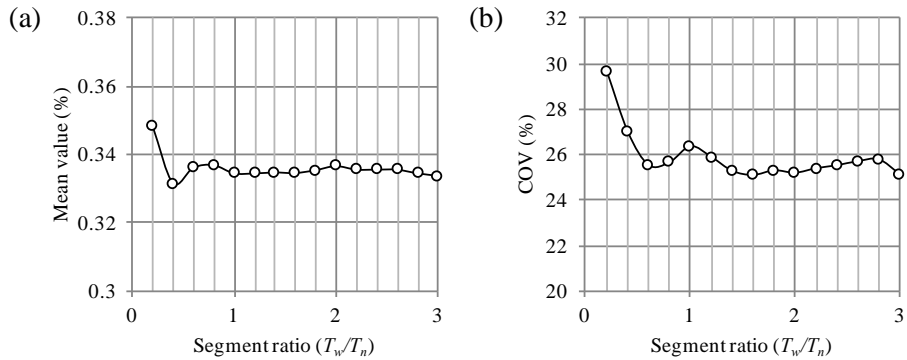


Figure 4-29 The statistics of estimated damping ratio according to the segment ratio of moving RMS: (a) mean value and (b) COV

4.6. Application to NExT-ERA: Jindo Bridge after installation of MTMD

4.6.1. Monitored data

The built-in sensors that are used to monitor the dynamic response of the bridge are shown in Figure 2-1. The vertical acceleration of the deck of Bridge 2 was measured by two accelerometers with a sampling frequency of 100 Hz. An ultrasonic anemometer installed on the northwest side of Bridge 2

was utilized to simultaneously measure the wind velocity at the leading edge of the deck. The anemometer was located at a height of 3 m over the deck and the sampling frequency was set to 1Hz.

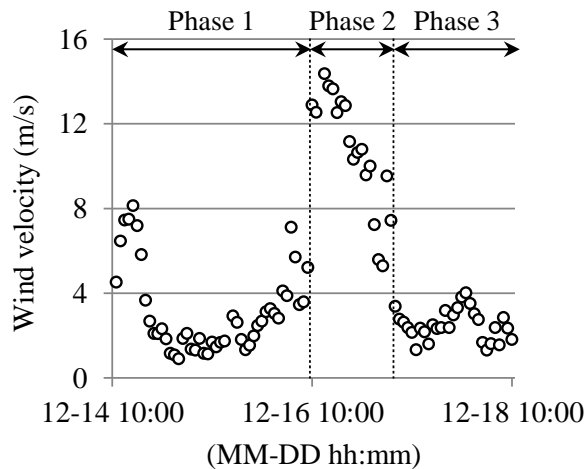


Figure 4-30 1-hour mean wind velocity for 4-day wind data

The acceleration data, recorded for 4 days starting on December 14, 2012, were utilized for an output-only modal analysis. For the operational modal analysis of Bridge 2, the 4-day measured acceleration and wind velocity was divided into 1-hour segments. The 1 hour-averaged mean wind velocities are shown in Figure 4-30. The monitored data were separated into three time phases according to the level of mean wind velocity. The division is based on the onset velocity of the VIV, which was approximately 10m/s. During Phase 1 (12-14 11:00 to 12-16 10:00) and Phase 3 (12-17 01:00 to 12-18 10:00) the mean wind velocity was less than 10 m/s. For Phase 2 (12-16 10:00 to 12-17

01:00), the mean wind velocity exceeded 10 m/s, as shown in Figure 4-30.

4.6.2. Estimated damping ratio corresponding to signal stationarization

A total of two analysis condition—basic and stationarization with proper parameter selection—was compared in this chapter. Figure 4-31 shows the distribution of estimated damping ratios during the operation of the MTMD with basic analysis condition.

The damping ratio of the first vertical mode was significantly enhanced from the initial value of 0.3% for the bare structure with the strong variation in a distribution. Note that this variation in the estimated value of the damping ratio showed a similar trend with that of the mean wind velocity, as shown in Figure 4-30.

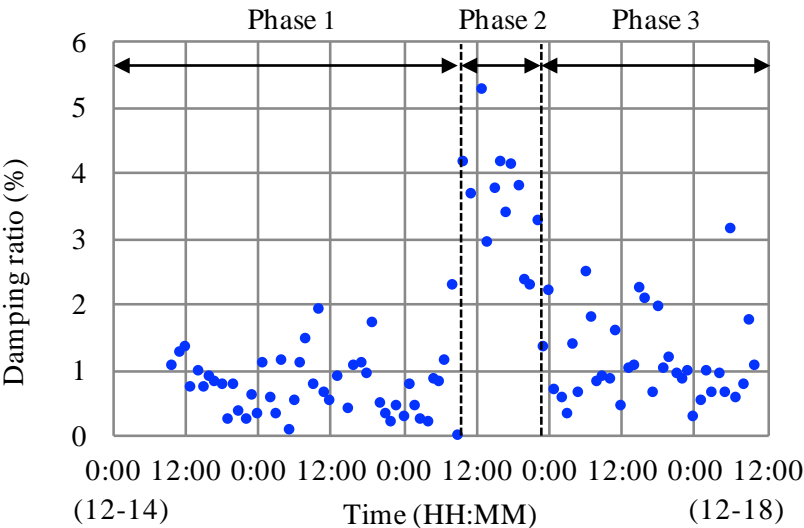


Figure 4-31 Estimated damping ratio during the operating MTMD with basic analysis condition

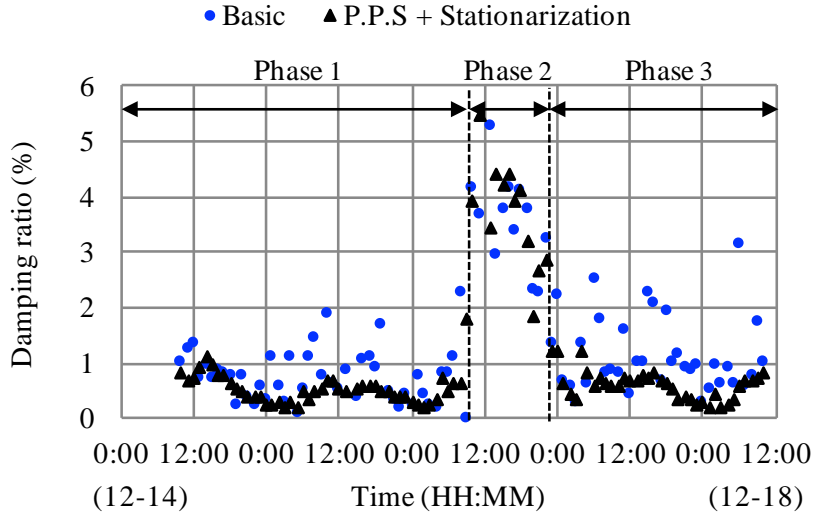


Figure 4-32 Comparison of estimated damping ratio during the operating MTMD between the cases of basic and signal stationarization condition

This tendency appeared much clearly after signal stationarization. Figure 4-32 compares the distribution of estimated damping ratios between the analysis conditions of basic condition and of stationarization condition. As can be seen, the overestimated damping ratios in Phase 1 and Phase 3 were successfully stabilized. Consequently, the full operation of MTMD in Phase 2 was highlighted well. Actually, a significant difference in the identified damping ratios was found for different mean wind velocities after stationarization. For Phases 1 and 3, the mean of damping ratio was 0.52~0.61% with a range of 0.18~1.80%. This was, in fact, an increased value compared to that of bare structure but much less than the designed damping ratio of 3~4%. In contrast, the mean of damping ratio for Phase 2 reached an average of 3.72%

for fully controlled conditions. This indicated that the installed MTMD was in a full operation in the case of the onset wind velocity for the VIV.

Table 4-9 The statistics of estimated modal damping ratio of Jindo Bridge
with operating MTMD

	Basic		Stationarization	
	Mean	COV	Mean	COV
Phase 1	0.79%	59.79%	0.52%	41.24%
Phase 2	3.61%	23.02%	3.72%	25.64%
Phase 3	1.15%	57.88%	0.61%	43.37%

The statistical values for the identified damping ratio corresponding to phase and analysis conditions are listed in Table 4-9 for each phase. As presented in the previous chapters, a similar trend was observed in Phase and Phase 3. A scattering in estimated damping ratio decreased by applying a signal stationarization process in terms of decreasing COVs from 57.88~59.79% to 41.24~43.37%.

The interesting point was that COV of estimated damping ratios in basic case was lower than that of stationarization case in Phase 2. It indicates that even the estimation of basic case was more reliable compared to the stationarization case. This reliable damping estimation in basic case might be due to the greater modal participation of the target mode caused by a higher wind velocity.

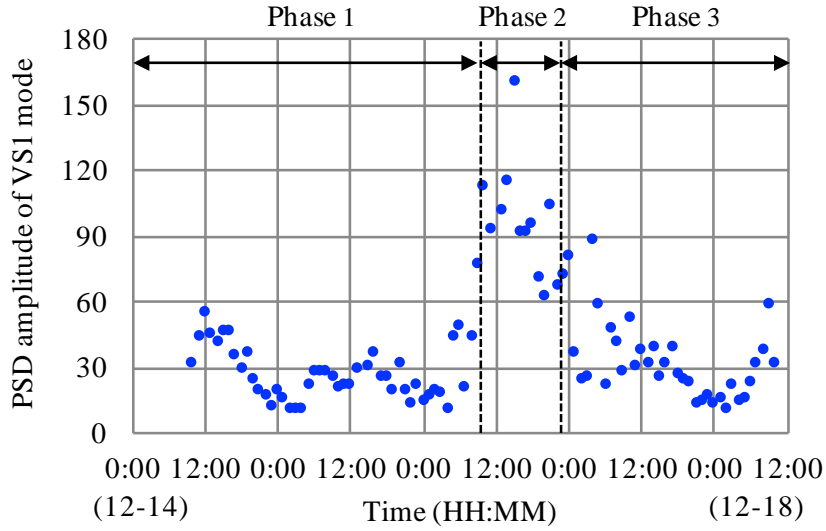


Figure 4-33 PSD amplitude of first vertical mode

Figure 4-33 shows the PSD amplitude of first vertical mode during 4-days. As can be seen, the first vertical mode was the most dominant modes in Phase 2, contrary to Phase 1 and Phase 3 since the wind velocity of 10~15 m/s was the onset velocity of vortex-induced vibration of Bridge 2. In addition, ERA is based in the energy method. It means that the more dominant modes correspond to the larger PSD amplitude are more easily identified. Therefore, even without the procedure of selecting a median value, the target mode was identified well with only a minimum system order in Phase 2.

4.6.3. Effectiveness of MTMD according to windy condition

To identify the conditions for the activation of the MTMD, the accelerations of each TMD were recorded simultaneously using the existing operational monitoring system during June 2013. The overall data, including the acceleration of the bridge deck, the TMDs and wind velocity were divided into 1-min intervals for an in-depth investigation.

Figure 4-34 shows the wind velocity-acceleration (V-A) curve for the MTMD. The acceleration of the MTMD was calculated by averaging the vertical acceleration of four TMDs. As can be seen, the MTMD was fully operated when the mean wind velocity reached the onset velocity of the VIV.

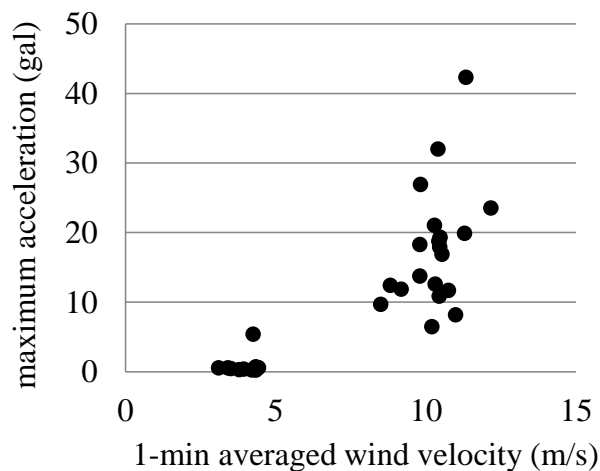
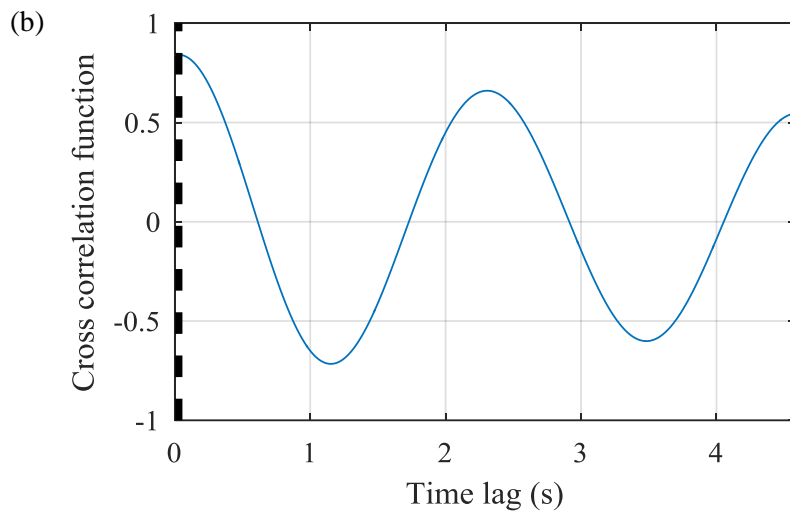
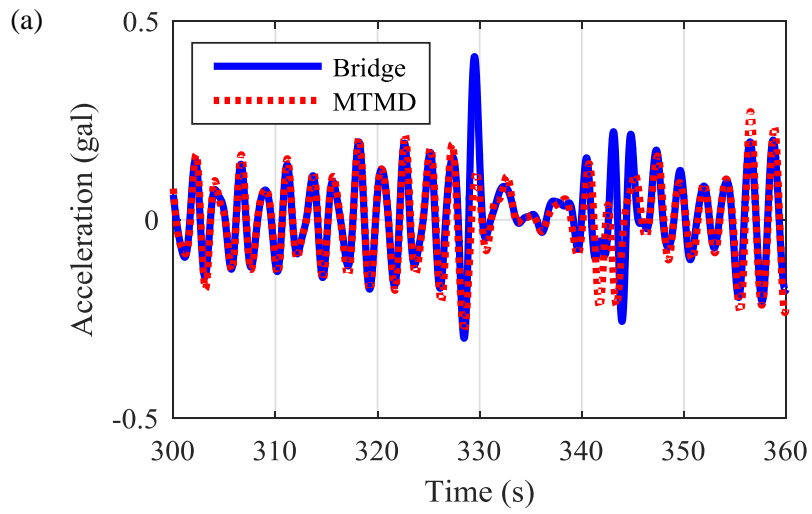


Figure 4-34 V-A curve of the averaged vertical vibration of TMDs

For more details, the amplitudes and phase lags of the MTMD under conditions of different wind velocities are shown in Figure 4-35 and Figure 4-36. For a low wind velocity of less than 4 m/s, the bridge and the MTMD were in phase, as shown in Figure 4-35. The measured acceleration of the MTMD was the same as that of the bridge, indicating that the MTMD vibrates with the bridge as a unit.

For the onset wind velocity case ($U > 10$ m/s) in Figure 4-36, however, the phase angles of the TMDs with respect to the bridge were about 90 degrees, which maximize the damping effect produced by energy dissipation. The measured acceleration of the MTMD was also high for suppressing the higher motion of the bridge deck.

Figure 4-35 and Figure 4-36 also show the PSDs for the acceleration of the bridge as well as TMDs. For low wind velocity, the amplitudes of PSDs for TMDs were similar to those for the bridge illustrating one motion between TMDs and the bridge. However, for the onset wind velocity, the amplitudes of the PSDs for TMDs exceeded those for the bridge to a considerably extent, due to the energy-dissipating motion of the TMDs.



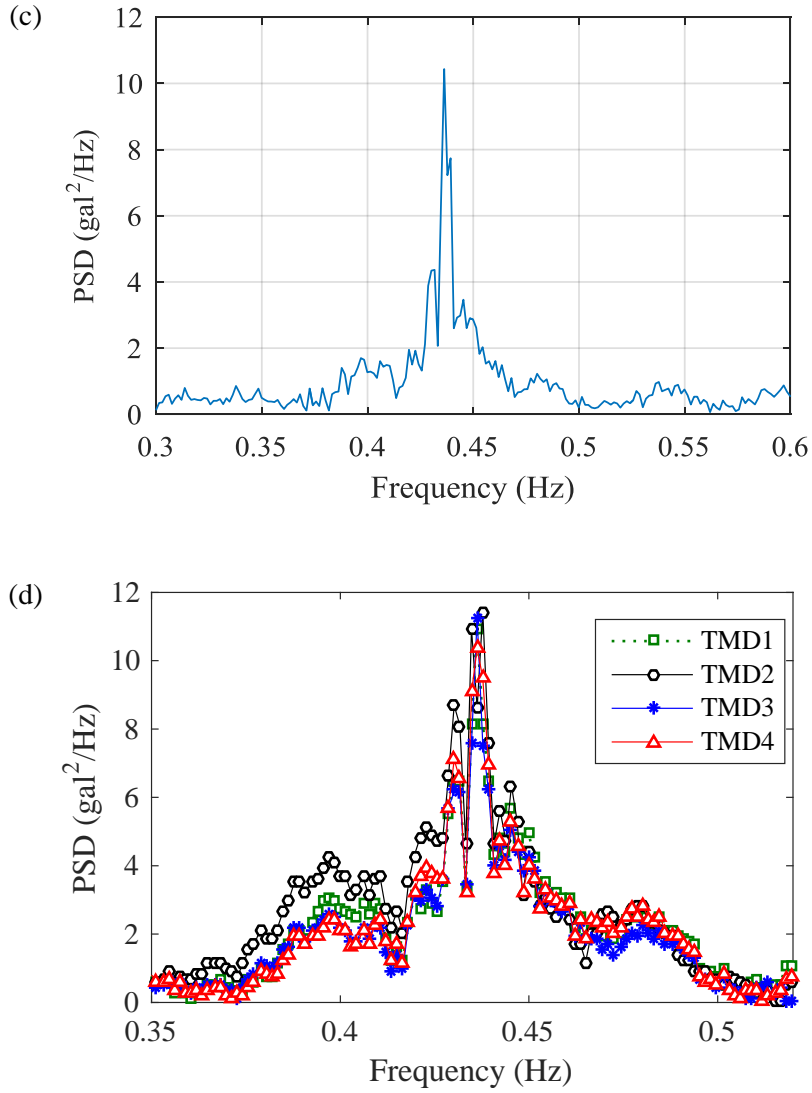
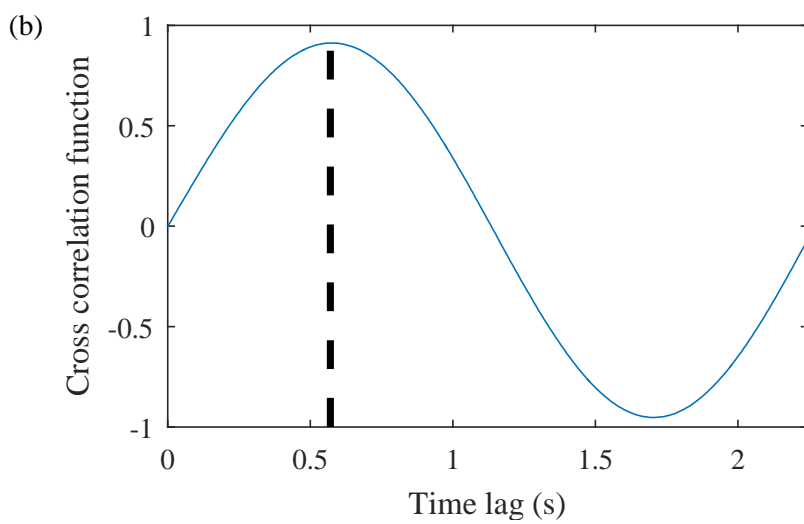
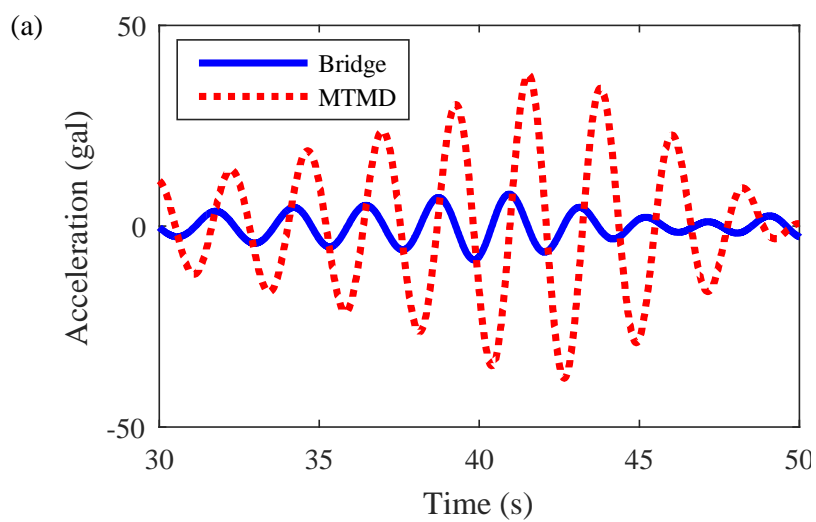


Figure 4-35 (a) Measured acceleration, (b) cross correlation function between Bridge 2 and MTMD (time lag is 0.03 second corresponding to phase lag of 4.71°), (c) PSD of bridge and (d) PSD of MTMD for low wind velocity



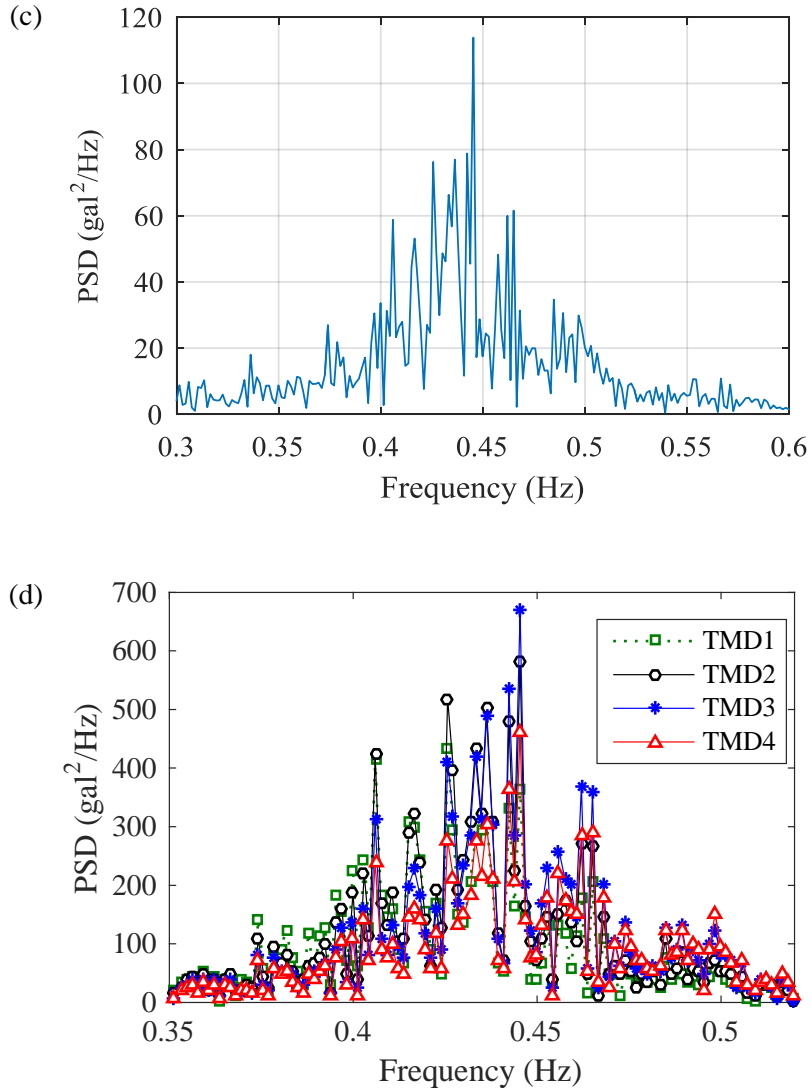


Figure 4-36 (a) Measured acceleration, (b) cross correlation function between Bridge 2 and MTMD (time lag is 0.57 second corresponding to phase lag of 91.4°), (c) PSD of bridge and (d) PSD of MTMD for onset wind velocity

The enhancement in damping capacity of the bridge results in an enhanced serviceability for a VIV. Figure 4-37 shows the relationship between the 10-min average wind velocity and the root mean square (RMS) deck acceleration measured at the center of the mid span. ‘Without MTMD’ refers to acceleration data collected for 3 days under uncontrolled conditions prior to the installation of the MTMD during the period 2012/10/15 10:00 to 2012/10/17 24:00, while ‘With TMD’ refers to 4-day data under controlled conditions using the MTMD. Significant VIVs were observed for a wind velocity of 10~12 m/s without MTMD, but with the MTMD, the amplitude of the vertical motion reduced to the level observed for typical ambient vibration condition.

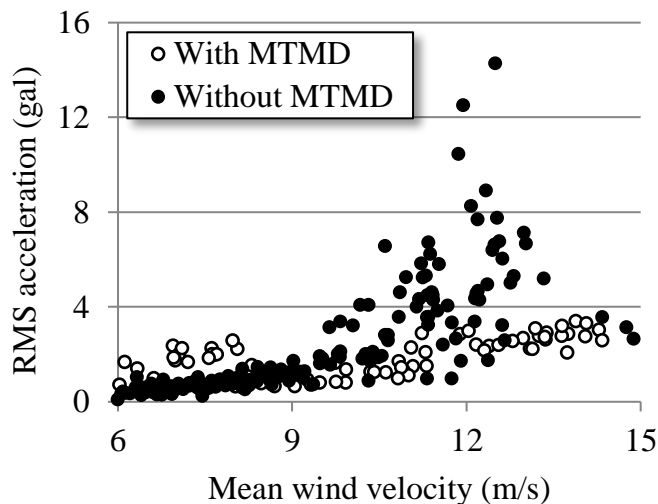


Figure 4-37 V-A curve of the deck of Bridge 2 with and without the MTMD

A pair of PSDs for uncontrolled and controlled conditions shown in Figure 4-38 highlights the efficiency of the MTMD. The PSD amplitude of the first vertical mode decreases to a level of one-third that with the MTMD whereas that of the second vertical mode remains nearly the same.

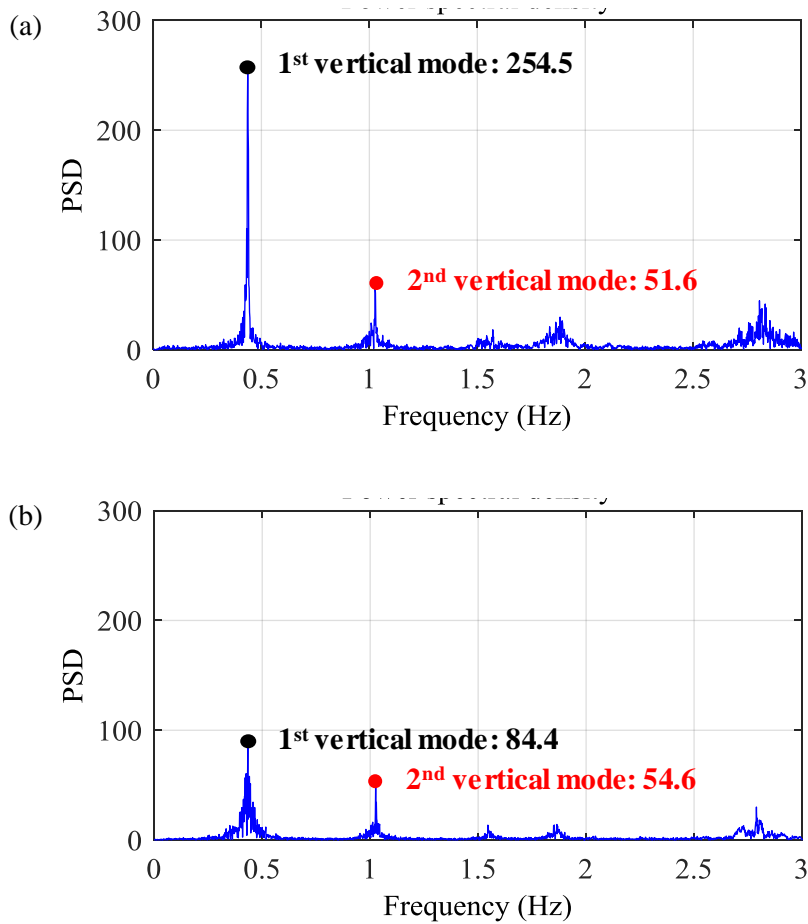


Figure 4-38 PSD of the measured acceleration (a) without MTMD ($U = 10.61\text{m/s}$) and (b) with MTMD ($U = 10.04\text{m/s}$)

4.7. Concluding remarks

A literature survey and field monitoring data confirmed that the traffic-induced vibration was localized, which resulted in a nonstationary response. The structural modes of vehicle frequencies that ranged from 2-5Hz were amplified by traffic loading, but lower structural modes were dominated by stationary excitation. The signal stationarization process that adopted an amplitude modulating function was proposed. The amplitude modulating function was obtained from envelope-type output-only data induced by running vehicles, and was applied to modulate nonstationary components. Values for the nonstationary effect and frequency distortion due to vehicles were successfully reduced by a signal stationarization procedure. After signal stationarization, the kurtosis value was significantly decreased and the power spectral density function approximated that of the stationary data. Consequently, the over/underestimated damping ratio due to TIV was recovered, and the uncertainty of estimated damping ratios was also reduced by applying the signal stationarization process.

Chapter 5

Environmental effect on the variation of estimated damping ratio

Some parts of this chapter were reported in following journal publications:

Kim S, Kim H-K, Hwang YC. Enhanced Damping Estimation for Cable-Stayed Bridges from Operational Monitoring Data. Structural Engineering International. 2018. (submitted)

A previous chapter clearly showed the reduced uncertainty in OMA-based damping estimation by proper parameter selection with signal stationarization process. Nevertheless, the variation of damping ratio was still found with the large range of 0.1% to 0.6%. The reason for these variations should be identified clearly.

Interestingly, the change in estimated damping ratio is regular according to time evolution. The damping ratio started to increase in the morning and maintained a constant value until the evening. After that, it decreased and showed a relatively low value until dawn. This tendency was repeated for 3-days as can be seen in Figure 4-28.

This chapter focused on assessing the effect of environmental factors on the variation of damping ratio, and identifying the most dominant parameter. First, the factors affecting the damping ratio change were selected based on the damping ratio distribution, and the characteristics of each parameter were analyzed. Next, the statistical relationship between the damping ratio and each environmental parameter was evaluated through correlation analysis. Based on these result, the effect of environmental factors on the damping ratio was analyzed.

5.1. Main environmental factors for variation of damping ratio

5.1.1. Vibration amplitude

The damping ratio of bridge was known to be sensitive to the vibration amplitude. Siringoringo and Fujino (2008) observed that the modal damping ratios increased with the increasing RMS of the transverse and vertical acceleration of bridge deck based on the system identification applied to Yokohama Bay Bridge, Rainbow Bridge, and Tsurumi Fairway Bridge using the records from the 2004 Chuetsu-Niigata earthquake. They supposed that the greater energy dissipation from the friction force at hinges and bearings that occurred during large excitation might lead to increase a damping ratio. Chen et al. (2016) found that the modal damping ratios increased according to increasing vibration amplitudes, and stabilized where testing continued into large response amplitude range by the sweep excitation tests using eccentric mass shaker in a multi-span pre-stressed concrete bridge. Since all frictional mechanisms were already activated, no further increase occurred after a certain level of damping was reached.

These stabilizations in amplitude-dependence of damping ratio were clearly shown in a high-rise building. Jeary (1986) suggested the damping predictors as below.

$$\xi_1 = 0.01f_1 + 10\sqrt{D/2}(x_h/H) \quad (5-1)$$

where

- f_1 = lowest natural frequency of building (Hz)
- D = width of building base in vibration direction (m)
- x_h = tip draft (m)
- H = height of building (m)
- x_h/H = Critical tip drift ratio

Equation 4-1 clearly shows that the damping ratio of building had a general tendency to increase with larger vibration amplitude. The estimated damping ratio by Random Decrement Technique (RDT) in a building (Tamura et al., 2000) also presented that the damping due to friction force increased with increasing the number of slipping contacts. Li et al. (2002) also clearly demonstrated the similar nonlinearity in estimated damping ratio by RDT in 79-story tall building. Fukuwa et al. (1996) observed that a damping ratio even decreased in very high amplitudes of tip acceleration in a three-story steel-framed experimental house with autoclaved lightweight concrete (ALC) panel slabs. After it reached a ‘critical tip ratio’, there were no additional slipping contacts, thus reducing the stiffness, so damping ratio can decrease.

Based on the previous researches, it should be noted that large vibration

amplitude induced greater energy dissipation due to the more frictions at the structural components. This physical phenomenon allows increasing a mechanical damping ratio with increased vibration amplitudes. Keeping these typical characteristics of a damping ratio in mind, the amplitude dependency of the damping ratios in the Jindo Bridge was demonstrated with the OMA-based damping estimations and corresponding RMS amplitude of acceleration.

5.1.2. Number of vehicle

As previously mentioned, the main source of ambient vibration in cable-stayed bridge is the traffic loading. Therefore, the influence of the number of vehicles should also be assessed in order to find the factors of the damping ratio variation.

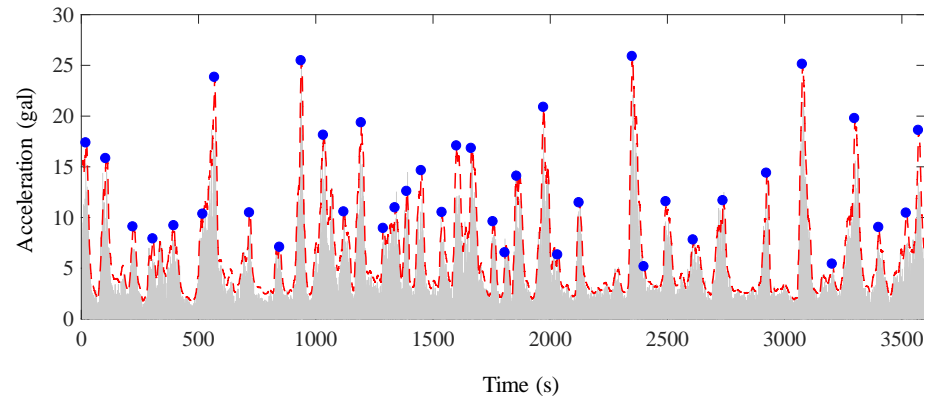


Figure 5-1 Local maxima from the measured acceleration of Jindo Bridge

Unfortunately, there is no sensor on the Jindo Grand Bridge to measure the traffic volume. Therefore, instead of the number of traffic, the number of peaks in the measured acceleration was counted inevitably. First, the envelope of the measurement acceleration is obtained by moving RMS. Then the number of peaks is counted through finding local maxima with the minimum amplitude of the peak of 5 gal and the minimum width of the peak of 50 seconds. Figure 5-1 showed the number of local maxima was successfully counted from the measurement acceleration of Jindo Bridge.

5.1.3. Temperature

Temperature changes are known to be cause variations in modal properties. Many of researchers in damage detection have conducted in-depth studies in this relationship since it may cover the changes of natural frequency due to structural damage. Various researches shown that natural frequencies were sensitive to temperature variations (Hua et al., 2007; Magalhães et al., 2012; Sohn et al., 1999). On the other hand, the influence of temperature on the damping ratio changes is not identified clearly. Xia et al. (2006) performed nearly two-year vibration monitoring of an RC slab to quantify the environmental effect in vibration-based structural health monitoring. The first four modal frequencies showed significant negative relationship with

temperature due to elastic modulus, not a geometry change or friction mechanism. On the other hand, no clear relationship was found in damping ratio since the variation in damping is much significantly affected by other factors, and difficult to quantify. Besides temperature effects, other factors also contribute to the changing of structural damping ratios. Xia et al. (2011) continued research for variation of vibration properties with respect to temperature distribution. The result also showed that the uncertainty level of damping was relatively high since the variation of temperature was not significant. Moser and Moaveni (2011) investigated effects of temperature on the identified natural frequencies and damping ratios of the Footbridge. While significant variability in natural frequencies was significantly correlated with temperature, no obvious pattern of variation is observed but large scattering was found in identified damping ratios.

As previously shown in Figure 4-28, however, the distribution of identified damping ratio of Jindo Bridge was similar in tendency to that of temperature. Therefore, the correlation between identified damping ratio and corresponding temperature was also considered in following section. Unfortunately, the surface temperature of Jindo Bridge was not measured at the bridge for 3 days. Instead of that, the atmosphere temperature measured at automatic weather station (AWS) at 10 km from the Jindo Bridge was used for

correlation analysis. The distance and position between the bridge and AWS are shown in Figure 5-2.

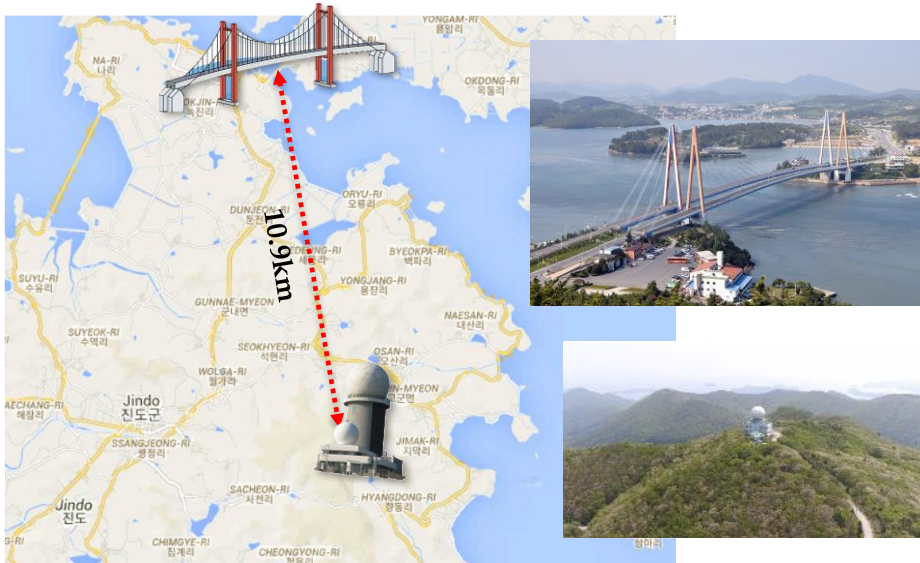


Figure 5-2 The location of Jindo Bridge and automatic weather station (AWS)

5.1.4. Aerodynamic damping ratio

The aerodynamic damping of the first vertical mode due to wind effect can be estimated with experimentally obtained flutter derivatives for the bridge sections based on the single-mode flutter analysis theory which assumed in Eqs 5-2 and 5-3. that the first vertical mode is induced with a purely heaving motion and not coupled with any other mode (Simiu and Scanlan, 1996) as

$$\xi_{ae} = \frac{\rho B^2}{4I} \left[H_1(K) \int_{deck} h(x)h(x)dx \right] \quad (5-2)$$

where I and $h(x)$ are the generalized mass of the bridge deck per unit length and the first vertical mode shape of the bridge deck shown in Figure 5-3(b), respectively. ρ is the air density ($=1.25\text{kg/m}^3$), B is the width of the bridge deck ($=12.690\text{ m}$), and H_1 is the flutter derivative which represent the self-excited lift force due to unit velocity of the deck motion in the vertical direction as shown in Figure 5-3(a). $K(\omega B/U)$ is a reduced frequency in which U is the mean wind velocity, ω the motional frequency for the first vertical mode under the wind action which can be estimated as

$$\omega = \omega_1 / \left(1 + \frac{\rho B^2}{2I} \left[H_4(K) \int_{deck} h(x)h(x)dx \right] \right) \quad (5-3)$$

in which ω_1 is the natural frequency of the first vertical mode, and H_4 the flutter derivatives relating the lift force due to unit displacement of the deck motion in the vertical direction.

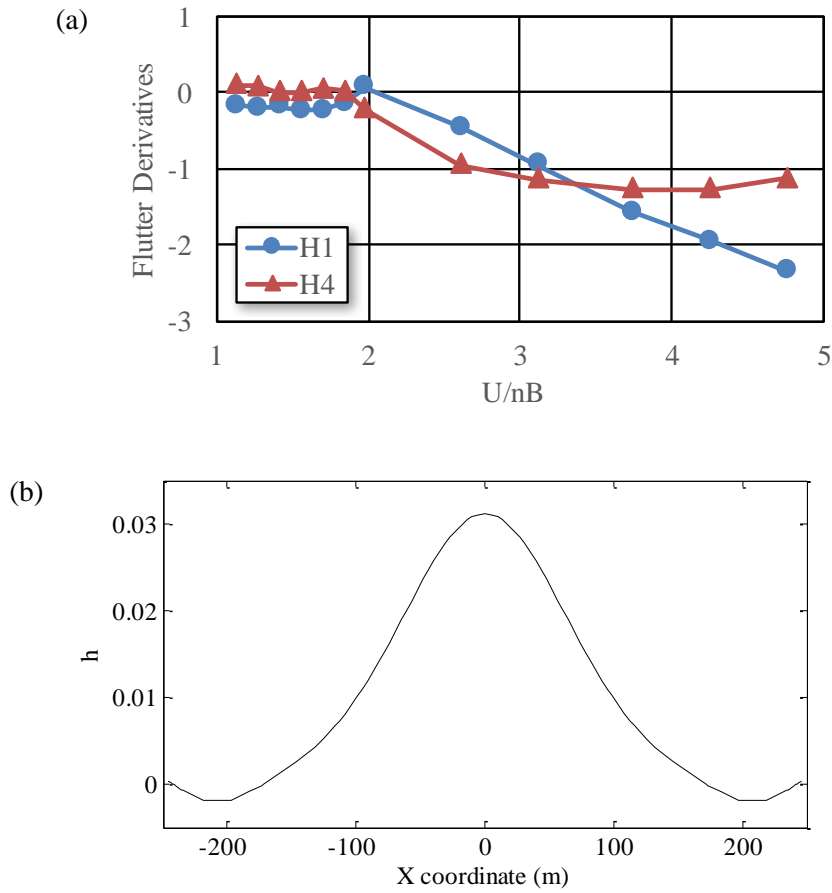


Figure 5-3 (a) Flutter derivatives and (b) Calculated mode shape along the bridge deck for the first vertical mode

Figure 5-4 showed the estimated aerodynamic damping ratio of the first vertical mode. Since the flutter derivatives measured in lock-in range (10~12 m/s) contain the shedding force, it is hard to calculate the pure aerodynamic damping ratio accurately. Actually, the flutter derivatives from a wind tunnel test are generally extracted with a considering only the self-excited forces, so that the aerodynamic damping calculated from flutter derivatives is not correct

value within the lock-in range. Furthermore, the aerodynamic damping ratios in lower velocity range (0~6.4m/s) were just linear fitted value as shown in Figure 5-4, not the measured value. Consequently, the aerodynamic damping ratios based on FDs were not considered in this research while the mean wind velocity during 3-days varied from 0~12 m/s.

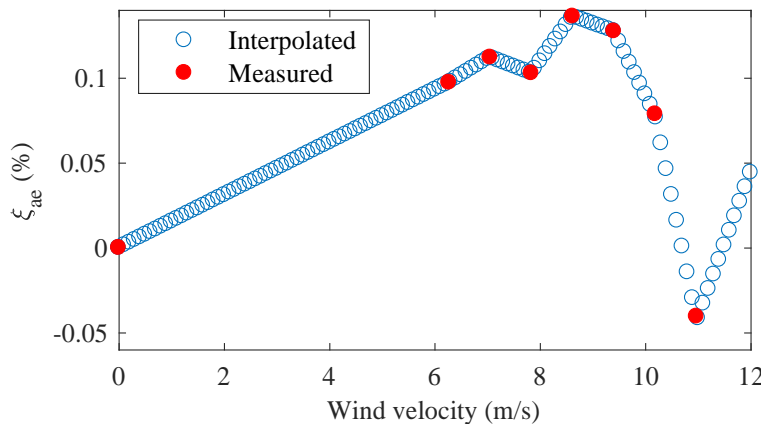


Figure 5-4 Estimated aerodynamic damping

5.2. Correlation analysis between estimated damping ratio and environmental factors

For the damping ratio, correlation analysis was performed for RMS amplitude, the number of vehicle and temperature. Since each unit is different, the normalized (average of 0 and standard deviation of 1) distribution of four parameters over 3 days was shown in Figure 5-5. It is clear that the trends of the four variables were much similar.

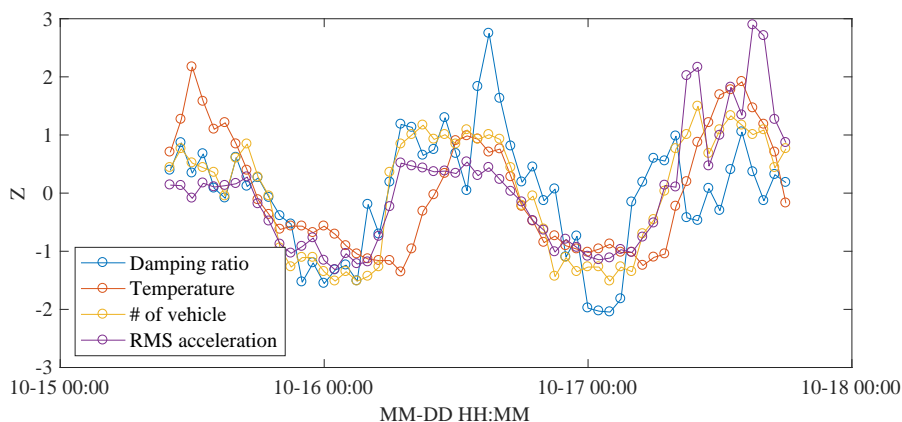


Figure 5-5 Normalized distribution of damping ratio and representative environmental factors according to time evolution (3-days)

Table 5-1 Correlation coefficient between identified damping ratios and environmental factor

	Damping ratio	RMS Acceleration	Number of vehicle	Temperature
Damping ratio	1.000	0.475	0.735	0.438
RMS acceleration		1.000	0.850	0.682
Number of vehicle			1.000	0.708
Temperature				1.000

The correlation analysis results for the damping ratio were shown in the Table 5-1. As can be seen from the Table 5-1, it can be confirmed that the variable with the highest correlation was the number of the vehicle while the tendency toward temperature was the lowest as expected. Interestingly, unlike vehicle numbers, the RMS amplitude is not high. This is presumably due to

the amplified response to the lock-in range.

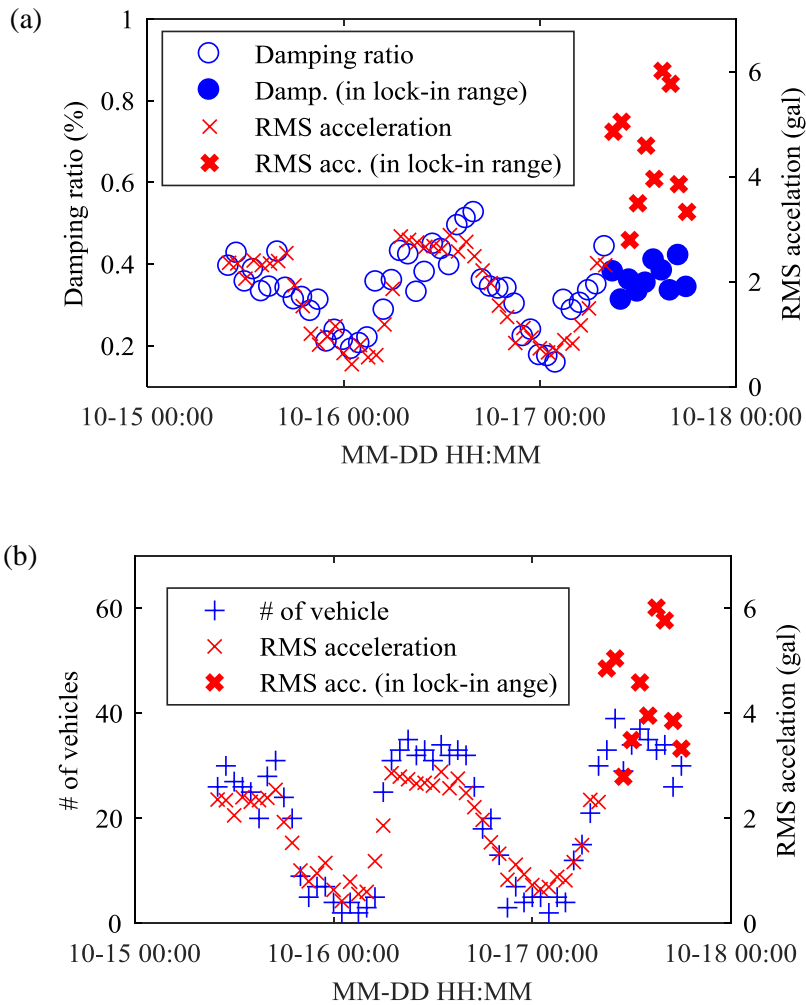


Figure 5-6 The distribution of RMS acceleration with (a) corresponding the number of vehicle and (b) identified damping ratios

In the lock-in range, the bridge was subjected to a vortex-shedding force, which amplified the vibration amplitude of the bridge deck. Figure 5-6(a) shows that the number of vehicle is similar for 3 days, but the RMS amplitude

rapidly increased on October 17 when the corresponding mean wind speed was within the lock-in wind velocity. On the other hand, these VIVs were supposed to not contribute to damping behavior, such as traffic-induced vibration. As shown be seen in Figure 5-6(b), regardless of larger amplitude due to VIVs, identified damping ratios did not increase as much.

5.3. Correlation analysis between estimated damping ratio and environmental factors without lock-in range data set

Figure 5-7 illustrates normalized distribution of damping ratio and representative environmental factors according to time evolution (3-days) after discarding the data set of lock-in range. Table 5-2 also summarizes the correlation coefficients between identified damping ratios and environmental factor without lock-in range data set. Also in this case, the factor that has the highest correlation with the damping ratio was the number of vehicles. It should be noticed that the correlation coefficient between damping ratio and RMS amplitude increased rapidly from 0.475 to 0.761. As a result, the coefficient between RMS acceleration and the number of vehicle was also enhanced from 0.850 to 0.968 which is almost 1.0.

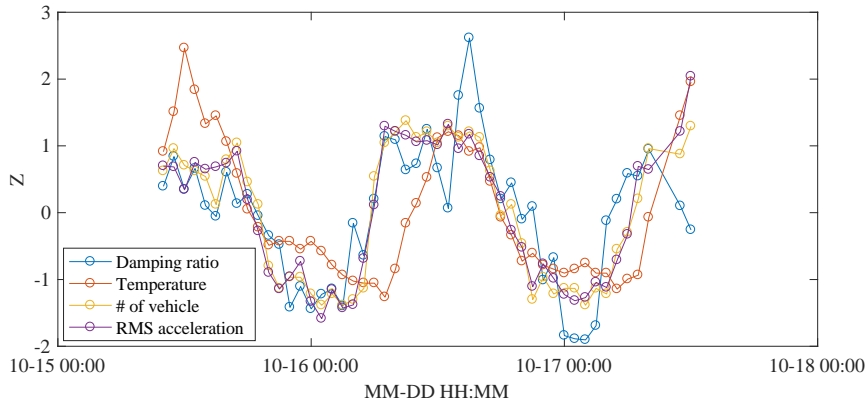


Figure 5-7 Normalized distribution of damping ratio and representative environmental factors according to time evolution (3-days) after discarding the lock-in data set

Based on these result, it can be supposed that the main source of the damping ratio in cable-stayed bridge was vibration induced by the vehicle loading. Furthermore, VIV can occur during service condition, which amplify the vibration amplitude of bridge deck, but did not seem not to contribute to the damping behavior, unlike traffic-induced vibration.

Table 5-2 Correlation coefficient between identified damping ratios and environmental factor without lock-in range data set

	Damping ratio	RMS Acceleration	Number of vehicle	Temperature
Damping ratio	1.000	0.761	0.805	0.447
RMS acceleration		1.000	0.968	0.674
Number of vehicle			1.000	0.663
Temperature				1.000

5.4. Amplitude-dependency

A previous research showed that the most dominant parameter on damping ratio changes was RMS acceleration by vehicle loadings. Consequently, this section described the amplitude-dependency of identified damping ratio. The data sets within the lock-in range were not eliminated in regression analysis, but considered separately.

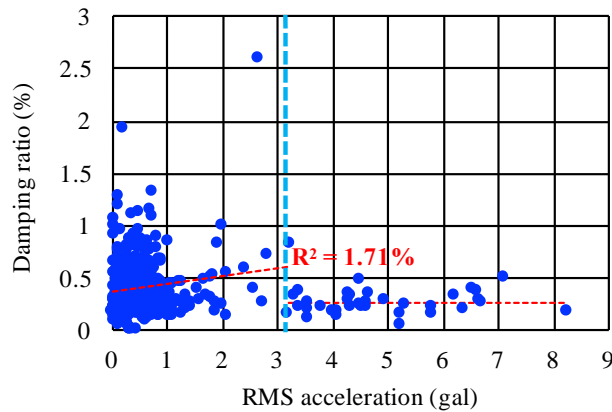


Figure 5-8 Amplitude-dependency of estimated damping ratio (basic)

Figure 5-8 illustrates the tendency of estimated damping ratio according to the RMS value of vertical acceleration in a basic estimation. A dashed red line in left-side is the linear regression line between RMS acceleration and the corresponding estimated damping ratios. Especially, the dots on the right side of the vertical dashed cyan line corresponded to the data within lock-in range. As can be seen, due to the higher scattering a clear amplitude-dependency was

not observed in estimated damping ratios while R^2 was just 1.71%.

Regardless of decreased scattering after parameter selection, the amplitude-dependency of estimated damping ratio is shown to be still poor in Figure 5-9. R^2 of 7.65% was slightly larger than the value of basic analysis.

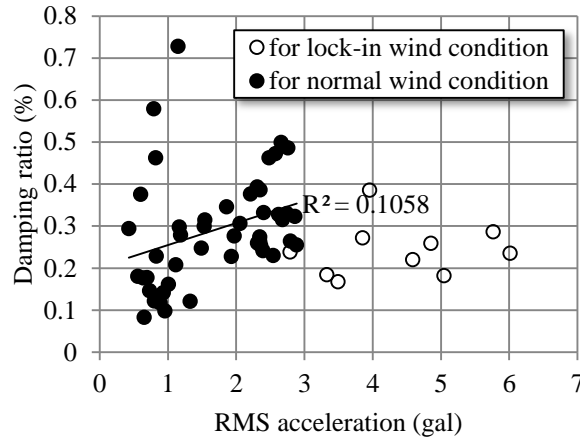


Figure 5-9 Amplitude-dependency of estimated damping ratio (proper parameter selection)

Figure 5-10 shows a clear relationship between RMS acceleration and estimated damping ratios after a signal stationarization. By applying a signal stationarization process, the unexpected scattering of the damping ratios in the range was reduced, resulting in a dramatic increase in R^2 value of linear regression from 7-8% to 67.82%. This indicates that the large uncertainties in estimated damping ratio can mask the amplitude-dependency, and it should be confirmed more clearly by reducing the large error bound by signal stationarization process.

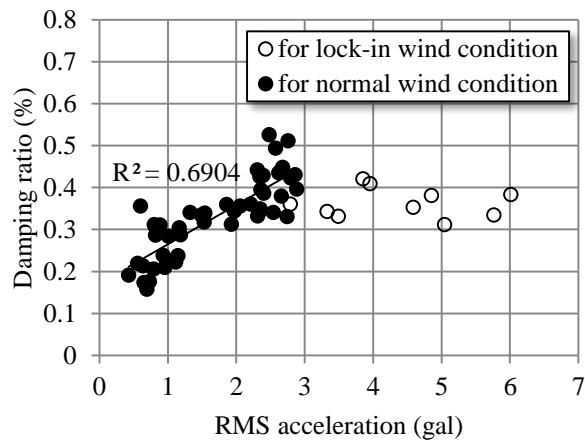


Figure 5-10 Amplitude-dependency of estimated damping ratio (signal stationarization)

In addition, as previously noted in Section 5.3, the VIV response within the lock-in range only increased in amplitude, not in the estimated damping ratio. It should be investigated with additional studied to determine whether this is a phenomenon in which all frictions in the bridge were fully activated so that a damping ratio no further increased or not. However, it is reasonable to conclude that the VIV amplitude does not contribute to the increase of the damping ratio, considering the previous results of correlation analysis and the limited level of VIV amplitude.

5.5. Conclusion

The study of parameter dependency of estimated damping ratio confirmed that the main source of damping ratio of cable-supported bridge was traffic-induced vibration. It also showed a high positive correlation with the number of vehicle and corresponding vibration amplitude of TIV. In the lock-in range, the RMS amplitude also increased, but there is no corresponding increase in the damping ratio. Although the tendency toward temperature was relatively low, it is considered that the effect on temperature should be studied in-depth in order to determine the seasonal variation of the damping ratio when the vehicle conditions are similar through long-term data. The analysis of the amplitude-dependency of the damping ratio clearly showed that the uncertainties in estimated damping ratios were significantly removed by automated parameter selection and stationarization. In the basic identification, the large error bounds masked the amplitude-dependency as in the previous studies, but this tendency was clearly appeared by applying the proposed method.

Chapter 6

Conclusions and further study

6.1. Conclusions and contributions

This research includes several contributions to the OMA and structural health monitoring system. Furthermore, it also gives the larger insight to the civil engineers and bridge owners for a design level of damping ratio and the utilization of operational monitored data.

The proposed parameter selection process allows to automated damping estimation using operational monitoring data. The current monitoring system in Korea can measure the responses of bridges of which quality was verified well. However, the application was only limited to alert the triggering based on the maximum limitation of wind velocity or acceleration, as well as rarely used to offer solutions for critical issues within the bridge. This is because the reliability of St-Id and condition assessment based on monitoring data was relatively poor, so that the additional AVT or controlled experiment was performed regardless of accumulated monitoring data. The proposed parameter selection leads to obtain a reliable damping estimation in real time without the controlled experiment or engineering judgements, and the availability of current SHM system would be rapidly increased.

This research also demonstrates the negative effect of traffic loading on the accuracy of classic OMA. Based on the field monitoring data accompanying with the truck loading test, the nonstationarity of TIV and its

distortion in PSD was successfully illustrated through the time and frequency domain. The result of estimated damping ratio indicates the limitation of application of classic OMA to TIV directly. To reduce this TIV properties found in real-world data, this dissertation proposed the signal stationarization process. The applicability of signal stationarization process to the real-world data was successfully demonstrated through the comparisons in time histories and PSDs, respectively. It leads to more accurate damping estimation compared to the direct application of classic OMA to measured TIV. The bias and variance error in estimates were clearly decreased, as well as the amplitude-dependency of damping ratio appeared more clearly compared to the result without a signal stationarization process. With the application of this simple process, the well-verified classic OMA such as NExT-ERA or SSI-COV can be implemented to the response of cable-stayed bridges.

The identified damping ratios under the MTMD conform to both the target design damping values by the MTMD as well as the value estimated from the free decaying response of the exited deck by one TMD. The contribution of the MTMD to overall structural damping depends on the wind velocity. For a low wind velocity, the MTMD is not well activated and the increase in modal damping for the first vertical mode remains limited. However, as the wind velocity approaches the onset wind velocity of the VIV,

the identified damping ratios reach the target design level for the MTMD. For a low wind velocity, the MTMD is not well activated and the increase in modal damping for the first vertical mode remains limited. However, as the wind velocity approaches the onset wind velocity of the VIV, about 10~12 m/s, the identified damping ratios reach the target design level for the MTMD. Based on a plot between the identified damping ratios and the corresponding deck responses, the current bridge with a MTMD satisfies the vibrational serviceability criteria.

The study of parameter dependency of estimated damping ratio confirmed that the main source of damping ratio of cable-supported bridge was traffic-induced vibration with a high positive correlation. Even though VIV also contributed to amplify the vibration amplitude, the amplitude increase due to VIV has little effect on the damping ratio. this vibration was relatively but the damping was not increased by VIV. Regardless of the similar pattern of damping and temperature changes, the effect of temperature on damping ratio variation was not significant either.

6.2. Suggestion

This paper showed couple of efforts to approach these impending issues by introducing database for probabilistic assessment and data processing to

eliminate large scattering in identified damping ratios. Especially, the modal damping ratios can only be estimated when a bridge construction is being completed, but have been overlooked for years. The more accurate damping estimation based on automated OMA can enhance the applicability of St-Id, which has been only limited in a damage detection or model updating based on natural frequencies or mode shapes. Furthermore, it can also secure the accuracy in bridge maintenance as well as the design, prediction and assessment for hazardous vibration and the instant design feedback and solutions for critical issues in the structure. The author recommends to bridge owners to secure initial damping ratios for dominant modes and to confirm the validity of wind-resistance design in terms of design damping ratios.

As various factors affect, the impact of the environmental factor should be identified through long-term data. Especially, since the influence of temperature is relatively insignificant, it is essential to analyze the case where the temperature is different from the dominant factor such as amplitude, vehicle number, and wind speed were similar. This approach inevitably requires estimation of the damping ratio for long-term data. At present, for the operational monitoring system of Korean bridges, only the 10-minute statistical value of the measurement data is recorded in server, and the raw data is removed every week. As can be seen, the proposed damping ratio

estimation algorithm can automatically estimate the damping ratio with high accuracy without any heuristic user judgment. Therefore, if the modal information database is constructed by automated estimating the damping ratio and the natural frequency along with the general statistical processing, the influence of environmental factors on the damping behavior of cable-supported bridges can be evaluated more clearly.

The Korean guideline suggests the design damping as a 0.4% for cable-supported bridge. However, this dissertation clearly showed that the actual damping ratio was a level of 0.3%, and the serviceability problem was very sensitive to the lack of damping ratio. Especially, as can be seen in the case of Jindo Bridge, the damping ratio of the bridge can be reduced from 0.4% to at least 0.1-0.2% when the amplitude is low. Therefore, if necessary, the level of design damping ratio can be lowered to accommodate a potential possibility of low damping ratios of flexible structures, which adopt higher-strength materials and simpler connections. As previously mentioned, the bridge owner can secure the accumulated damping estimates from the monitoring data in real time. If the damping ratio can be estimated directly from the real-time measured acceleration, and accumulated with other environmental aspects, it can be helpful to decide the design damping ratio.

References

1. Bartos MJ. Ontario Writes New Bridge Code. Civil Engineering—ASCE. 1979;49(3):56-61.
2. Bendat JS, Piersol A. Random Data: Analysis and Measurement Procedures, John Wiley & Sons. Inc; 2000.
3. Benedettini F, Gentile C. Operational modal testing and FE model tuning of a cable-stayed bridge. Engineering Structures. 2011;33(6):2063-73.
4. Brewick PT, Smyth AW. Exploration of the impacts of driving frequencies on damping estimates. Journal of Engineering Mechanics. 2014;141(3):04014130.
5. Brincker R, Krenk S, Kirkegaard PH, Rytter A. Identification of dynamical properties from correlation function estimates. Danish Society for Structural Science and Engineering; 1992.
6. Brincker R, Ventura C, Andersen P, editors. Damping estimation by frequency domain decomposition. 19th International Modal Analysis Conference; 2001.
7. Brincker R, Zhang L, Andersen P, editors. Modal identification from ambient responses using frequency domain decomposition. Proc of the 18th International Modal Analysis Conference (IMAC), San Antonio, Texas; 2000.
8. Brownjohn J, Magalhaes F, Caetano E, Cunha A. Ambient vibration re-testing and operational modal analysis of the Humber Bridge. Engineering Structures. 2010;32(8):2003-18.
9. Brownjohn J, Magalhaes F, Caetano E, Cunha A. Ambient vibration re-testing and operational modal analysis of the Humber Bridge. Eng Struct. 2010;32:2003.
10. Brownjohn JMW, Moyo P, Omenzetter P, Lu Y. Assessment of highway bridge upgrading by dynamic testing and finite-element model updating. Journal of Bridge Engineering. 2003;8(3):162-72.
11. Caicedo J. Practical guidelines for the natural excitation technique (NExT) and the eigensystem realization algorithm (ERA) for modal identification using ambient vibration. Exp Tech. 2010;35:52.

12. Caicedo JM, Dyke SJ, Johnson EA. Natural excitation technique and eigensystem realization algorithm for phase I of the IASC-ASCE benchmark problem: Simulated data. *Journal of Engineering Mechanics*. 2004;130(1):49-60.
13. Chen G-W, Beskhyroun S, Omenzetter P. Experimental investigation into amplitude-dependent modal properties of an eleven-span motorway bridge. *Engineering Structures*. 2016;107:80-100.
14. Chiang D, Lin C. Identification of modal parameters from ambient vibration data using eigensystem realization algorithm with correlation technique. *J Mech Sci Technol*. 2010;24:2377.
15. Chiang D-Y, Lin C-S. Identification of modal parameters from nonstationary ambient vibration data using correlation technique. *AIAA journal*. 2008;46(11):2752-9.
16. Davenport RG, editor FFT processing of direct sequence spreading codes using modern DSP microprocessors. Aerospace and Electronics Conference, 1991 NAECON 1991, Proceedings of the IEEE 1991 National; 1991: IEEE.
17. De Roeck G. Stochastic system identification for operational modal analysis: a review. 2001.
18. Farrar C, James GI. System identification from ambient vibration measurements on a bridge. *J Sound Vib*. 1997;205:1.
19. Farrar C, Jauregui D. Comparative study of damage identification algorithms applied to a bridge: II. Numerical study. *Smart Mater Struct*. 1998;7:720.
20. Feng MQ, Fukuda Y, Chen Y, Soyoz S, Lee S. Long-term structural performance monitoring of bridges. Phase II: Development of Baseline Model and Methodology—Report to the California Department of Transportation. 2006.
21. Fu Z-F, He J. *Modal analysis*: Butterworth-Heinemann; 2001.
22. Fukuwa N, Nishizaka R, Yagi S, Tanaka K, Tamura Y. Field measurement of damping and natural frequency of an actual steel-framed building over a wide range of amplitudes. *Journal of wind engineering and industrial aerodynamics*. 1996;59(2-3):325-47.
23. Guo W, Xu Y. Fully computerized approach to study cable-stayed bridge–vehicle interaction. *Journal of Sound and Vibration*.

- 2001;248(4):745-61.
24. Guo Y. Nonstationary system identification techniques: UNIVERSITY OF NOTRE DAME; 2015.
 25. Guo Y, Kareem A, Ni Y, Liao W. Performance evaluation of Canton Tower under winds based on full-scale data. *Journal of Wind Engineering and Industrial Aerodynamics*. 2012;104:116-28.
 26. HDEC. Report on Performance Assessment for MTMD on Second Jindo Bridge. Hyundai Engineering and Construction; 2012.
 27. HDEC. Report on the Mitigation for Vortex-Induced Vibration of Second Jindo Bridge. Hyundai Engineering and Construction; 2012.
 28. He X, Moaveni B, Conte JP, Elgamal A, Masri SF. System identification of Alfred Zampa Memorial Bridge using dynamic field test data. *Journal of Structural Engineering*. 2009;135(1):54-66.
 29. Hua X, Ni Y, Ko J, Wong K. Modeling of temperature–frequency correlation using combined principal component analysis and support vector regression technique. *Journal of Computing in Civil Engineering*. 2007;21(2):122-35.
 30. Ill GHJ, Carrie TG, Lauffer JP. The natural excitation technique (NExT) for modal parameter extraction from operating wind turbines. 1993.
 31. James GH, Carne TG, Lauffer JP, Nord AR, editors. Modal testing using natural excitation. PROCEEDINGS OF THE INTERNATIONAL MODAL ANALYSIS CONFERENCE; 1992: SEM SOCIETY FOR EXPERIMENTAL MECHANICS INC.
 32. Jeary A. Damping in tall buildings—a mechanism and a predictor. *Earthquake engineering & structural dynamics*. 1986;14(5):733-50.
 33. Jeary A. Establishing non-linear damping characteristics of structures from non-stationary response time-histories. *Structural Engineer*. 1992;70:61-6.
 34. Ju M, Park C, Kim G. Structural Health Monitoring (SHM) for a cable stayed bridge under typhoon. *KSCE Journal of Civil Engineering*. 2015;19(4):1058-68.
 35. Juang J-N, Pappa RS. An eigensystem realization algorithm for modal parameter identification and model reduction. *Journal of guidance, control, and dynamics*. 1985;8(5):620-7.

36. Kareem A, Gurley K. Damping in structures: its evaluation and treatment of uncertainty. *Journal of Wind Engineering and Industrial Aerodynamics*. 1996;59(2):131-57.
37. Kim C-W, Kawatani M. Pseudo-static approach for damage identification of bridges based on coupling vibration with a moving vehicle. *Structure and infrastructure engineering*. 2008;4(5):371-9.
38. Kim CW, Kawatani M, Kim KB. Three-dimensional dynamic analysis for bridge–vehicle interaction with roadway roughness. *Computers & structures*. 2005;83(19):1627-45.
39. Kim S, Kim H-K. Damping Identification of Bridges under Nonstationary Ambient Vibration (under review). *Engineering*. 2017.
40. Kim S, Kim H-K, Hwang YC. Enhanced Damping Estimation for Cable-Stayed Bridges from Operational Monitoring Data (submitted). *Structural Engineering International*. 2018.
41. Kim S, Park J, Kim H-K. Damping Identification and Serviceability Assessment of a Cable-Stayed Bridge Based on Operational Monitoring Data. *Journal of Bridge Engineering*. 2016;04016123.
42. Kim S-J, Kim H-K, Calmer R, Park J, Kim GS, Lee DK. Operational field monitoring of interactive vortex-induced vibrations between two parallel cable-stayed bridges. *Journal of wind engineering and industrial aerodynamics*. 2013;123:143-54.
43. KSCE. Design Guidelines for Steel Cable-Supported Bridges. Korea: Korean Society of Civil Engineers; 2006.
44. Li Q, Yang K, Zhang N, Wong C, Jeary A. Field measurements of amplitude-dependent damping in a 79-storey tall building and its effects on the structural dynamic responses. *The Structural Design of Tall and Special Buildings*. 2002;11(2):129-53.
45. Lin C, Yang Y. Use of a passing vehicle to scan the fundamental bridge frequencies: An experimental verification. *Engineering Structures*. 2005;27(13):1865-78.
46. Lin C-S, Chiang D-Y. Modal identification from nonstationary ambient response data using extended random decrement algorithm. *Computers & Structures*. 2013;119:104-14.
47. Magalhães F, Caetano E, Cunha Á. Challenges in the application of stochastic modal identification methods to a cable-stayed bridge. *Journal*

- of Bridge Engineering. 2007;12(6):746-54.
48. Magalhães F, Caetano E, Cunha Á, Flamand O, Grillaud G. Ambient and free vibration tests of the Millau Viaduct: Evaluation of alternative processing strategies. *Engineering Structures*. 2012;45:372-84.
 49. Magalhães F, Caetano E, Cunha Á, Flamand O, Grillaud G. Ambient and free vibration tests of the Millau Viaduct: Evaluation of alternative processing strategies. *Eng Struct*. 2012;45:372.
 50. Magalhães F, Cunha A. Explaining operational modal analysis with data from an arch bridge. *Mechanical systems and signal processing*. 2011;25(5):1431-50.
 51. Magalhães F, Cunha A, Caetano E. Vibration based structural health monitoring of an arch bridge: from automated OMA to damage detection. *Mechanical Systems and Signal Processing*. 2012;28:212-28.
 52. Magalhães F, Cunha Á, Caetano E, Brincker R. Damping estimation using free decays and ambient vibration tests. *Mechanical Systems and Signal Processing*. 2010;24(5):1274-90.
 53. Majka M, Hartnett M. Effects of speed, load and damping on the dynamic response of railway bridges and vehicles. *Computers & Structures*. 2008;86(6):556-72.
 54. Martínez-Rodrigo MD, Filiatrault A. A case study on the application of passive control and seismic isolation techniques to cable-stayed bridges: A comparative investigation through non-linear dynamic analyses. *Engineering Structures*. 2015;99:232-52.
 55. Moaveni B, Barbosa AR, Conte JP, Hemez FM. Uncertainty analysis of system identification results obtained for a seven-story building slice tested on the UCSD-NEES shake table. *Structural Control and Health Monitoring*. 2014;21(4):466-83.
 56. Moon F, Aktan A. Impacts of epistemic (bias) uncertainty on structural identification of constructed (civil) systems. *Shock and Vibration Digest*. 2006;38(5):399-422.
 57. Moser P, Moaveni B. Environmental effects on the identified natural frequencies of the Dowling Hall Footbridge. *Mechanical Systems and Signal Processing*. 2011;25(7):2336-57.
 58. Newland DE. An introduction to random vibrations, spectral & wavelet analysis: Courier Corporation; 2012.

59. Pappa RS, Schenk A, Noll C. Eigensystem realization algorithm modal identification experiences with mini-mast. 1992.
60. Park W, Kim H-K, Jongchil P. Finite element model updating for a cable-stayed bridge using manual tuning and sensitivity-based optimization. *Structural Engineering International*. 2012;22(1):14-9.
61. Park W, Park J, Kim H-K. Candidate model construction of a cable-stayed bridge using parameterised sensitivity-based finite element model updating. *Structure and Infrastructure Engineering*. 2015;11(9):1163-77.
62. Rainieri C, Fabbrocino G. Operational modal analysis of civil engineering structures. Springer, New York. 2014;142:143.
63. Reynders E, Houbrechts J, Roeck GD. Fully automated (operational) modal analysis. *Mech Syst Sig Process*. 2012;29:228.
64. Rodrigues J, Brincker R. Application of the random decrement technique in operational modal analysis. 2005.
65. Seo J-W, Kim H-K, Park J, Kim K-T, Kim G-N. Interference effect on vortex-induced vibration in a parallel twin cable-stayed bridge. *Journal of wind engineering and industrial aerodynamics*. 2013;116:7-20.
66. Seo JW. Mitigation of vortex-induced vibration of twin cable-stayed bridge girder using multiple tuned mass dampers. *Mag Korean Soc Steel Constr*. 2015;27:57.
67. Seo JW, Kim HK, Park J, Kim KT, Kim GN. Interference effect on vortex-induced vibration in a parallel twin cable-stayed bridge. *J Wind Eng Ind Aerodyn*. 2013;116:7.
68. Sim S-H, Carbonell-Márquez JF, Spencer B, Jo H. Decentralized random decrement technique for efficient data aggregation and system identification in wireless smart sensor networks. *Probabilistic Engineering Mechanics*. 2011;26(1):81-91.
69. Sim S-H, Spencer B, Zhang M, Xie H. Automated decentralized modal analysis using smart sensors. *Structural Control and Health Monitoring*. 2010;17(8):872-94.
70. Sim SH. Decentralized identification and multimetric monitoring of civil infrastructure using smart sensors: University of Illinois at Urbana-Champaign; 2011.
71. Simiu E, Scanlan RH. Wind effects on structures: Wiley; 1996.

72. Siringoringo DM, Fujino Y. System identification applied to long-span cable-supported bridges using seismic records. *Earthquake Engineering & Structural Dynamics*. 2008;37(3):361-86.
73. Siringoringo DM, Fujino Y. System identification of suspension bridge from ambient vibration response. *Engineering Structures*. 2008;30(2):462-77.
74. Sohn H, Dzwonczyk M, Straser EG, Kiremidjian AS, Law KH, Meng T. An experimental study of temperature effect on modal parameters of the Alamosa Canyon Bridge. *Earthquake engineering & structural dynamics*. 1999;28(8):879-97.
75. Spencer Jr B, Cho S, Sim S-H. Wireless monitoring of civil infrastructure comes of age. *Structure*. 2011;13.
76. Sun H, Feng DM, Liu Y, Feng MQ. Statistical Regularization for Identification of Structural Parameters and External Loadings Using State Space Models. *Computer-Aided Civil and Infrastructure Engineering*. 2015;30(11):843-58.
77. Tamura Y, Suda K, Sasaki A, editors. Damping in buildings for wind resistant design. *Proceedings of the International Symposium on Wind and Structures for the 21st Century*; 2000.
78. The Ontario Code. Documentation Bridge Code. 1991.
79. Van Overschee P, De Moor B. Subspace identification for linear systems: Theory—Implementation—Applications: Springer Science & Business Media; 2012.
80. Wen Q, Hua X, Chen Z, Guo J, Niu H. Modal parameter identification of a long-span footbridge by forced vibration experiments. *Advances in Structural Engineering*. 2017;1369433217698322.
81. Xia Y, Hao H, Zanardo G, Deeks A. Long term vibration monitoring of an RC slab: temperature and humidity effect. *Engineering Structures*. 2006;28(3):441-52.
82. Xia Y, Xu Y-L, Wei Z-L, Zhu H-P, Zhou X-Q. Variation of structural vibration characteristics versus non-uniform temperature distribution. *Engineering structures*. 2011;33(1):146-53.
83. Xing C, Wang H, Li A, Xu Y. Study on wind-induced vibration control of a long-span cable-stayed bridge using TMD-type counterweight. *Journal of Bridge Engineering*. 2013;19(1):141-8.

84. Yun GJ, editor Modal identification and damage detection for structural health monitoring under ambient vibration environment. Structures Congress 2009: Don't Mess with Structural Engineers: Expanding Our Role; 2009.
85. Zhang P. Experimental modal analysis of star-spar buoy using eigensystem realization algorithm and stochastic subspace identification methods: University of Rhode Island; 2012.

국 문 초 록

응답기반모드해석(Operational Modal Analysis, OMA) 기반 추정 감쇠비의 불확실성을 줄이기 위해 자동화된 변수선정 및 신호 정상화 과정에 기반한 개선된 Natural Excitation Technique—Eigensystem Realization (NExT-ERA) 알고리즘을 제안하였으며, 다중질량동조감쇠기(Multiple Tuned Mass Damper, MTMD) 설치 전후의 사장교 계측 데이터에 적용하여 그 정당성을 검증하였다. 상관분석을 통해 환경적 요인의 영향을 분석하고 감쇠비 변화에 가장 주요한 원인이 되는 환경적 요인을 선정, 회귀분석을 수행하여 제안한 방법 적용 전후에 따라 감쇠비의 불확실성이 얼마나 줄어드는지를 확인하였다.

경험적 변수선택에 준하는 감쇠비 추정의 정확도 및 정밀도의 확보를 목표로 자동화된 변수 선정 절차를 제안하였다. 먼저 적절한 변수 구간을 선정하기 위해 수치해석과 계측 데이터를 활용한 변수 연구를 수행하였다. 평균과 변동계수를 통해 정확도 및 정밀도를 평가한 결과, 샘플링 주파수 100Hz 에서 데이터 길이 60 분에 Number of FFT 215 일 때 가장 좋은 결과를 보였다. 행렬 행렬의 크기는 계산된 임펄스응답함수가 최대값의 50% 만큼 되었을 때를 기준으로 결

정하였다. 시스템 차수에 따른 추정 감쇠비의 분산을 해결하기 위해, 시스템 차수를 1 부터 50 까지 바꿔가며 추정한 감쇠비의 중앙값을 취하였다. 상기의 자동화된 변수 선정 절차는 경험적 변수선택보다 더욱 정확한 결과를 보였다.

현장실험을 통해 차량으로 인해 응답이 집중화되는 것과 그것이 OMA 기반 감쇠비 추정에 미치는 영향을 분석하였다. 교량의 차선이 적고 통행량이 많지 않을 경우, 차량이 센서에 근접함에 따라 상시계측 가속도가 커지고 차량이 센서를 지나감에 따라 응답이 줄어들게 된다. OMA 는 하중을 정상상태 백색잡음으로 가정하기 때문에, 이러한 차량에 의한 하중 및 응답의 비정상성은 OMA 불확실성의 한 원인이 된다. 또한 이러한 차량 하중은 계측 가속도의 파워스펙트럼함수(Power Spectral Density function, PSD)의 주파수 성분을 왜곡한다. 정상상태 하중 및 차량하중에 의한 계측가속도 PSD 를 비교했을 때, 차량이 지나갈 때 2-5Hz 의 고주파 성분이 증폭되는 것을 확인하였다. ERA 는 에너지 기반의 기법으로, 지배적인 모드를 보다 쉽게 식별하기 때문에 이러한 PSD 의 왜곡 역시 추정 감쇠비에 오류를 야기할 수 있다.

계측 데이터의 시계열에서 나타나는 비정상성을 제거하기 위해,

진폭변조함수를 통한 신호 정상화 과정을 제안하였다. 비정상성 시계열은 포락함수와 정상 시계열의 곱으로 표현할 수 있다. 따라서 계측데이터의 이동 Root-Mean-Square(RMS)로부터 포락함수를 구해 계측 데이터를 포락함수로 나누면 계측 데이터 내 정상 시계열만을 성공적으로 추출할 수 있다. 제안한 신호 정상화 과정을 3 일간의 상시진동 데이터에 적용하여 감쇠비를 추정한 결과 추정치의 큰 편향들이 제거되었고, 변동계수 역시 줄어들었다. 이를 통해 신호 정상화 과정이 감쇠비의 불확실성을 제거하는데 유효함을 확인하였다.

대상교량에 MTMD 가 설치된 이후의 감쇠비를 동일한 방식으로 추정하였다. 다양한 바람 조건 하에서 계측된 4 일간의 데이터를 통해 감쇠비를 추정한 결과, 역시 자동화된 변수 선택 및 신호 정상화 과정이 OMA 기반 추정 감쇠비의 불확실성을 줄여주는 것을 확인하였다. 특별히 MTMD 에 의한 감쇠비 증가 효과는 풍속이 와류진동 위험풍속일 경우 가장 컸으며, 일반적인 풍속 조건에서는 비록 설계 수준의 성능을 보이지는 않았음에도 불구하고 충분한 제진 효과를 나타내었다.

마지막으로 환경적 요인이 감쇠비 변화에 미치는 영향을 평가하였다. 진폭, 차량 대수 및 온도를 대상 변수로 선정, 상관성 분석

을 통해 각 환경적 요인과 감쇠비 사이의 관련성을 분석하였다. 그 결과 차량에 의한 진동이 케이블 교량 진동 발현에 가장 큰 요인임을 확인하였다. 와류진동 Lock-in 구간에서도 진폭이 증가하였으나, 이는 감쇠비 증가에는 영향을 미치지 않는 것으로 나타났다. 온도와 의 상관성 역시 상대적으로 낮았다. 대표 변수인 차량에 의한 진폭 의존도(amplitude-dependency)를 회귀분석을 통해 분석한 결과, 신호 정상화 과정을 적용하기 전에는 거의 나타나지 않던 상관성이 신호 정상화 적용에 따라 명확하게 나타나는 것을 확인하였다.

주요어: Operational Modal Analysis, Damping ratio, NExT-ERA, Cable-supported bridge, Stationarization, Amplitude-dependency,

Student Number: 2012-30241